

HYBRIDARMERING FÖR OPTIMERING AV LIVSLÄNGD OCH LIVSCYKELKOSTNAD

Ingemar Löfgren

2021-06-17

FÖRORD

SBUF-projektet 13683, ”Hybridarmering för optimering av livslängd och livscykelkostnad” har erhållit ekonomiskt stöd från Trafikverket/BBT (projekt 2017-015), SBUF, Thomas Concrete Group, Chalmers tekniska högskola, Cementa, NCC och Skanska.

Vi vill med den här delrapporten rikta ett stort tack till Trafikverket/BBT och SBUF - Svenska Byggbranschens Utvecklingsfond, för deras stöd och finansiering som möjliggjort detta projekt. Utöver Trafikverket och SBUF vill vi i projektgruppen även tacka övriga finansiärer.

Projektet har genomförts som ett postdok projekt vid Chalmers tekniska högskola och aktiva forskare inom projektet:

- PhD Teresa E Chen, postdok
- PhD Carlos Gil Berrocal, postdok
- Professor Karin Lundgren
- Adjungerad professor Ingemar Löfgren (projektledare)

I referensgruppen har följande personer ingått:

- Christine Warg, Trafikverket
- Elisabeth Helsing, RISE
- Hans Hedlund, Skanska
- Jonas Magnusson, NCC
- Mikael Westerholm, Cementa,
- Magnus Bäckström, Sweco

INNEHÅLL

BAKGRUND OCH INLEDNING	5
EXPERIMENT OCH RESULTAT	5
KORROSIONSMÖNSTER RELATERAT TILL SPRICKOR I BETONGEN	6
MODELLERING AV BÄRFÖRMÅGA.....	9
FALLSTUDIE PÅ KANTBALKAR.....	9
SLUTSATSER.....	13
PUBLIKATIONER INOM PROJEKTET:	14
EXAMENSARBETEN GENOMFÖRDA INOM PROJEKTET:	14

BAKGRUND OCH INLEDNING

Armerad betong i broar och tunnlar utsätts för klorider från tölsalter, som orsakar korrosion av armeringen. Detta är ett mycket utbredd problem, som allvarligt påverkar beständigheten, särskilt i utsatta delar som t ex kantbalkar. Nuvarande normer har därför strikta krav i form av små tillåtna sprickvidder. Detta leder ofta till tätt armerade konstruktioner som orsakar svårigheter i produktionen, men trots detta är det svårt att uppfylla sprickbreddskraven och ofta krävs en kostsam injektering. Ett intressant alternativ är att vid både reparation och nybyggnation använda hybridarmerade lösningar, i vilka fibrer och traditionell armering kombineras för att uppnå sprickkontroll. Utöver förbättrad beständighet, erbjuder sådana lösningar förbättrad arbetsmiljö och ökad produktivitet genom en mer industrialiserad byggprocess.

Idag är Trafikverket restriktivt gentemot hybridarmerade konstruktioner i kloridhaltiga miljöer, på grund av farhågor om att stålfibrer skulle påverka korrosion av armeringsstänger på ett negativt sätt, genom minskad resistivitet och risk för galvanisk korrosion. I ett doktorandprojekt som genomförts i samarbete mellan Chalmers tekniska högskola och Thomas Concrete Group har dessa risker undersökts experimentellt. Resultaten visar att farhågorna är kraftigt överdrivna, istället kan hybridarmering förlänga livslängden, dels genom att armeringskorrosion fördröjs och minskas, och dels genom att effekten på bärförmågan av korrosionsskador begränsas. Dessa resultat och slutsatser stämmer väl med internationell forskning. Syftet med projektet har varit att ytterligare undanröja tvivel och underbygga slutsatserna, och ta de positiva resultaten vidare till praktisk användning.

De publikationer som har publicerats i projektet finns redovisat på Chalmers¹. Följande artiklar har publicerats (open source):

- Correlation between concrete cracks and corrosion characteristics of steel reinforcement in pre-cracked plain and fibre-reinforced concrete beams. *Materials and Structures*, vol. 53, Article number: 33 (2020)
<https://link.springer.com/article/10.1617/s11527-020-01466-z>
- Assessment of the mechanical behaviour of reinforcement bars with localised pitting corrosion by Digital Image Correlation. *Engineering Structures*, Vol. 219, 15 September 2020, 110936
<https://www.sciencedirect.com/science/article/pii/S0141029620313390?via%3Dihub>
- Comparison of the service life, life-cycle costs and assessment of hybrid and traditional reinforced concrete through a case study of bridge edge beams in Sweden. *Structure and Infrastructure Engineering*,
<https://www.tandfonline.com/doi/full/10.1080/15732479.2021.1919720>

EXPERIMENT OCH RESULTAT

Ett program med långtidsförsök inleddes 2013 för att studera hybridarmerade betongbalkars prestanda i kloridhaltig miljö [2]. Totalt ingick 54 balkar med dimensionen 100×180×1100 mm, vardera armerad med tre Ø10 stänger. Fyra betongsorter ingick: utan fibrer, samt tre olika sorters fiberbetong. Vidare delades provkropparna in i spruckna och ospruckna balkar. De

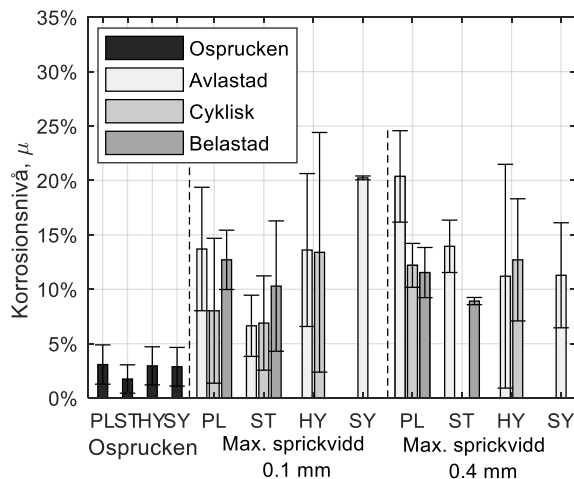
¹ <https://research.chalmers.se/project/8328>

² Berrocal CG. Corrosion of steel bars in fibre reinforced concrete: Corrosion mechanisms and structural performance, Doctoral Thesis, Chalmers University of Technology; 2017.

utsattes för omväxlande torra och våta perioder under sammanlagt tre år, där de våta perioderna inkluderade 16,5% NaCl-lösning för att främja korrosion. Ytterligare detaljer om betongrecept, fiberegenskaper och försöksuppställning finns i [1]. I det aktuella projektet studerades 22 balkar, i vilka vi undersökte korrosionsmönstret i förhållande till sprickor och där de mekaniska egenskaperna hos de korroderade armeringsstängerna karakteriserades. Först kartlades sprickbilderna som inkluderade både tvärgående böjsprickor och längsgående korrosionssprickor. Därefter extraherades armeringsstängerna från balkarna för kartering av korrosionsmönster och dragprovning.

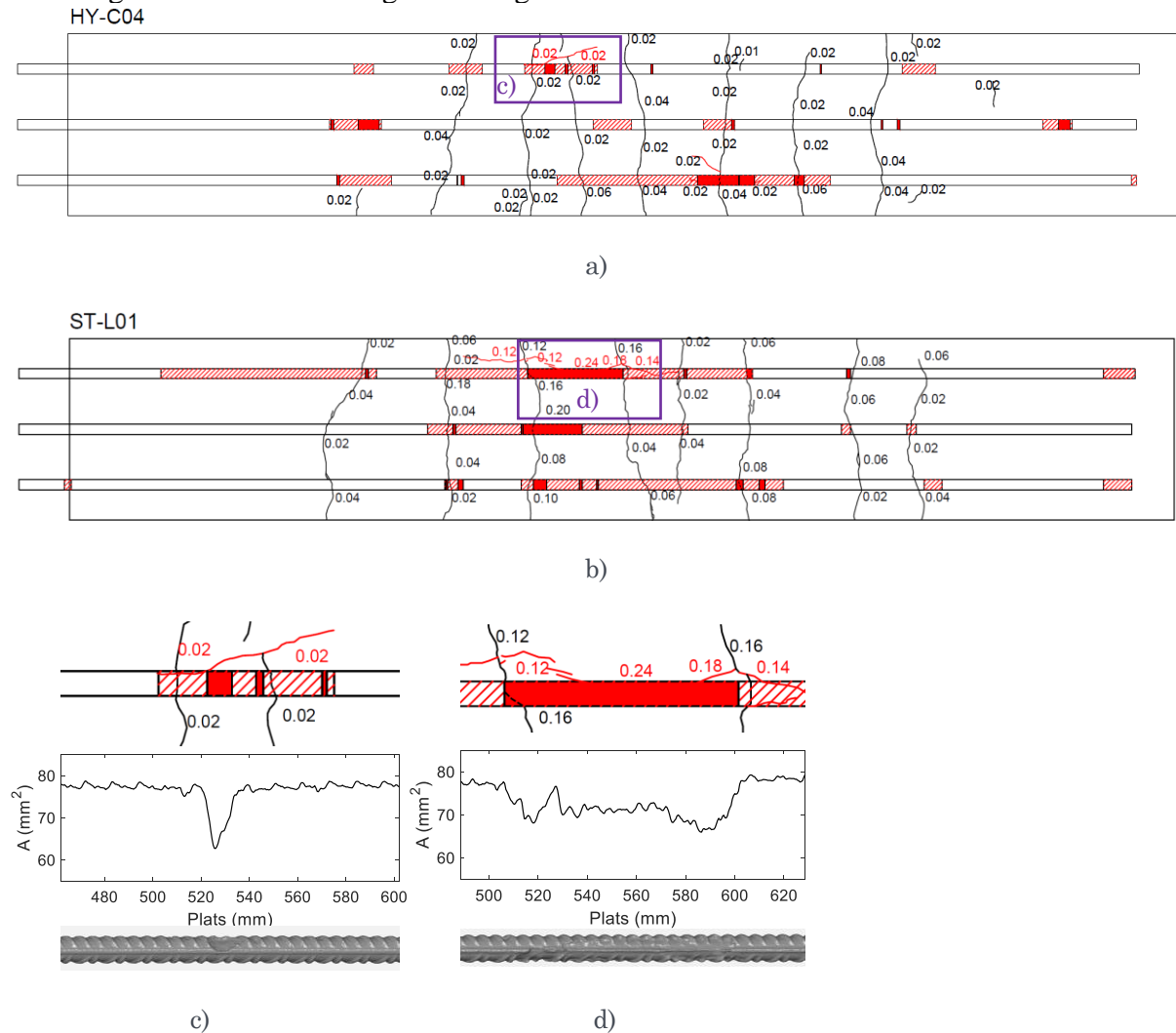
KORROSIONSMÖNSTER RELATERAT TILL SPRICKOR I BETONGEN

Korrosionsnivån μ (definierad som den maximala förlusten av en armeringsstångs tvärsnittsarea) och korrosionsmönster karterades noggrant med hjälp av 3D-scanning. Som framgår av figur 1 är det uppenbart att de tvärgående böjsprickorna accelererade korrosionen. Det gick dock inte att påvisa någon tydlig korrelation mellan den maximala sprickvidden för böjsprickorna (0,1 och 0,4 mm) och korrosionsnivån. Alla balkarna i stålfiberserien (ST) hade lägre genomsnittlig korrosionsnivå än motsvarigheterna i serien utan fibrer (PL). Balkarna med en fibermix (HY, syntet och stål) och syntetiska (SY) fibrer visade liknande eller lägre genomsnittlig korrosionsnivå än sina motsvarigheter utan fibrer för den större sprickvidden (0,4 mm). Balkarna med en fibermix visade en stor standardavvikelse (figur 1) som kan ha berott på ojämn fiberfördelning. Det fanns ett avvikande fall, för syntetfibrer och sprickvidd 0,1 mm, som hade högre korrosionsnivå än motsvarande utan fibrer. Det beror troligen på att den balken fått gjutdefekter vid armeringen, eftersom korrosionsnivån var lägre i balken med syntetfibrer och 0,4 mm sprickvidd.



Figur 1 Korrosionsnivå (genomsnittlig och standardavvikelse) för de tre armeringsstängerna i varje balk av de fyra betongsorterna (PL: utan fibrer, ST: stålfibrer, HY: blandade och SY: syntetiska) under olika lastförutsättningar och tidigare maximal sprickvidd. (Notera: korrosionsnivån representerar maximal lokal förlust av tvärsnittsarean.).

Vi kunde också identifiera ett samband mellan korrosionsmönster och längsgående sprickor som uppkommit på grund av rostens volymexpansion [3]. En längre gropfrätning visade sig hänga samman med en längre och vidare längsgående spricka (figur 2). Resultaten indikerar ett tidsberoende i hur sprickor påverkar korrosionsutvecklingen – följande hypotes ställdes upp: I ett tidigt skede påverkar tvärgående sprickor och ger främst lokaliserad gropfrätning. Dessa leder till längsgående korrosionsinducerade sprickor, som i sin tur med tiden ger upphov till mer generell korrosion längs armeringen.



Figur 2 Exempel som visar hur sprick- och korrosionsmönster karterades.

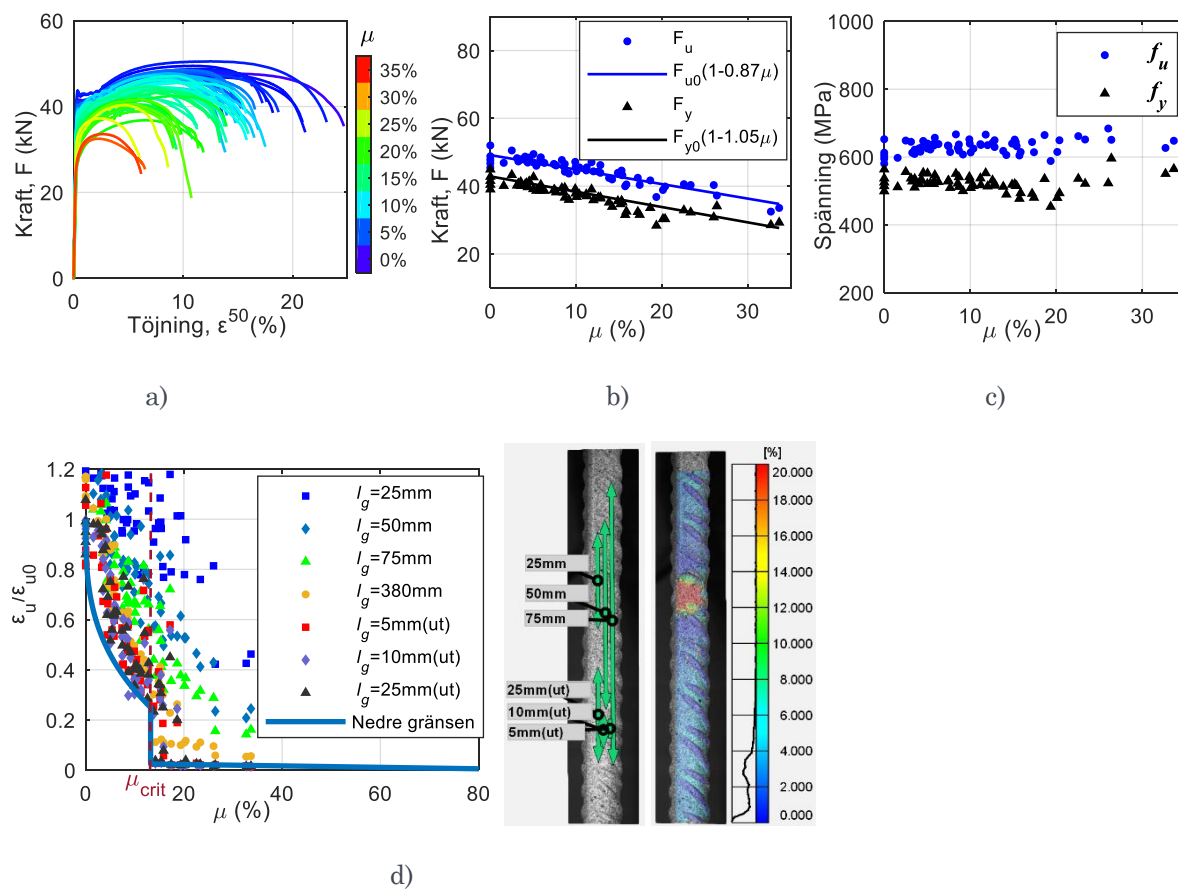
Resultat från dragprover av de korroderade armeringsstängerna sammanfattas i figur 3. Med ökande korrosionsnivå visar kraft-töjningskurvan tidigare flytning, och att den markerade flytplatån successivt minskar och försvinner (figur 3a). Flyt- och maxlast (F_y , F_u) minskade linjärt med korrosionsnivån, medan flyt- och maxspänning (f_y , f_u), baserade på den återstående tvärsnittsarean, var konstanta oavsett korrosionsnivå, med en viss spridning - se figur 3b och 3c. Jämfört med lastkapacitet minskade deformationskapaciteten mer drastiskt med ökande korrosionsnivå. Töjningen vid max lastkapacitet (ϵ_u) beror även på hur den mäts, eftersom

³ Chen E, Berrocal CG, Löfgren I, Lundgren K. Correlation between concrete cracks and corrosion characteristics of steel reinforcement in pre-cracked plain and fibre-reinforced concrete beams. *Materials and Structures*. 2020;53

töjningen inte är jämnt fördelad över stången – detta visades med hjälp av Digital Image Correlation (DIC); se figur 3d. Försöken visade även att det finns en kritisk korrosionsnivå för gropfrätning: för större lokala korrosionsnivåer blir deformationsförmågan mycket begränsad. Det beror på att stålet når flytning enbart i det område som är angripet av gropfrätning – flytningen sprider sig alltså inte till resten av armeringsstången. Genom en enkel jämviktsbetraktelse visades att denna kritiska korrosionsnivå är:

$$\mu_{crit} = 1 - \frac{f_{y0}}{f_{u0}}$$

där f_{y0} är stålets flytgräns och f_{u0} är stålets sträckgräns, båda för armeringsstänger utan korrosion. För de provade stängerna var denna kritiska korrosionsnivå 13.3%. Vidare jämviktsbetraktelser ledde till en enkel modell som kan användas för att på säkra sidan uppskatta deformationsförmågan för en armeringsstång med gropfrätningar. Denna nedre gräns för deformationsförmågan fås direkt ur materialets arbetskurva, se figur 3d. För detaljer, se [4].



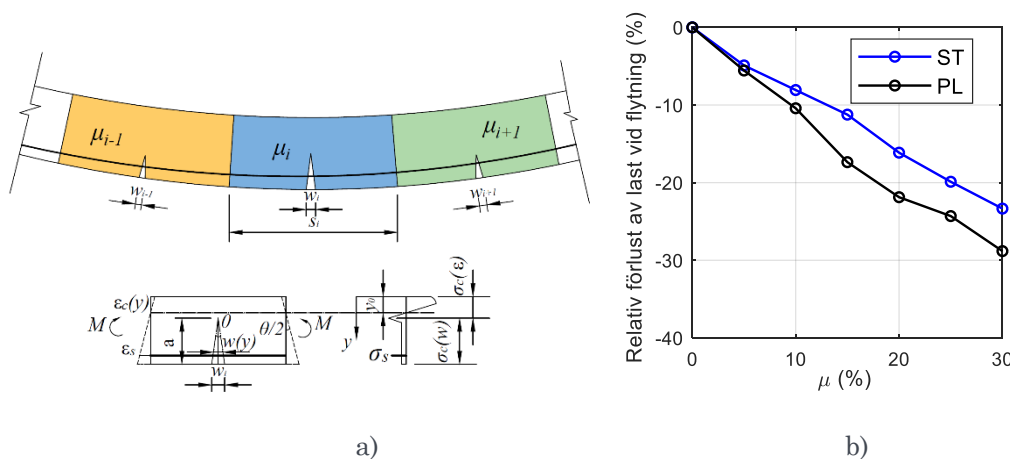
Figur 3 Resultat från dragprover av korroderade armeringsstänger: a) Kraft mot töjning för varierande korrosionsnivåer; b) Flyt- och maxlast (F_y och F_u) mot korrosionsnivå, F_{y0} och F_{u0} är flyt- respektive maxlast för okorroderad armeringsstång; c) flyt- och maxspänning (f_y och f_u) mot korrosionsnivå; d) normaliserad töjning vid maxlast (ϵ_u/ϵ_{u0} , där ϵ_{u0} är för okorroderad armeringsstång) mot korrosionsnivå mätt över olika mätlängd

⁴ Chen E, Berrocal CG, Fernandez I, Löfgren I, Lundgren K. Assessment of the mechanical behaviour of reinforcement bars with localised pitting corrosion by Digital Image Correlation. *Engineering Structures*. 2020;219:110936

l_g och den provade stångens totala längd $l_g=380$ mm. Dessutom visas den nedre gränsen härledd i [3], med den kritiska korrosionsnivån μ_{crit} markerad.

MODELLERING AV BÄRFÖRMÅGA

Lokaliserad gropfrätning minskar armerade betongkonstruktioners bärförmåga, deformationskapacitet och därmed säkerhet. Särskilt allvarligt blir det om förvarning om pågående korrosion genom spräckta täcksikt saknas. För att bedöma bärförmågan hos hybridarmerade betongbalkar utvecklades en modell som baseras på ett koncept med icke-linjära leder och där modellen som togs fram i [3] användes för att ge arbetskurvan för korroderade stänger. För den fiberarmerade betongen användes en bilinjär arbetskurva efter uppsprickning. En balk delades upp i en serie icke-linjära leder, där antalet berodde på de tvärgående sprickorna (figur 4a). Korrosionsnivån på armeringen i varje led tilldelades separat för att motsvara varierande gropfrätningar längs stängerna. För varje led bestämdes moment och krökning ($M_{i-\kappa_i}$) samband, detta beräknades utifrån korrosionsnivån μ_i och jämvikts- och kompatibilitetsförhållandena för det spruckna tvärsnittet. Under ett givet lastfall (till exempel trepunkts- eller fyrapunktsböjning) kan krökningsfördelning, rotation och balkens nedböjning lösas. Modellen validerades först mot tidigare försöksresultat för hybridarmerade betongbalkar, både med och utan armeringskorrosion. Därefter utfördes en parameterstudie för att undersöka effekten av korrosionsnivå och gropfrätningars placering på bärförmågan. Givetvis är gropfrätningar farligast då de är placerade i maxmomentssnitt, i dessa fall mitt i balken. Resultaten av parameterstudien visar att jämfört med den traditionellt armerade betongbalken behöll den hybridarmerade betongbalken en större andel av sin ursprungliga bärförmåga, se figur 4b.



Figur 4 a) Modell för bärförmåga med icke-linjära leder; b) Resultat i form av relativ förlust av last vid flytning för balkar under tre-punkts böjning (med samma geometri och materialegenskaper som balkarna i [1], PL: utan fibrer, ST: stålfibrer).

FALLSTUDIE PÅ KANTBALKAR

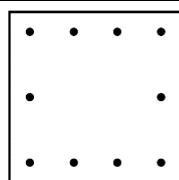
En fallstudie genomfördes på kantbalkar på broar. Kantbalkar har en avsevärt kortare livslängd än broars avsedda livslängd, huvudsakligen på grund av armeringskorrosion som orsakar långsgående sprickor och avspjälkning av täcksikt. Olika alternativa kantbalkar, med

varierande armeringsutformning och stålfibermängd utformades, se tabell 1. Momentkapacitet, sprickvidd och livslängd beräknades för alla alternativ. Livslängden beräknades utifrån initieringstid för korrosion genom kloriddiffusion och hur lång tid den korrosionsinducerade sprickbildningsprocessen tar. Samma kloriddiffusion användes för den ospruckna betongen oavsett om den innehöll fibrer eller ej, baserat på de tidigare försöksresultaten [1]. I sprucken fiberarmerad betong visade det sig denna vara 33 % mindre än den i sprucken betong utan fibrer. Tillväxten av korrosionssprickor studerades i finita elementanalyser. Analyserna visade att sprickvidden för de längsgående sprickorna blev betydligt mindre i hybridarmerad betong, särskilt för alternativet med 1,0% volym stålfibrer och liten diameter på armeringsstängerna.

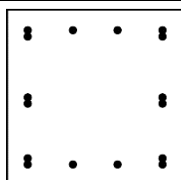
Baserat på dessa beräkningar kan livslängden för en kantbalk förlängas med mer än 58 % genom användning av fibrer (se tabell 1).

Tabell 1 Alternativa utformningar i fallstudien och beräknad livslängd

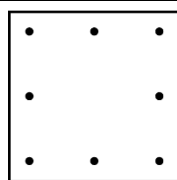
Alter-nativ	Arme-ring	v_f (% vol.)	A_s (mm^2)	f_{ct} (MPa)	$f_{Ft,SLS}$ (MPa)	$f_{Ft,ULS}$ (MPa)	M_u (kNm)	w_{cr} (mm)	Livslängd (år)
PL1	10Ø16	0	2011	3.5	0	0	153	0.51	50
PL2	16Ø16	0	3217	3.5	0	0	221	0.28	44
FRC1	10Ø16	0.5	2011	3.5	2.0	1.5	201	0.21	97
FRC2	8Ø16	0.5	1608	3.5	2.0	1.5	167	0.27	79
FRC3	8Ø16	1.0	1608	3.6	3.0	2.4	197	0.13	102
FRC4	10Ø12	1.0	1131	3.6	3.0	2.4	173	0.15	127



PL1, FRC1, FRC4



PL2



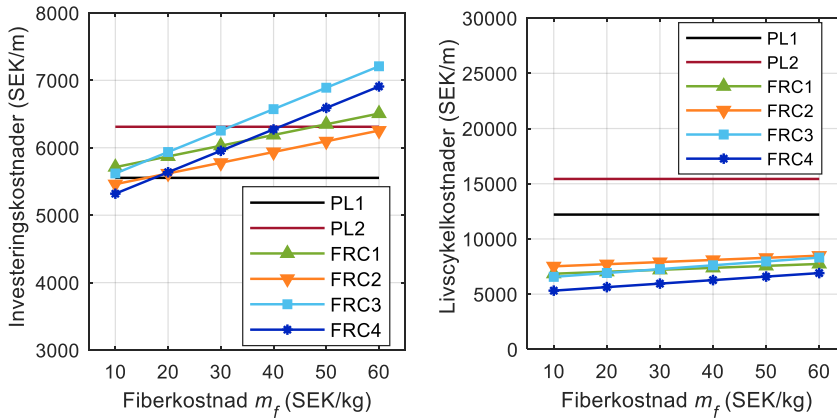
FRC2, FRC3

Armeringsutformning

Notera: v_f är volymsinnehåll fibrer, A_s är armeringsarea, f_{ct} är betongens draghållfasthet, $f_{Ft,SLS}$ är fiberbetongens residualdraghållfasthet i bruksgräns, $f_{Ft,ULS}$ är fiberbetongens residualdraghållfasthet vid en sprickvidd om 2,5 mm (brottgräns), M_u är momentkapacitet och w_{cr} är den maximala sprickvidden på grund av tvång.

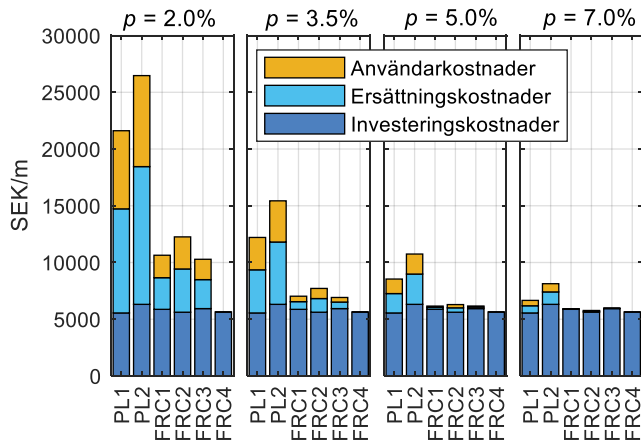
Vidare utfördes analys av livscykelkostnaden (LCC) med beaktande av Investeringskostnader, Ersättningskostnader och Användarkostnader, med varierande värden på fiberkostnaden (10-60 SEK/kg), diskonteringsränta (p) och genomsnittlig dygnstrafik (ADT). Vid högre fiberkostnader (≥ 30 SEK/kg, vilket är högre än det normala marknadspriset om cirka 15-25 SEK/kg), är investeringskostnaderna för alla hybridkonstruktioner högre än de traditionella. Trots det är den totala livscykelkostnaden för alla alternativen med hybridarmering mindre än de traditionella alternativen, på grund av minskade Ersättnings- och Användarkostnader; se figur 5a och 5b. Fördelen med att minska LCC genom att använda hybridarmering blir

dessutom större vid lägre diskonteringsränta. Genomsnittlig dygnstrafik har ett mindre inflytande (figur 5c och 5d).

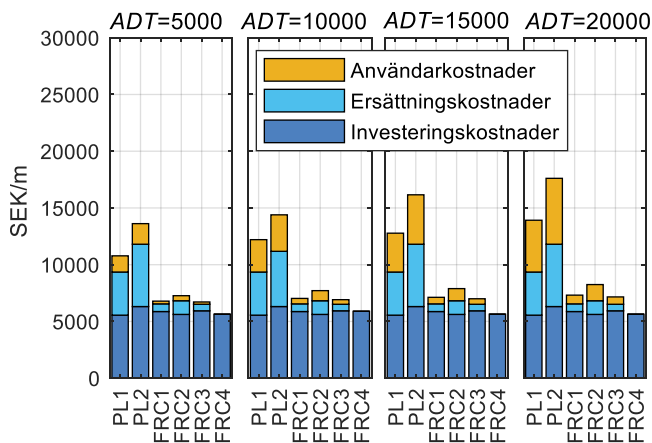


a)

b)



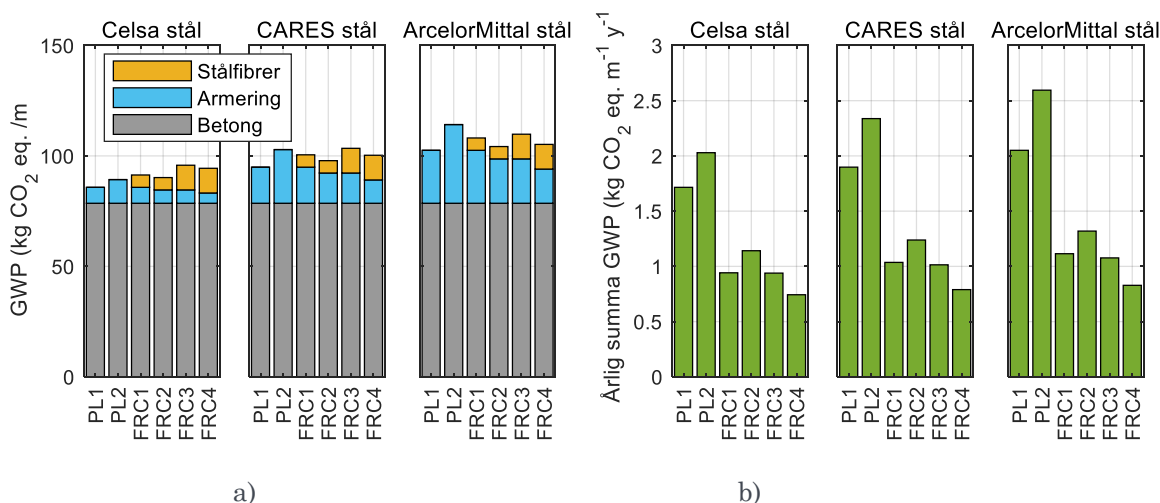
c)



d)

Figur 5 Inverkan av fiberkostnader på a) investeringskostnader och b) totala livscykelkostnader; c) inverkan av diskonteringsräntan p när genomsnittliga dygnstrafiken ADT=10000 fordon/dag och fiberkostnaden är 20 SEK/kg; d) inverkan av den genomsnittliga dygnstrafiken ADT när diskonteringsräntan $p=3.5\%$ och fiberkostnaden är 20 SEK/kg (Bron antogs vara 15 m lång med 120 års livslängd).

Slutligen bedömdes den miljöpåverkan som indikeras av GWP (Global Warming Potential) per meter av kantbalken från materialproduktionen av olika alternativ genom livscykelanalys, se resultat i figur 6. Olika tillverkare av armeringsstänger rapporterar varierande värden på GWP, därför undersöktes denna variation. I allmänhet står betongen för majoriteten av den totala GWP, vilket gör att skillnaden av den totala GWP mellan olika alternativ blir måttlig. Men den årliga totala GWP är betydligt lägre i de hybridarmerade alternativen på grund av deras längre livslängd.



Figur 6 a) Global warming potential (GWP) från betong, armering och stålfibrer, and b) årlig total GWP i vart och ett av alternativen (enhets-GWP för betong från Svensk Betong är $388 \text{ kg CO}_2/\text{m}^3$, enhets-GWP av stålfibrer från Mapei är $0.703 \text{ kg CO}_2/\text{kg}$, enhets-GWP av armering är $0,37$, $0,839$ och $1,23 \text{ kg CO}_2/\text{kg}$ från Celsa, CARES respektive ArcelorMittal).

SLUTSATSER

Det aktuella projektet förstärker och bekräftar de tidigare positiva resultaten om användning av hybridarmerade konstruktioner i kloridhaltiga miljöer. Försök visade att de allra flesta armeringsstångerna i fiberarmerade betongbalkar hade lägre korrosionsnivå än motsvarande utan fibrer. Modeller för konstruktioners säkerhet och livslängd utvecklades, och de visar att hybridarmerade alternativ bibehåller både bärförmåga och beständighet (mätt i form av när armeringskorrosion spräcker täcksikt) bättre än traditionella lösningar. Följaktligen ger hybridarmerade konstruktioner en mer ekonomisk och hållbar lösning i kloridhaltiga miljöer genom dess ökade livslängd jämfört med traditionellt armerade betongkonstruktioner. Med den modell som utvecklades för att beskriva arbetskurvan för korroderade stänger och den för att bedöma bärförmåga och deformations-/rotationskapacitet kan effekten av korrosion undersökas både för konventionella och hybridarmerade konstruktioner.

Publikationer inom projektet:

Chen E., Berrocal, C. G., Löfgren I., & Lundgren K. (2020): Correlation between concrete cracks and corrosion characteristics of steel reinforcement in pre-cracked plain and fibre-reinforced concrete beams. *Materials and Structures* (2020) 53:33.

<https://doi.org/10.1617/s11527-020-01466-z>

Chen E., Berrocal, C. G., Fernandez I., Löfgren I., & Lundgren K. (2020): Assessment of the mechanical behaviour of reinforcement bars with localised pitting corrosion by Digital Image Correlation. *Engineering Structures* 219(2020).

https://research.chalmers.se/publication/517647/file/517647_Fulltext.pdf

Chen E., Berrocal, C. G., Löfgren I., & Lundgren K.: Comparison of the service life, life-cycle costs and assessment of hybrid and traditional reinforced concrete through a case study of bridge edge beams in Sweden. *Structure and Infrastructure Engineering* 2021.

<https://www.tandfonline.com/doi/full/10.1080/15732479.2021.1919720>

Chen E., Berrocal, C. G., Löfgren I., & Lundgren K. (2020): *Corrosion Pattern and Mechanical Behaviour of Corroded Rebars in Cracked Plain and Fibre Reinforced Concrete*. P. Serna et al. (Eds.): BEFIB 2020, RILEM Bookseries 30, pp. 477–488, 2021.

https://doi.org/10.1007/978-3-030-58482-5_44

Chen E., Berrocal, C. G., Löfgren I., & Lundgren K. (2020): Hybridarmerade konstruktioner i kloridhaltiga miljöer – beständighet, säkerhet och livscykelkostnader. *Bygg & teknik* 6/2020.

Examensarbeten genomförda inom projektet:

Cassavia G. (2020): *Structural analysis of hybrid reinforced concrete beams with reinforcement corrosion*. Department of Civil Engineering, Architecture, Environment, Land Planning and Mathematics, University of Brescia.

Henriksson R., & Åhs M. (2019): *Effect of Cracks and Fibres on Reinforcement Corrosion – Edge beam application*. Master's thesis in Master Program Structural Engineering and Building Technology, Chalmers University of Technology. Master's thesis ACEX30-19-25.

<https://hdl.handle.net/20.500.12380/257459>

Chen E., Berrocal, C. G., Löfgren I., & Lundgren K. (2020): Correlation between concrete cracks and corrosion characteristics of steel reinforcement in pre-cracked plain and fibre-reinforced concrete beams. *Materials and Structures* (2020) 53:33.

CORRELATION BETWEEN CONCRETE CRACKS AND CORROSION CHARACTERISTICS OF STEEL REINFORCEMENT IN PRE-CRACKED PLAIN AND FIBRE-REINFORCED CONCRETE BEAMS

E Chen^{1*}, Carlos G. Berrocal^{1,2}, Ingemar Löfgren^{1,2}, Karin Lundgren¹

¹Chalmers University of Technology, Division of Structural Engineering, Göteborg, SE-41296, Sweden

²Thomas Concrete Group AB, Södra Vägen 28, Göteborg, 41254, Sweden

ABSTRACT

This paper presents results on corrosion characteristics of 66 rebars extracted from un- and pre-cracked plain concrete and fibre-reinforced concrete (FRC) beams suffering from corrosion for more than three years. The influences of fibre reinforcement, flexural cracks, corrosion-induced cracks and loading condition on the maximum local corrosion level (defined as the maximum cross-sectional area loss percentage) and pit morphology were examined. With 3D-scanning, the corrosion characteristics were analysed, and pit types were classified based on the maximum local corrosion level and geometric parameters of pits. Corrosion pits were observed near some flexural cracks, while the bars at other cracks were free from corrosion. Most rebars in FRC had less maximum local corrosion level than those in plain concrete under the same loading condition and target crack width. However, the maximum local corrosion level was not dependent on the flexural crack width (0.1 and 0.4 mm). Longitudinal cracks aggravated the total steel loss and changed the pit morphology by promoting the pit length development. However, longitudinal cracks did not always form, even with severe pitting corrosion. A hypothesis about the time-dependent interplay between transverse and longitudinal cracks and corrosion development was proposed. Further studies on predicting the pitting corrosion evolution and experimental work on specimens exposed for longer periods are needed to understand and quantify the long-term durability of concrete structures reinforced with both conventional reinforcing bars and fibres.

Keywords: Pitting corrosion; 3D-scanning; Fibre-reinforced concrete; Corrosion-induced cracks.

1. Introduction

Corrosion of reinforcement in concrete structures is a major problem affecting the durability of reinforced concrete (RC) structures, particularly for those in marine environments or exposed to de-icing salts [1]. External agents such as chloride, CO₂, oxygen, and water, can penetrate concrete cover. When the chloride concentration near the rebar surface reaches a critical value or the carbonation front advances over time to the rebar's depth, the passive film on the reinforcement is destroyed, after which corrosion initiates [2].

Moreover, in practice RC structures inevitably have cracks, originating from such things as shrinkage, thermal gradients and/or mechanical loading. These cracks provide preferential paths for the ingress of external agents [3,4], which shortens the corrosion initiation period and induces localised corrosion near the cracks [5,6]. However, the long-term impact of cracks on the corrosion propagation phase has not been clarified and is still under debate [7]. As discussed in the state-of-the-art review [7], some studies reported that the corrosion rate increased with the

crack width [6,8,9], while other studies indicated that cracks did not enhance the corrosion process or that the enhancing effect diminished with time [10,11].

Although the importance of crack width on reinforcement corrosion is not completely clear, to limit the risk of corrosion, current codes [12,13] dictate the minimum cover depth and maximum allowable crack width, based on the class of environment aggressiveness. The restrictive requirement of controlling crack width for civil engineering structures exposed to marine environments or de-icing salts (such as harbour piers or bridges) often results in congested reinforcement layouts. These are costly and difficult to handle on-site. In such cases, an attractive alternative could be the use of fibre reinforcement combined with conventional reinforcement. Fibres are an effective means of crack control through fibre bridging [14]. They can also improve the mechanical performance of concrete structures [15]. Nevertheless, the corrosion performance of conventional reinforcement in FRC in chloride environments is not yet fully understood. In [16], fibre-reinforced cementitious composites (FRCC) with a 1.5% fibre volume fraction were found to delay the corrosion initiation and reduce the corrosion amount, compared to plain mortar under the same impressed voltage. Further, it was shown in [17] that bars in FRC with a 1.5% fibre volume fraction had longer corrosion initiation times and a lower active corrosion rate compared to bars in plain concrete at the same flexural load.

An earlier study by the authors [18] investigated the effect of various types of fibres (with a volume fraction of <1%) on the corrosion initiation time of steel bars in pre-cracked beams. Unlike other studies [16,17], the maximum surface crack width produced by three-point bending was kept the same for plain RC and FRC beams. This made it possible to examine the effect on steel corrosion of crack characteristics such as crack pattern and internal crack morphology in FRC. The impact of the width of surface crack was also studied by setting the target crack width (maximum flexural crack width) to 0.1, 0.2, 0.3, and 0.4 mm. Experimental results showed a tendency towards earlier initiation of corrosion, with increasing crack widths. A small improvement (in terms of delayed corrosion initiation) was observed when fibres were added. In the subsequent study [19], the flexural behaviour of corroded plain RC and FRC beams (among the specimens in [18]) was examined. FRC beams were found to display higher residual load capacity at reinforcement yielding than plain RC beams, whereas the relative loss of load capacity (the loss of load normalised by the load on reference beams) as a function of the maximum local corrosion level was similar to that seen in plain RC beams [19]. However, the relative contribution of the fibres to the residual capacity of FRC beams and mechanical behaviour of corroded rebars could not be investigated specifically, as it was not possible to evaluate the mechanical behaviour of those rebars accurately after the flexural capacity tests. Following the tests, the corrosion level of critical rebar segments was evaluated using 3D-scanning [19]. However, no clear trend was identified in maximum local corrosion levels regarding i) fibre addition, ii) targeted crack widths of 0.2 and 0.3 mm and iii) loading type. This was partly due to the limited number of specimens. Thus, further studies on the correlation between concrete cracks and the corrosion behaviour of rebars in plain RC and FRC beams should focus on achieving a better understanding of the influence of cracks and fibres on the corrosion process.

The present study is a continuation of previous ones [18,19]. The purpose was to examine the effect of cracks and fibres on the corrosion characteristics of rebars from the remaining uncracked and cracked specimens, with target crack widths of 0.1 and 0.4 mm prepared in [18]. In particular, a 3D-scanning technique was used to obtain the pit morphology. This enabled detailed geometrical parameters to be determined for each pit (including the maximum cross-sectional area loss, pit depth, pit length and pit volume) and represent the corrosion condition. When discussing the influence on reinforcement corrosion of such factors as concrete binder type

and cracking [6,8,20,21], most existing studies use a definition of “corrosion level” that refers to either “corrosion rate” (measured using electrochemical techniques), or “corrosion amount” (often calculated as the weight loss). However, the corrosion rate measured from electrochemical methods may give inaccurate estimation on the local corrosion state if the actual extent of the anodic area in the rebar is not known [22,23]; this may render the conclusions regarding various factors on the corrosion propagation not reliable. Further, it is the pit characteristics that determine the consequences of steel corrosion, including the mechanical properties of corroded rebars, corrosion-induced cover cracking and concrete-steel bond behaviour and, hence, the overall structural performance. Understanding the influence of various factors on pit morphology will increase the reliability of conclusions as to their effects on structural durability and safety.

2. Experimental programme

2.1. 2.1 Specimens description

The specimens in this study were 1100 mm long beams with cross-sectional dimensions of 180 x 100 mm². Each beam was reinforced with three Φ 10 mm “as-received” ribbed rebars, positioned with a clear concrete cover of 30 mm. The end of the bars embedded in the beam had a distance of 30 mm away from the beam end whereas the other end of the bars stuck out 50 mm to enable an electrical connection for the corrosion monitoring equipment. The geometry of the specimens, including the reinforcement layout, is illustrated in Fig. 1. Four different series of specimens were used, one without fibre reinforcement referred to as “plain” (PL) series, and three FRC series with different types of fibre reinforcement, referred to as “steel” (ST), “hybrid” (HY) and “synthetic” (SY) series. The types of fibres used for the different FRC series were 35 mm end-hooked steel fibres for the ST series, 30 mm straight polyvinyl alcohol (PVA) for the SY series and a combination of steel fibres and 18 mm long PVA fibres for the HY series. A self-compacting concrete mix with the same water/cement ratio of 0.47 was used for all the series. The mix proportions are given in Table 1. A total of 54 beams specimens were cast in 2013. After casting, the beams were covered with a polyethylene sheet. After 24 hours, they were demoulded. Subsequently, the beams were wetted and wrapped in geotextile and plastic sheets at room temperature until the age of 10 weeks. After that, the beams were pre-loaded to induce cracking under different loading conditions and subsequently exposed to chlorides except six of the beams kept uncracked and stored in potable water for use as reference samples. In 2017, 32 beams (including the reference beams, some of the uncracked beams and cracked beams with a target crack width of 0.2 and 0.3 mm) were tested structurally to assess their residual flexural behaviour [19]. The remaining 22 beams (including the uncracked beams and cracked beams with a target crack width of 0.1 and 0.4 mm) were investigated in this study.

2.2. 2.2 Load and exposure conditions

The four conditions considered were: (a) uncracked specimens, which were never loaded, (b) specimens that were loaded only once to induced cracking, (c) specimens subjected to five load cycles to promote greater damage at the rebar-concrete interface and (d) specimens initially pre-cracked and subsequently reloaded with a sustained load to keep the cracks open. When referring to their loading conditions, the beams are denoted throughout the paper as “*uncracked*”, “*unloaded*”, “*cyclic*” and “*loaded*”.

The specimens were pre-loaded under three-point bending at age 10 weeks, up to the target crack of 0.1, 0.2, 0.3, and 0.4 mm. During the pre-loading procedure, the widest crack formed on each beam was measured using a crack detection microscope, at 20x magnification and 0.02 mm resolution, to determine when the target crack width was reached. However, in one of the ST beams under “*cyclic*” loading, the maximum crack width reached 0.8 mm instead of the target crack width of 0.4 mm. It should be noted that, in order to reach the same target crack width

under the same loading type, the load applied to FRC series was always greater than that for plain series, see [18]. Upon unloading, the cracks closed to a certain degree and the remaining surface crack width ranged between 0.02 and 0.06 mm, for both the plain and fibre-reinforced specimens. The beams subjected to sustained loading were paired using a clamping setup. This was to keep the target crack width as the widest crack opening during the pre-loading procedure.

The beams were partially immersed in a highly concentrated sodium chloride solution (16.5% NaCl), with approximately three quarters of the beam length submerged. The chloride exposure was conducted cyclically, with two-week wetting cycles followed by two-week drying cycles under laboratory conditions ($20.5\pm 3.6^\circ\text{C}$ and $45\pm 15\%$ RH). Corrosion potentials were monitored hourly with an embedded MnO_2 reference electrode to determine the corrosion initiation time. Corrosion rates were measured based on the galvanostatic pulse technique every 2 weeks in the beginning and every 6 weeks during the last 18 months of the exposure period. Those results have been reported by the authors in previous work [18].

After three years' exposure, all the specimens were removed from the tanks and stored in the laboratory. The reinforcement corrosion continued naturally during storage, as the specimens were fully contaminated by chlorides and showing active corrosion. The corrosion rates were not measured during the storing period; nevertheless, a lower corrosion rate was expected compared to that during the exposure period.

Table 2 summarises the specimens used in this study. Some beams (including the uncracked and six cracked PL beams, and two cracked ST beams) were taken out for testing after being stored in the laboratory for 18 months, while the other 13 beams were tested after 24 months' storage. The six-month time difference between extraction of the rebars may have had minor influence on the total corrosion, but the corrosion characteristics were unlikely to have changed under laboratory conditions in such a short time. This influence is therefore ignored.

2.3. 2.3 Crack mapping

Before extracting bars from the beams, both the flexural cracks and corrosion-induced cracks were mapped. The crack widths of six cracked PL beams and two cracked ST beams were not recorded, whereas the crack widths of other beams were measured with the microscope, as noted in Table 2.

2.4. 2.3 Corrosion characteristics evaluation

After mapping the cracks on the beam surfaces, the beams were broken with a jackhammer and the bars carefully removed. Before cleaning the bars, pit locations and general corrosion regions were measured preliminarily by visual inspection of surface corrosion products. This is because extremely shallow corrosion sites are not easily detected once rust is removed. The corrosion locations were further confirmed and adjusted as necessary, after rust removal by sand-blasting.

The pit locations were identified as positions where the corrosion depth was obviously greater than the surrounding region of rebar surface. The general corrosion regions referred to locations where corrosion products were deposited on the rebar surface but with no obvious localised cavity. Indeed, numerous very tiny pits existed in the general corrosion region but none had developed into an obvious localised pit.

2.3.1 Sand-blasting and gravimetric measurements

The corroded bars were cleaned with sand-blasting to remove corrosion products and adhered concrete. The initial weight of "as-received" bars before casting and final weight of the clean corroded bars were measured using a scale accurate to 0.01 g. The global corrosion level was

determined as the ratio between the gravimetric loss to the initial weight of the bar, according to Equation (1):

$$\mu_g = \frac{k \times m_0 - m_f}{k \times m_0} \quad (1)$$

where μ_g is the global corrosion level, m_0 and m_f are the initial and final steel weights and k is a parameter which takes into account the removal of mill-scale from the initial weight during sand-blasting. The parameter k is taken as 0.9978, which was determined based on the average weight loss of 15 non-corroded, “as-received” bars subjected to mechanical cleaning with wire-bristle brushes to remove mill-scale [19].

2.3.2 3D-scanning technique

After sand-blasting and weight measurements, each bar was cut into two or three segments with an electric rebar cutter. The cutting sections were selected to get a segment with the most severe pit included in the middle region (referred to as “critical segment”) and with a constant length of 500 mm. A few bars presented more than one pit in relatively close proximity and with similar severity. The critical segments of such bars were cut to a length of 550 mm to accommodate both pits within the same segment. Only the critical segment of each bar was 3D-scanned, meaning that pits located in other segments were not studied. Bar selections to cut from the uncracked beams were made differently, as their most severe pit was close to the bar-end embedded in the concrete. However, the end corrosion was not considered in this study; the remaining segment of rebar with the most severe pitting was scanned instead.

The scan was carried out using a portable Handy Scan 700TM laser scanner from Creaform. This equipment features an accuracy of up to 30 μm and a maximum spatial resolution of the generated point cloud of 0.05 mm. Mounted to a fixture outfitted with reference scanning targets, the bar was scanned by swiping the scanner manually around it at an appropriate distance. The surface of the bar was reconstructed with a 3D triangular mesh of the point cloud generated in the scanner’s software. This mesh was repaired in the GOM Inspect software by filling in small holes and removing noise points. A new point cloud was then generated from the repaired mesh for further analysis, using Matlab 2015b commercial software.

The corrosion evaluation procedures are illustrated by the example in Fig. 2. Fig. 2a shows the 3D surface mesh of the scanned bar, whereas Fig. 2b shows the longitudinal variation of cross-sectional area A_c along the bar, obtained via the methodology described in [24]. The regular variation of cross-sectional area in Fig. 2b is due to the transverse ribs on the bar surface. The 3D coordinates of points composing the bar surface are also shown in a 2D plot, with the colour representing the radius of every point, as shown in Fig. 2c. The colour scale showing the magnitude of radius (in mm) appears in the legend on the right of Fig. 2c. The pit location can be clearly identified from the blue range. The pit length l_p is the measurement of the pit along the rebar axis, as shown in Fig. 2c.

To evaluate the corrosion penetration depth (the radius loss) and cross-sectional area loss in the pit, the uncorroded segment covering a complete interval of transverse-rib variation was first identified. An iterative process developed in [19] was used for each section in the pit, to find its original uncorroded section. This involved comparing the healthy part of the corroded section with each section in the uncorroded segment. The original uncorroded section was regarded as the one with the shortest distance to the healthy part of the corroded section, through a set of rigid body transformations (translation and rotation).

The cross-section with the minimum area is marked by a dashed line in Fig. 2c. The appearance of the minimum cross-section with its original uncorroded section is shown in Fig. 2d. The maximum local corrosion level μ_{max} is defined as the area loss percentage at the minimum cross-section:

$$\mu_{max} = \frac{A_0^{min} - A_c^{min}}{A_0^{min}} \quad (2)$$

where A_0^{min} and A_c^{min} are the uncorroded and remaining cross-sectional areas at the minimum cross-section, respectively. Adding the volume loss between two consecutive cross-sections along the pit length l_p gives the approximate total volume loss in the pit:

$$V_p = \sum_{i=1}^{N-1} \frac{1}{2} [(A_0^{i+1} - A_c^{i+1}) + (A_0^i - A_c^i)] \Delta l \quad (3)$$

where Δl is the interval distance between two consecutive cross-sections (which is a constant value), A_0^i and A_c^i are the original and remaining area of the i^{th} cross-section in the pit and N is the total number of cross-sections within the pit length l_p .

The pit depth x_p is defined as the maximum radius loss at the minimum cross-section:

$$x_p = \max (r_0(j) - r(j)) \quad (4)$$

where $r_0(j)$ and $r(j)$ are the original and final radii at point j on the minimum cross-section.

3. Classification of pit morphology

To show how pit morphology is influenced by cracks, loading condition and fibres in the following sections, the pits have been classified according to their geometric characteristics. In the general field of metal corrosion, pit shapes are usually described as conical, hemispherical and saucer-shaped, but they may be completely irregular [25]. Fig. 17 in the Appendix shows the common pit shapes for steel and many associated alloys, with the characteristic descriptions for each type. The pit shapes found on 66 bars in this study belong to the “elliptical” and “shallow, wide” types in Fig. 17, with the exception of two special pits which showed the “subsurface” shape. Six types of pit were classified from the parameters of maximum local corrosion level μ_{max} , pit depth x_p and pit length l_p (illustrated in Table 3). Colours representing the pit types in Table 3 will be used in the figures below to show the pit types.

Three intervals of the maximum local corrosion level were defined: $\mu_{max} \leq 5\%$, $5\% < \mu_{max} \leq 10\%$, and $\mu_{max} > 10\%$ corresponding to “light”, “moderate”, and “severe” corrosion, respectively. Furthermore, the pit depth and pit length relative to the nominal radius r_0 and nominal diameter d_0 of steel bars were used to reflect pit morphology. Type 1 represents tiny pits with $\mu_{max} \leq 5\%$, $x_p < r_0/5$ and $l_p < d_0/2$. Usually, multiple tiny pits could be found, albeit isolated from each other. For Types 2 and 3, the pitting level is moderate with $5\% \leq \mu_{max} < 10\%$ and $x_p < r_0/3$, but Type 2 refers to small pits isolated from each other, while Type 3 describes multiple small pits concentrated (or connected) in the continuous long region of length $l_p > 2.5d_0$. For Types 4, 5 and 6, the corrosion level is regarded as severe, with $\mu_{max} > 10\%$. Type 4 is characterised by shallow pit depth $x_p < r_0/3$ but longer pit length $l_p > 2.5d_0$, which is close to the shape “shallow, wide” in Fig. 17. Type 5 is characterised by both long pit length and (locally) greater pit depth, with either an elliptical pit shape embedded in a long pit or an elliptical pit located next to a long pit. Type 6 is characterised by a greater pit depth $x_p > r_0/3$ but short pit length $l_p < 2.5d_0$, showing a typical “elliptical” shape.

4. Results and discussions

4.1. Overview of crack pattern and corrosion pattern

4.1.1 Location of cracks and pits

The crack pattern of concrete surface and corrosion pattern of bars were drawn simultaneously, so as to view the correlation between their locations. Fig. 3 illustrates the crack pattern on the tension surface (the surface under tension during three-point bending) and corrosion pattern of plain series under the “*uncracked*”, “*unloaded*”, “*cyclic*”, and “*loaded*” conditions, with 0.4 mm target crack. The mix series, loading condition, and target crack width are included in the name of each specimen label. The four load conditions “*uncracked*”, “*unloaded*”, “*cyclic*”, and “*loaded*” are represented by “N”, “U”, “C”, and “L” respectively. For example, PL-N represents the uncracked plain series beam, PL-U0.4 represents the plain series beam with “*unloaded*” condition and 0.4 mm target crack. Fig. 4 shows the crack-corrosion pattern of steel fibre, hybrid fibre and synthetic fibre series under the “*unloaded*” condition, with 0.4 mm target crack.

All the bars, including those in *uncracked* beams, were corroded. Corrosion in the “*uncracked*” beams was light for all mix series but many of the rebars in “*uncracked*” beams (see PL-N in Fig. 3) showed severe pitting corrosion at the end of the bar embedded in concrete (see Fig. 18a in the Appendix). In cracked beams, light to severe pitting corrosion was found. Pitting corrosion is usually accompanied by general corrosion in the surrounding region. An example of this appears in Fig. 18b. As seen in Fig. 3 and Fig. 4, several pits were formed on separate sites of a bar, with most pits located at the flexural cracks. However, some pits were located at a short distance from the transverse cracks. It is noteworthy that in approximately half of the flexural cracks, no corrosion was found. This is probably due to the mechanism described in [26], which suggests that corrosion is induced at the widest crack or weakest position first, which delays and suppresses corrosion in other cracks.

4.1.2 Rust stains and fibre corrosion

In most cracked beams, rust stains were found near some corrosion-induced cracks (also commonly called longitudinal or splitting cracks), but no cracks were fully filled with corrosion products. For the fibre-reinforced series including steel fibres (ST and HY series), rust stains were distributed at numerous spots on the beam surface due to fibre corrosion, but no corrosion could be found on steel fibres embedded in the cover. It has been found that steel fibres have better corrosion resistance than reinforcement bars. This is probably due to there being fewer defects on the fibre surface and a more uniform fibre-matrix interface [27]. However, the long-term corrosion resistance and corrosion behaviour of steel fibres across cracks need further investigation, especially when the crack widths become very large.

4.1.3 Crack characteristics

It was observed that some flexural cracks (less than 0.02 mm width) were partially or fully healed, or filled with white material. They may have been healed by the hydrated products or infilled with salt crystals. These fine cracks were also traced in the crack-corrosion pattern drawings of Fig. 3 and Fig. 4.

For the same loading condition, “*unloaded*” with 0.4 mm target crack width, there were a few more flexural cracks in the fibre-reinforced series than the plain series (Fig. 4). In the previous studies [5,28], increasing crack frequency decreased the local corrosion rate at each corroding spot, because the crack distance limited the cathodic area available to contribute to the macro-cell current. The flexural crack spacing on beams in this study varied between 40 to 110 mm, and the average crack spacing in fibre series beams was slightly shorter. Since the flexural crack spacing on one beam was not uniform and the difference in the average crack spacing between plain series and fibre-reinforced series was small (less than 2x, see Fig. 3 and Fig. 4), the

influence of crack spacing on the corrosion level of each pit along a rebar was not examined. Only the local corrosion level of the most severe pit along each rebar was focused in this study.

Corrosion-induced cracks were found in most beams. They were short in length, localised at severe pits and most of their widths were greater than those of the flexural cracks, as observed in Fig. 4. The flexural cracks crossing the longitudinal cracks were found to have greater widths than other flexural cracks (ones that did not cross corrosion-induced cracks). Thus, the flexural cracks most likely opened due to the creation of longitudinal cracks under corrosion expansion.

4.1.4 Mapping cracks and the cross-sectional area variation

To examine the correlation between cracks and pit morphology, the crack widths, longitudinal variation of the remaining cross-sectional area of rebar and the pit morphology were mapped in the same plot. Fig. 5 gives three examples of severe pits exhibiting different shapes, with the pit parameters (μ_{max} , V_p , and l_p) marked. From the definition given in Table 3, the pit in Fig. 5a is Type 6, being of elliptical shape and short pit length, while the pits in Fig. 5b and Fig. 5c are Type 5, as they are both long and deep. The pit length l_p and pit volume V_p increase from Fig. 5a to Fig. 5c. The extent (including length and width) of corrosion-induced cracks also increases from Fig. 5a to Fig. 5c, with the respective maximum crack widths being 0.02, 0.04 and 0.24 mm. However, the maximum local corrosion level μ_{max} did not follow this increasing order from Fig. 5a to Fig. 5c; the value for Fig. 5b was the greatest, with the values for Fig. 5a and Fig. 5c close behind. The maximum local corrosion level did not seem clearly dependent on longitudinal cracks. Moreover, an association can be identified between the width of longitudinal cracks and the length and volume of pits. Although it is unknown whether longitudinal cracks are induced by long pits or vice versa, there is likely a correlation. This will be further discussed in section 4.4.

4.2. Pitting corrosion parameters

4.2.1 Correlation between the global corrosion level and maximum local corrosion level

The global corrosion level was less than 1.6% for all bars, as the pitting corrosion only affected a small fraction of the rebar and the general corrosion was almost negligible. On the other hand, the maximum local corrosion level ranged from 0 to 34%. Fig. 6 shows the correlation between the global corrosion level and maximum local corrosion level of all bars. The maximum local corrosion level is obviously greater than the global corrosion level for all bars but, otherwise, **no correlation can be found**. Points with similar global corrosion levels may have major differences in the maximum local corrosion levels. This indicates that, for the bars in this study, the pitting corrosion level cannot be deduced from the global corrosion level, as concluded in [29].

4.2.2 Pitting factor

To characterise the localised level of a corrosion pit, the pitting factor or pitting concentration factor α , was calculated. This is defined as the ratio of maximum pit depth x_p to the penetration depth x_u corresponding to homogeneous corrosion for the same amount of iron lost [29-31]. In most of the literature, the area loss is usually obtained from the total mass or volume loss per unit length using the gravimetric method. This assumes the area loss of every cross-section along the measured length to be uniform. Mass loss is measured either for the entire rebar [32] or for short offcuts [10]. Contrary to the traditional gravimetric method, 3D-scanning enables the obtention of area loss at every cross-section. For pitting corrosion with the area loss at every cross-section inside the pit being different, using area loss at the minimum cross-section and the average area loss of the pit would result in different values of x_u . Fig. 7 plots the correlation between the maximum local corrosion level μ_{max} and average corrosion level within the pit length μ_{ave,l_p} . As can be expected, μ_{max} is greater than μ_{ave,l_p} . The values of μ_{ave,l_p} for most pits are less

than 15%, except that of three Type 6 pits which exhibit μ_{ave,l_p} values greater than 20%. Those three pits have a large area loss at every cross-section within the pit. Additionally, the average corrosion level of most pits with maximum local corrosion level μ_{max} within 10-25% is close to 10%. This means averaging the area loss of all cross-sections within the pit would not accurately reveal the maximum local corrosion level.

The equivalent uniform corrosion depth, calculated from the maximum cross-sectional area loss μ_{max} and average area loss in the pit μ_{ave,l_p} is noted as $x_{u,max}$ and $x_{u,ave}$ respectively, as given in Equations (5) and (6):

$$x_{u,max} = \frac{d_0}{2} (1 - \sqrt{1 - \mu_{max}}) \quad (5)$$

$$x_{u,ave} = \frac{d_0}{2} (1 - \sqrt{1 - \mu_{ave,l_p}}) \quad (6)$$

The correlation between the pit depth and equivalent uniform corrosion depth calculated from the above two methods is plotted in Fig. 8. It shows that the points for $x_{u,ave}$ are mostly above those for $x_{u,max}$, which indicates that the pitting factor calculated by $\alpha_{max} = x_p/x_{u,max}$ is smaller than that of $\alpha_{ave} = x_p/x_{u,ave}$. The ratio $x_p/x_{u,max}$ or $x_p/x_{u,ave}$ is not a constant value (in other words, the data points in Fig. 8 are not linear in their placement) as the pitting factor varies among bars. The histograms of the pitting factor from the two methods were obtained, in order to determine a typical pitting factor value for the bars in this study (see Fig. 9). The results demonstrate that the maximum probability for the pitting factor falls between 4-6 for α_{max} and 8-10 for α_{ave} . As α_{ave} (calculated from the average steel loss in the pit) is closer to the definitions with traditional methods in the literature, its value (8-10) is considered as the pitting factor for rebars in this study and represents highly localised pitting according to [32].

4.3. Comparison of maximum local corrosion level μ_{max}

In this section, the maximum local corrosion levels of rebars from all specimens are compared and statistically analysed to examine the effects of crack width, loading condition and fibre reinforcement. Fig. 10 shows μ_{max} of bars in all beams, with the colour representing the pit type defined in Table 3. For bars with induced longitudinal cracks, the corresponding transverse and longitudinal crack widths are labelled in black and red fonts respectively (note: only crack widths on some of the beams were recorded, as mentioned in section 2.3 and Table 2). Three bars in the same beam are placed together, with the sequence of three bars corresponding to their locations (such as corner bar or middle bar) in the beam, as indicated in the figure. The ST beam under the “cyclic” condition with target crack 0.4 mm was accidentally overloaded during pre-loading, causing the maximum crack width to be about 0.8 mm. The results of that beam are therefore omitted. Also, one bar in each of PL-U0.4, ST-L0.4 and SY-U0.1 were bent too much during the extraction process. Consequently, their local corrosion levels could not be properly evaluated, as it was difficult to straighten the 3D-scanned bar meshes and obtain accurate cross-sections based on the scan results.

As observed in Fig. 10, μ_{max} of bars in the same beam varied significantly. The largest μ_{max} for each beam was mostly on the corner bar, with only one exception. This was anticipated as chloride can diffuse from both the tension surface and the side surface facing the corner bar. Corrosion-induced surface cracks were also generated above many corner bars, as shown in Fig. 3 and Fig. 4. This also accelerated the local corrosion on the corner bar. The effect of corrosion-induced cracks will be described further in section 4.4.

4.3.1 Influence of loading condition

Fig. 11 shows the average value of μ_{max} for bars in the same beam, with the standard deviation represented by the error bars. For PL and ST series involving all three loading conditions (“unloaded”, “cyclic”, and “loaded”), the average μ_{max} is compared for beams with the same mix type and target crack width but different loading conditions. In the four comparison groups, the “unloaded” condition resulted in larger average μ_{max} than the “cyclic” and “loaded” conditions for PL-0.1, PL-0.4 and ST-0.4 groups. At the same time, just for ST-0.1 group, the “loaded” beam had the largest average μ_{max} among the three loading conditions. For HY beams, the average μ_{max} was similar for the “unloaded” and “cyclic” loading types. These results contradict the findings in [19], where the maximum local corrosion levels under the “loaded” and “cyclic” conditions were mostly greater than for the “unloaded” condition. The differing results may be correlated to the additional storage period of nearly two years for specimens in this study compared to those in [19]. However, the mechanism behind this needs to be further explored.

From Fig. 10, pit Types 5 and 6, both of which have a locally deep pit depth, are dominant for the “unloaded” condition, whereas more pits belonging to Types 3 and 4 (both of which have long pits but shallow depth) were found for the “loaded” case. The long pit length formed on bars in “loaded” beams may relate to the greater extent of slip and separation between concrete and steel, while a more localised pit is likely to form where lesser damage is caused under the “unloaded” condition. Moreover, the pressure generated from corrosion products is also influenced by the interface damage and opening of flexural cracks, as both can provide additional space for corrosion products. In this aspect, corrosion-induced cracks may be larger in “unloaded” beams than “loaded” ones. Unfortunately, no information was available on the corrosion-induced cracks in the most relevant beams, so it was not possible to compare the width of corrosion-induced cracks under the “unloaded” and “loaded” conditions. If the argument is valid, that a greater corrosion-induced crack width may be formed under the “unloaded” condition, then the corrosion level of bars in “unloaded” beams may be increased more by corrosion-induced cracks than in “loaded” beams.

4.3.2 Influence of flexural crack width

From Fig. 10 and Fig. 11, it is obvious that uncracked beams have a smaller μ_{max} than pre-cracked ones. It should be noted that the pitting corrosion at the ends of bars in uncracked beams was not considered. No obvious dependency of μ_{max} on the target crack width of 0.1 and 0.4 mm was observed in Fig. 10 and Fig. 11. Further, the distribution of μ_{max} values is compared for bars in uncracked and cracked beams. The results from the ST beam cyclically loaded by accident to an 0.8 mm crack width were also used, as they contribute to the limited available data for μ_{max} under larger crack widths. Fig. 12a shows the histograms of μ_{max} for uncracked (zero crack width), target cracks of 0.1 and 0.4 mm and a maximum crack of 0.8 mm. From Fig. 12a, all bars in the uncracked beams had μ_{max} value of less than 10% and the three bars under target crack width of 0.8 mm all had μ_{max} greater than 20%. However, the relative frequency distribution of μ_{max} differed, to merely a small extent, for target crack widths of 0.1 and 0.4 mm.

4.3.3 Influence of fibres

From Fig. 11, it can be seen that ST series consistently showed a lower average μ_{max} than PL series under the same loading condition and target crack width. HY series and SY series had similar or lower average μ_{max} than PL series under the target crack width of 0.4 mm. However, the opposite was true under the target crack width of 0.1 mm. This suggests fibre reinforcement may be more effective in reducing the corrosion level when the achieved crack width is larger.

Fig. 12b gives the histograms of μ_{max} for the four concrete mix series. For PL series, the relative number of bars with μ_{max} of 10-20% was higher than that with μ_{max} lower than 10%. However,

the opposite was the case for fibre series. This shows that more bars from beams in PL series presented severe pitting corrosion than those in FRC series. However, the relative frequency of μ_{max} of 20-30% was greater for HY and SY than PL and ST. Looking back to Fig. 10, two corner rebars in the HY series have largely different μ_{max} , but were under the same loading and exposure conditions. Further, Fig. 11 shows that HY series had larger standard deviation of μ_{max} than ST and SY series. It is therefore inferred that the fibre distribution may be uneven in the HY series, causing locally severe damage during pre-loading and severe pitting corrosion on one of the bars in a beam. The high relative frequency of μ_{max} of 20-30% in SY series is because the total specimen number for SY beams is only three (including one “*uncracked*” beam and two “*unloaded*” beams) and μ_{max} in SY-U0.1 is slightly greater than 20%, as seen from Fig. 10. More specimens need to be studied before conclusions can be drawn regarding the effect of fibres on maximum local corrosion level.

It should be noted that with a defined target crack width, loading condition type and mix proportion, only one beam was studied although there were three rebars were involved in one beam. Replicated specimens under the same condition need to be further studied to verify the tendencies found in this study, as suggested for the recommended practice when reporting corrosion experimental data [33].

4.4. Discussions on the role of longitudinal cracks

4.4.1 Correlation between maximum local corrosion level and longitudinal crack width

Longitudinal crack widths were measured on four cracked ST beams and all the cracked HY and SY beams, see Table 2. Thus, only results from those beams are discussed. The maximum width of each corrosion-induced crack above the same corrosion pit was used. For beams in which longitudinal cracks had been found at the same pit on both the tension surface and side surface (see SY-U0.4 in Fig. 4), the maximum longitudinal crack width was taken. Fig. 13 presents the correlation between longitudinal crack width and maximum local corrosion level of the corrosion pit beneath the crack. Whenever no corrosion-induced cracks were formed, the longitudinal crack width was taken as zero.

Fig. 13 shows that, apart from four of them, most points with non-zero longitudinal cracks lie around a trend line. Although the cracking resistance parameters (the tensile strength f_{ct} and fracture behaviour) of the three types of FRC are different (given in [19]), their data points are still close to the same fitting line. It is also found that some pits with a high maximum local corrosion level of 10-35% did not induce longitudinal cracks. Those points are mainly from middle bars or have Type 6 pits. For the middle bar in a beam, the corrosion-induced cracks are more prone to develop towards the neighbouring bars rather than propagating to the cover surface. This is due to the confinement provided by the surrounding concrete, as revealed in [34]. The dependence of cracking behaviour on local corrosion length and pitting corrosion pattern has been studied numerically in [35], showing the tendency for shorter corrosion lengths to cause shorter and smaller corrosion cracks. Another study [36] showed experimentally that the required rust thickness of localised corrosion for cover cracking increased as the anodic length decreased. For deep but short elliptical pits, the internal pressure arising from the limited volume of corrosion products may not be sufficient to damage the concrete cover. The first example in Fig. 5 illustrates such a case. The maximum local corrosion level was 18.6% while the longitudinal crack width was only 0.02 mm. An important implication is that a rebar may lose a large amount of cross-sectional area in a localised pit, but no large corrosion cracks are produced which might give a warning. This is of major importance for structural condition assessment.

4.4.2 Correlation between pit volume and longitudinal crack width

There is an interaction between longitudinal cracks and pit volume. On the one hand, longitudinal cracks are caused by the volume accumulation of corrosion products. On the other, as longitudinal cracks grow, more steel surface is exposed to chloride and starts to corrode; this increases the rebar volume loss. Fig. 14 shows the correlation between pit volume and longitudinal crack width, with the symbol colour representing the pit type. As can be seen, the correlation depends on the bar location (such as corner or middle bar) and pit type. For a similar pit volume, a larger longitudinal crack was induced by the corner rebar than the middle rebar. Most pits under longitudinal cracks are Types 3, 4 and 5, which have long pits.

The correlation between maximum local corrosion level and pit volume is examined in Fig. 15. In general, the pits under longitudinal cracks have greater volume loss than those without longitudinal cracks. This may be explained by the larger surface area of steel that is exposed to the external environment when there is a longitudinal crack as opposed to a transverse crack. However, the correlation between the pit volume and maximum local corrosion level looks scattered. The maximum local corrosion level can vary a lot for the same pit volume. For a Type 6 pit, the pit volume is smaller than in Types 4 and 5 with similar maximum local corrosion levels. Therefore, the correlation between pit volume and maximum local corrosion level depends greatly on the pit morphology. This indicates that the maximum local corrosion level cannot be solely derived from total steel loss (or pit volume).

4.4.3 Hypothesis of the time-varying influence of cracks on the evolution of pit morphology

Inspired by the above discussions, a time-varying scenario for the corrosion propagation in cracked concrete will now be outlined, as shown in Fig. 16. Before corrosion initiation, transverse cracks existing in concrete provide preferential paths for chloride, oxygen and moisture and lead to localised pitting corrosion near the cracks. This corresponds to Stage I in Fig. 16. The long length of the blue arrow above the transverse cracks shows that the permeability and diffusivity are greater there than in the uncracked region. Microcell inside the pit and macrocell outside it on the uncorroded steel determine the local corrosion rate in the pit. The macrocell corrosion rate may be influenced by several factors such as the concrete resistivity and porosity (both related to the binder type), the cover depth, etc.. Most important factors depend on whether the rate-limiting factor of the corrosion reaction is controlled by the ohmic process or cathodic process [23].

In Stage II, the expansion pressure generated by the pitting corrosion products induces cover cracking. The longitudinal cracks, in turn, impact the pitting corrosion by providing new preferential paths for chloride, oxygen and moisture in this stage. Few studies have been conducted on the influence of longitudinal cracks on the corrosion rate, contrary to a lot of studies on the influence of transverse cracks. In a previous study [21], greater corrosion rate has been reported in concrete with longitudinal cracks than in concrete with transverse cracks. However, it should be noted that the local corrosion rate may be underestimated if the whole exposed steel surface is used instead of the real anodic area to calculate the corrosion rate [21,22], as the corrosion is usually localised at the tip of transverse cracks. In addition, Poursaeed and Hansson [21] found that in the presence of longitudinal cracks, the resistivity of different types of binder was not an influential factor in the corrosion rate of rebars. Since the influence of various factors, such as the chloride concentration, oxygen concentration and concrete resistivity, on the corrosion reactions is complex, it is challenging to quantify the influence of transverse and longitudinal cracks on the corrosion propagation rate.

In Stage III, the longitudinal cracks develop further. The anodic area thereby increases which, in turn, causes the longitudinal cracks to develop further in width and length. The specimens in the present study were between Stages II and III. The mutual interaction between pit development and corrosion-induced cracking will continue with time. Possibly, if there are longitudinal cracks caused by other pits along the beam length, these will interconnect during crack propagation. Eventually, the longitudinal cracks will extend along the whole beam and corrosion pitting will distribute along the whole reinforcement, indicating Stage IV. It is also possible that after long-term exposure to chloride, the chloride content entering through the uncracked cover may be enough to activate a major range of corrosion spots.

A previous study [24] examined the edge beams of a girder bridge (the Stallbacka Bridge in Sweden). Having been exposed to natural corrosion for 32 years, the corroded bars in places with splitting cracks or cover spalling showed corrosion across significant lengths of the bars. This gives a practical example of the corrosion and cracking state in Stage IV. A previous study in [10] has provided experimental evidence for the evolution of the crack and corrosion pattern from Stages III to IV, by analysing two beams that had been subjected to sustained load in a chloride environment for 14 and 23 years, respectively. The steel cross-sectional loss in the beam exposed for 14 years was concentrated in only the middle part along the length of reinforcements. However, the cross-sectional loss along the reinforcements in the beam exposed for 23 years was major over the entire bar length, except the end region. From the cracking maps of one beam drawn at the 14th, 19th and 23rd year, the extent of longitudinal cracks on the beam was seen to increase with years of exposure. Another study in [37] examined the corrosion characteristics of a four-year, naturally corroded concrete beam which was loaded to have the maximum transverse crack width of 0.2 mm before exposed to chloride. This beam presented longitudinal cracks along its entire length and major cross-sectional loss along the whole length of the reinforcement except the end. This corresponds to Stage IV in Fig. 16. The extent of corrosion-induced cracking and corrosion level of rebars in their specimen was much greater than that in this study although the exposure time was close to the one in this study. This is probably due to the thin concrete cover and corrosion of stirrups, as indicated by the authors.

4.4.4 Implications for the long-term durability of FRC structures

Compared to plain reinforced concrete, fibre-reinforced concrete has improved cracking resistance to mechanical loading and corrosion expansion. To evaluate the durability of FRC structures in a chloride environment, the influences of various types of cracks on the steel corrosion process should be considered.

Adding fibres are beneficial to form more tortuous internal cracking and reduce concrete-steel interfacial damage under service loading. A recent study (reported in [20]) revealed that interfacial damage may increase corrosion activity (in terms of the total rebar mass loss and corrosion length). This was done by comparing specimens with both transverse cracks and interfacial damage to those with transverse cracks only. However, the maximum local corrosion level of their specimens was not reported and the corrosion time investigated was less than a year. The influence of interfacial damage has been discussed in section 4.3.1 of the present study, by comparing the maximum local corrosion level of bars in beams under the “*unloaded*” and “*loaded*” conditions. This was because the interfacial damage was postulated as being less for the “*unloaded*” condition than for the “*loaded*” one. The results showed that, in most cases, the maximum local corrosion level of bars in beams with the “*unloaded*” condition was greater than for the “*loaded*” condition. Further studies are needed to confirm the effect of interfacial damage on corrosion propagation.

Moreover, FRC may delay cover cracking under corrosion expansion due to the additional confinement provided by fibres [38,39]. Undoubtedly, longitudinal cracks may greatly aggravate the total steel loss (as in pit volume) by increasing the anodic length. Even so, the maximum cross-sectional loss may develop more slowly when the corrosion length is increased. The correlation between maximum local corrosion level and pit volume was found to depend on the pit morphology. As the way in which pit morphology influences structural behaviour is still unresolved, the benefits afforded by concrete structures reinforced with steel bars and fibres (as compared to conventional reinforced concrete) remain to be quantified. Further theoretical studies covering the local corrosion rate prediction from electrochemical reaction and transport process in cracked concrete, as well as experimental work on specimens exposed for longer periods, are needed to assess the overall performance of FRC in a chloride environment.

5. Conclusions

This paper studied the corrosion pattern and characteristics of rebars in un- and pre-cracked plain and fibre-reinforced concrete which were subjected to natural corrosion for more than three years. A 3D-scanning technique was used to characterise the pit morphology. The influence of loading type, fibres, flexural cracks and corrosion-induced cracks on the maximum local corrosion level and pit morphology was studied. The following conclusions were drawn:

(1) The pre-cracked beams showed various degrees of pitting corrosion, with the maximum local corrosion level in almost all bars significantly greater than for bars in uncracked beams. Still, no correlation was found between the maximum flexural crack width (nominally 0.1 and 0.4 mm) and the maximum local corrosion level. However, one of the beams was occasionally pre-cracked to 0.8 mm. The three bars in this beam had the highest maximum local corrosion level of all bars: greater than 20%.

(2) All the beams in the steel fibre series had lower average maximum local corrosion levels than the counterparts of plain series. Hybrid fibre series and synthetic fibre series showed similar or lower average maximum local corrosion levels than their plain series counterparts for the larger crack width (0.4 mm). The bars in the hybrid fibre series showed a large standard deviation, which may have been due to uneven fibre distribution.

(3) In three out of four comparison groups, the bars had a higher average maximum local corrosion level in the “*unloaded*” condition than in the “*loaded*” one. **This contradicts earlier findings.** A possible explanation is that the greater interfacial damage in the “*loaded*” condition induced a longer anodic site and slower growth of the pit depth than in the “*unloaded*” condition. Further studies are required to understand the influence of interface damage on the corrosion propagation.

(4) When present, the maximum longitudinal crack width had a linear correlation to the maximum local corrosion level for most pits. However, some severe pits did not induce any longitudinal crack, or the induced corrosion crack was very small. It is important to note that pitting corrosion did not always induce longitudinal cracks; in practice, the maximum local corrosion level in pitting corrosion may be underestimated if it is assessed on the basis of longitudinal crack width.

(5) A hypothesis about the time-dependent interplay between transverse and longitudinal cracks and corrosion development was formulated as follows. Transverse cracks generated before the corrosion onset lead to localised pitting corrosion close to the cracks. When corrosion-induced cracks appear, the pitting length increases and total mass loss greatly increases. However, the maximum cross-sectional area loss has no unique correlation with the total mass loss in the pit.

Acknowledgements

The work reported in this paper has been supported by: the Swedish Transport Administration, under the project grant TRV 2018/36506; the construction industry's organisation for research and development (SBUF) under the project grant 13683; Chalmers University of Technology; Thomas Concrete Group; and Cementa AB (Heidelberg Cement Group).

Compliance with ethical standards

Conflict of interest

The authors declare that they have no conflict of interest.

References

1. Tang SW, Yao Y, Andrade C, Li Z (2015) Recent durability studies on concrete structure. *Cement and Concrete Research* 78:143-154
2. Bentur A, Berke N, Diamond S (1997) *Steel Corrosion in Concrete: Fundamentals and Civil Engineering Practice*. CRC Press,
3. Wang K, Jansen DC, Shah SP, Karr AF (1997) Permeability study of cracked concrete. *Cement and Concrete Research* 27 (3):381-393
4. Rodriguez OG, Hooton RD (2003) Influence of cracks on chloride ingress into concrete. *ACI Materials Journal* 100 (2):120-126
5. Schießl P, Raupach M (1997) Laboratory studies and calculations on the influence of crack width on chloride-induced corrosion of steel in concrete. *ACI Materials Journal* 94 (1):56-61
6. Otieno M, Alexander M, Beushausen H-D (2010) Corrosion in cracked and uncracked concrete— influence of crack width, concrete quality and crack reopening. *Magazine of Concrete Research* 62 (6):393-404
7. Boschmann Käthler C, Angst UM, Wagner M, Larsen CK, Elsener B (2017) Effect of cracks on chloride-induced corrosion of steel in concrete—a review: *Etatsprogrammet Varige konstruksjoner 2012-2015*. ETH Zurich,
8. Scott A, Alexander M (2007) The influence of binder type, cracking and cover on corrosion rates of steel in chloride-contaminated concrete. *Magazine of Concrete Research* 59 (7):495-505
9. Otieno M, Beushausen H, Alexander M (2016) Resistivity-based chloride-induced corrosion rate prediction models and hypothetical framework for interpretation of resistivity measurements in cracked RC structures. *Materials and Structures* 49 (6):2349-2366
10. Zhang R, Castel A, François R (2009) The corrosion pattern of reinforcement and its influence on serviceability of reinforced concrete members in chloride environment. *Cement and Concrete Research* 39 (11):1077-1086
11. Francois R, Khan I, Vu NA, Mercado H, Castel A (2012) Study of the impact of localised cracks on the corrosion mechanism. *European Journal of Environmental Civil Engineering* 16 (3-4):392-401
12. FIB (2006) *Model code for service life design*. vol 34. Fédération Internationale du Béton,
13. Eurocode 2: *Design of concrete structures—Part 1-1: general rules and rules for buildings: EN 1992-1-1 (2004)*. European Committee for Standardization,
14. Stang H, Aarre T (1992) Evaluation of crack width in FRC with conventional reinforcement. *Cement Concrete Composites* 14 (2)
15. Jansson A, Flansbjerg M, Löfgren I, Lundgren K, Gylltoft K (2012) Experimental investigation of surface crack initiation, propagation and tension stiffening in self-compacting steel–fibre-reinforced concrete. *Materials and Structures* 45 (8):1127-1143
16. Mihashi H, Ahmed SFU, Kobayakawa A (2011) Corrosion of reinforcing steel in fiber reinforced cementitious composites. *Journal of Advanced Concrete Technology* 9 (2):159-167
17. Blunt J, Jen G, Ostertag C (2015) Enhancing corrosion resistance of reinforced concrete structures with hybrid fiber reinforced concrete. *Corrosion Science* 92:182-191

18. Berrocal CG, Löfgren I, Lundgren K, Tang L (2015) Corrosion initiation in cracked fibre reinforced concrete: influence of crack width, fibre type and loading conditions. *Corrosion Science* 98:128-139
19. Berrocal CG, Löfgren I, Lundgren K (2018) The effect of fibres on steel bar corrosion and flexural behaviour of corroded RC beams. *Engineering Structures* 163:409-425
20. Hay R, Ostertag CP (2019) Influence of transverse cracks and interfacial damage on corrosion of steel in concrete with and without fiber hybridization. *Corrosion Science*
21. Poursaee A, Hansson CM (2008) The influence of longitudinal cracks on the corrosion protection afforded reinforcing steel in high performance concrete. *Cement and Concrete Research* 38 (8-9):1098-1105
22. Marcotte T, Hansson C (2003) The influence of silica fume on the corrosion resistance of steel in high performance concrete exposed to simulated sea water. *Journal of Materials Science* 38 (23):4765-4776
23. Hornbostel K, Elsener B, Angst UM, Larsen CK, Geiker MR (2017) Limitations of the use of concrete bulk resistivity as an indicator for the rate of chloride - induced macro - cell corrosion. *Structural Concrete* 18 (2):326-333
24. Tahershamsi M, Fernandez I, Lundgren K, Zandi K (2017) Investigating correlations between crack width, corrosion level and anchorage capacity. *Structure and Infrastructure Engineering* 13 (10):1294-1307
25. Bhandari J, Khan F, Abbassi R, Garaniya V, Ojeda R (2015) Modelling of pitting corrosion in marine and offshore steel structures—A technical review. *Journal of Loss Prevention in the Process Industries* 37:39-62
26. Suzuki K, Ohno Y, Praparntanatorn S, Tamura H Mechanism of steel corrosion in cracked concrete. In: *The Third International Symposium On Corrosion Of Reinforcement In Concrete Construction*, Warwickshire, 1990.
27. Marcos-Meson V, Michel A, Solgaard A, Fischer G, Edvardsen C, Skovhus TL (2018) Corrosion resistance of steel fibre reinforced concrete—A literature review. *Cement and Concrete Research* 103:1-20
28. Arya C, Ofori-Darko F (1996) Influence of crack frequency on reinforcement corrosion in concrete. *Cement and Concrete Research* 26 (3):345-353
29. François R, Laurens S, Deby F (2018) *Corrosion and Its Consequences for Reinforced Concrete Structures*. Elsevier,
30. Rodriguez J Corrosion of reinforcement and service life of concrete structures. In: *Proceedings of 7th International Conference on DBMC, 1996*. pp 117-126
31. Vidal T, Castel A, Francois R (2004) Analyzing crack width to predict corrosion in reinforced concrete. *Cement and Concrete Research* 34 (1):165-174
32. Gonzalez J, Andrade C, Alonso C, Feliu S (1995) Comparison of rates of general corrosion and maximum pitting penetration on concrete embedded steel reinforcement. *Cement and Concrete Research* 25 (2):257-264
33. Isgor OB, Angst U, Geiker M, Halmen C, Hansson C, Pacheco J, Tepke D, Trejo D, Vaddey P (2019) Recommended practice for reporting experimental data produced from studies on corrosion of steel in cementitious systems. *RILEM Technical Letters* 4:22-32
34. Chen E, Leung CK (2015) Finite element modeling of concrete cover cracking due to non-uniform steel corrosion. *Engineering Fracture Mechanics* 134:61-78
35. Tran K, Nakamura H, Kunieda M, Ueda N (2011) Three dimensional behaviour of concrete cracking due to rebar corrosion. *Procedia Engineering* 14:419-426
36. Torres-Acosta AA, Sagues AA (2004) Concrete cracking by localized steel corrosion—Geometric effects. *ACI Materials Journal* 101 (6):501-507
37. Fu C, Jin N, Ye H, Jin X, Dai W (2017) Corrosion characteristics of a 4-year naturally corroded reinforced concrete beam with load-induced transverse cracks. *Corrosion Science* 117:11-23
38. Solgaard AOS, Michel A, Geiker M, Stang H (2013) Concrete cover cracking due to uniform reinforcement corrosion. *Materials and Structures* 46 (11):1781-1799
39. Berrocal CG, Fernandez I, Lundgren K, Löfgren I (2017) Corrosion-induced cracking and bond behaviour of corroded reinforcement bars in SFRC. *Composites Part B: Engineering* 113:123-137

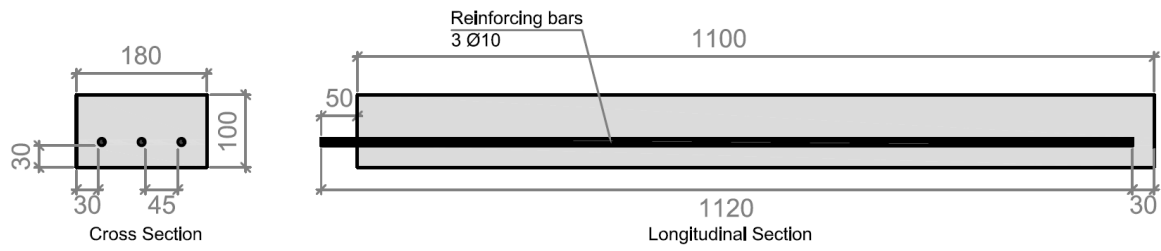


Fig. 1. Specimen geometry.

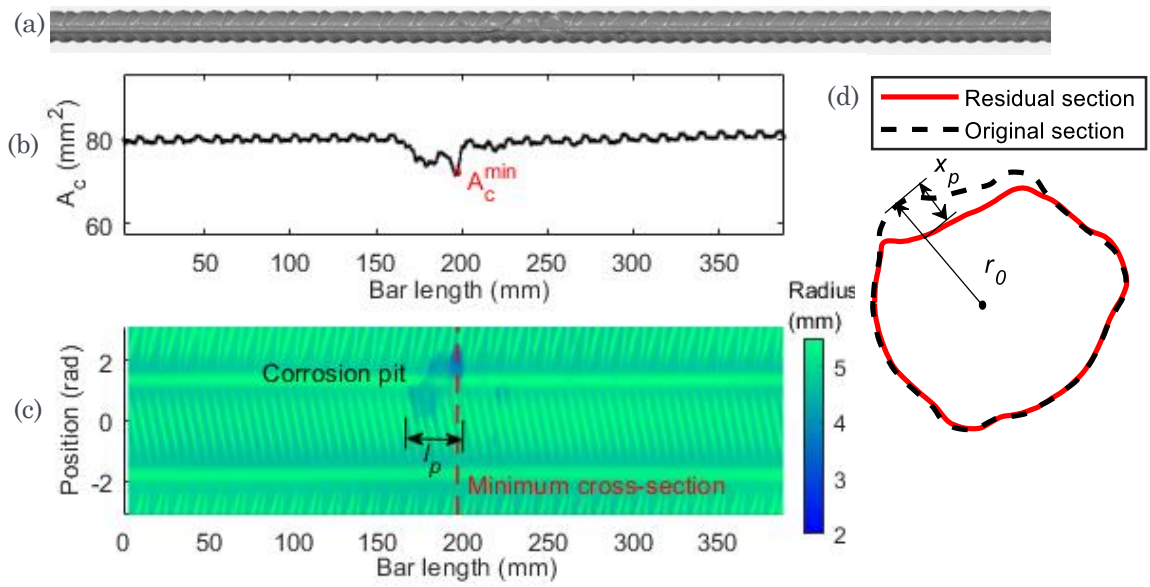


Fig. 2. Example illustrating corrosion evaluation from 3D-scanning: (a) 3D surface mesh in GOM Inspect; (b) longitudinal variation of the cross-sectional area along the scanned length; (c) 2D plot of the bar surface with colour scale showing the magnitude of radius; (d) residual and original cross-sectional appearance at the minimum cross-section.

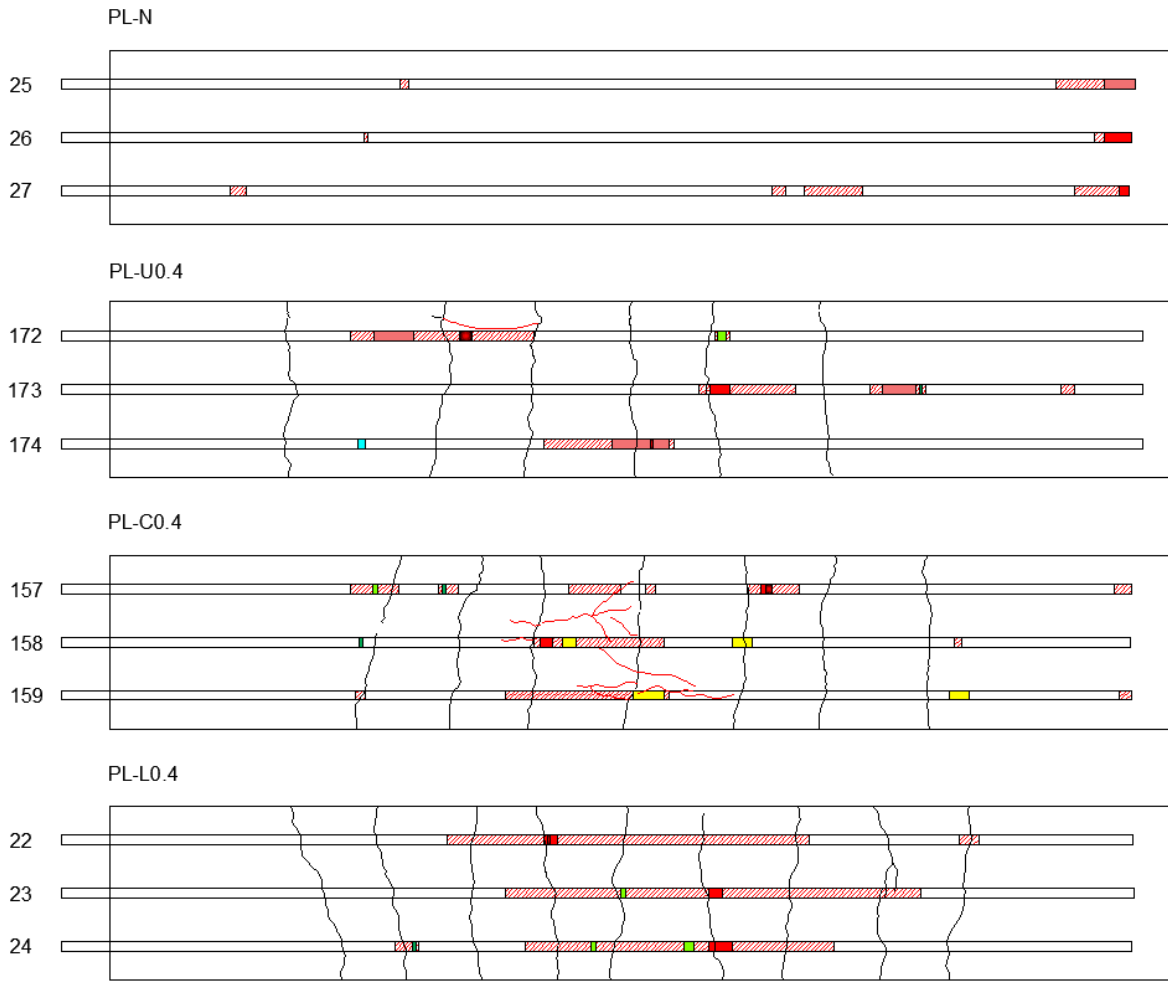


Fig. 3. Crack-corrosion pattern for PL series under the “uncracked”, “unloaded”, “cyclic” and “loaded” conditions, with 0.4 mm target crack width. (Shading represents general corrosion, while solid colours represent pitting corrosion with the colour corresponding to the pit types defined in Table 3. Flexural and corrosion cracks are indicated by black and red lines respectively).

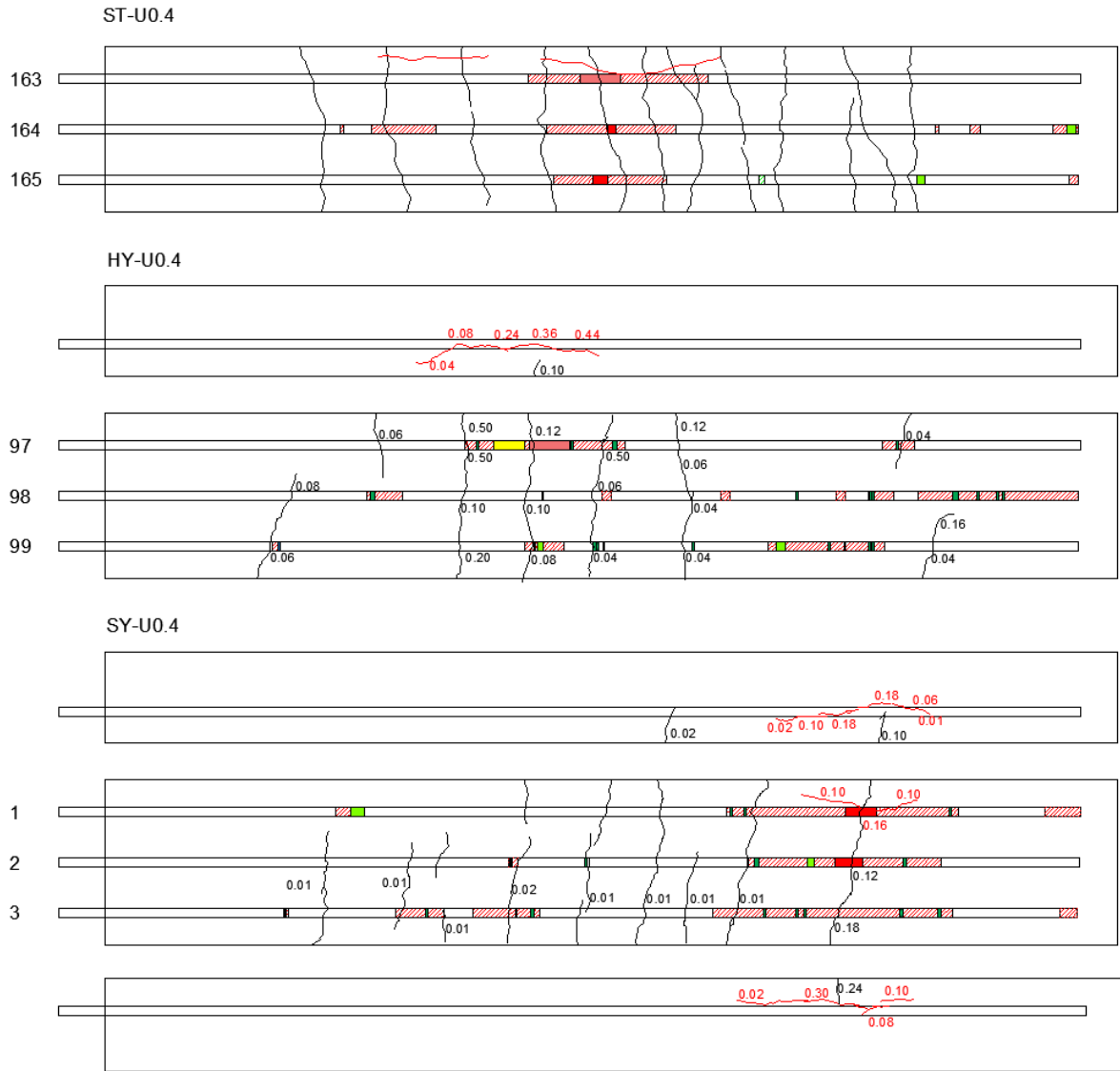


Fig. 4. Crack-corrosion pattern for ST series, HY series and SY series under the “unloaded” condition, with 0.4 mm target crack width.

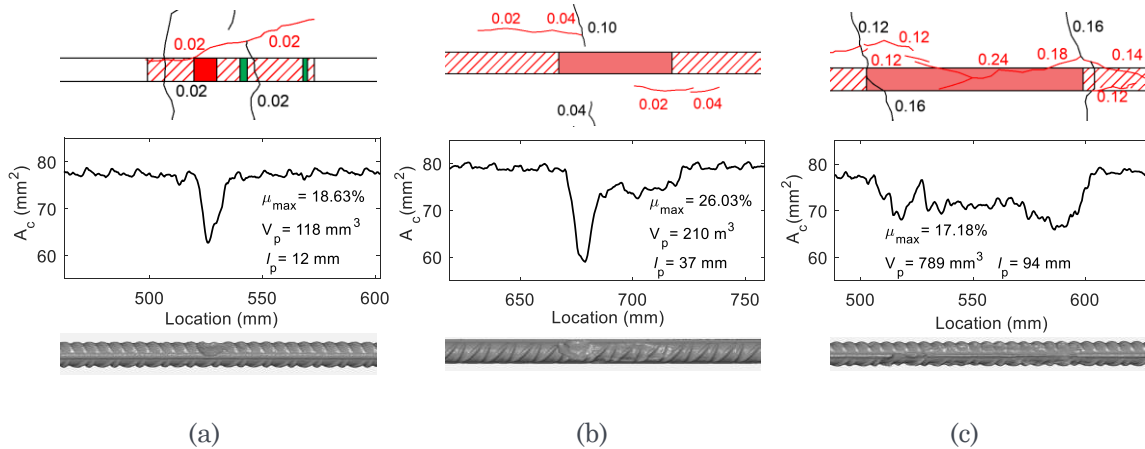


Fig. 5. Mapping cracks and longitudinal variation of the cross-sectional area: (a) one rebar in HY-C0.4; (b) one rebar in HY-C0.1; (c) one rebar in ST-L0.1. (Note: the horizontal axis “location” is the distance of cross-sections on the rebar from the bar’s end outside the concrete).

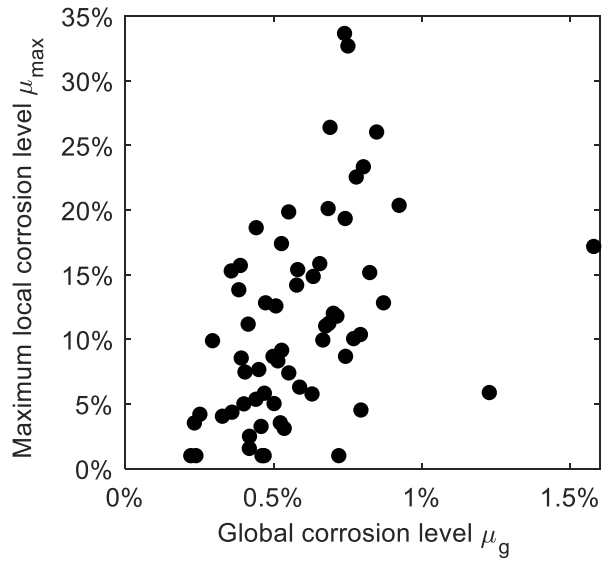


Fig. 6. Maximum local corrosion level versus global corrosion level.

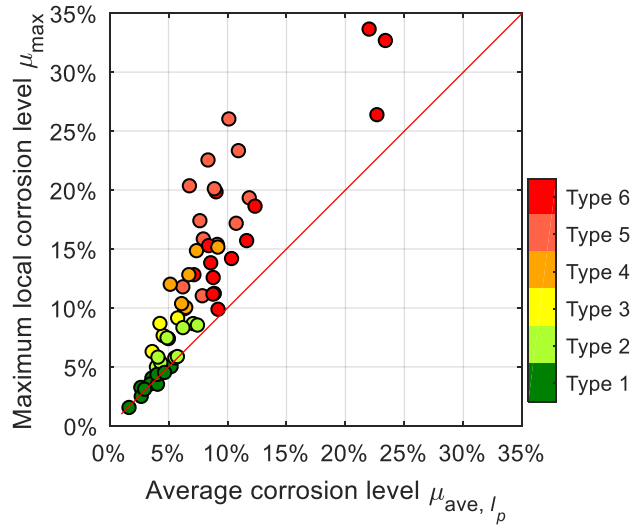


Fig. 7. Maximum local corrosion level versus average corrosion level in the pit.

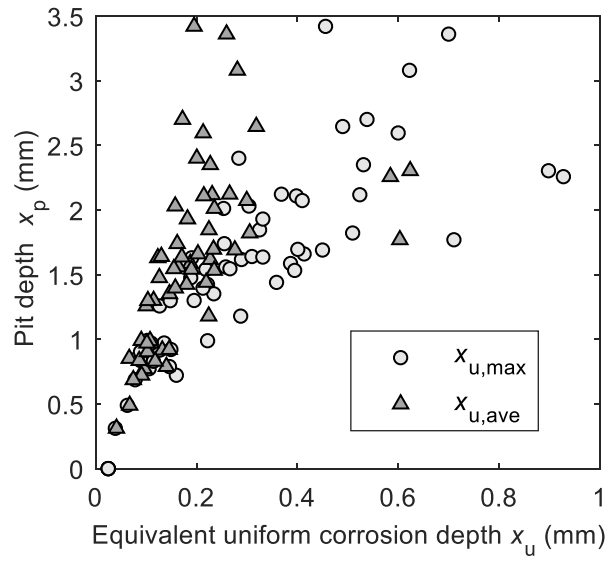


Fig. 8. Pit depth versus equivalent uniform corrosion depth.

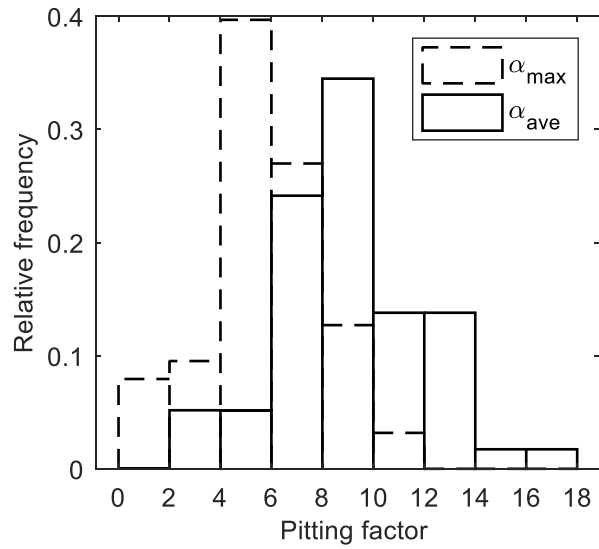


Fig. 9. Histograms of the pitting factor.

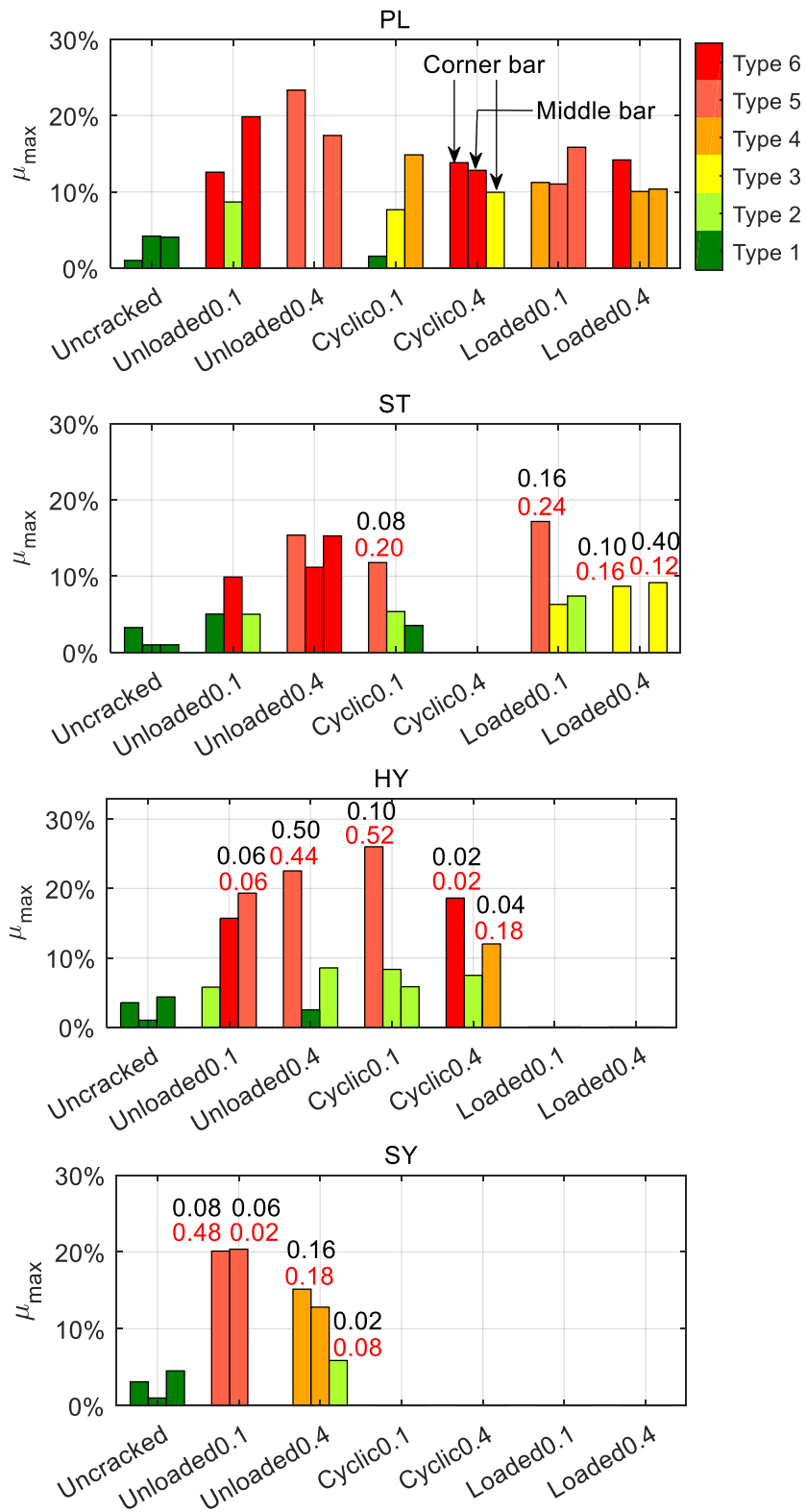


Fig. 10. Maximum local corrosion levels for all bars.

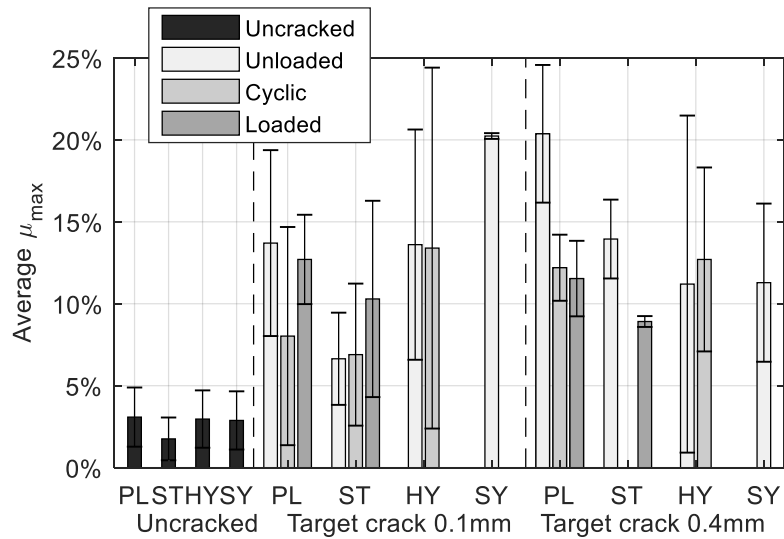


Fig. 11. Mean values and standard deviations of maximum local corrosion level of bars in the same beam.

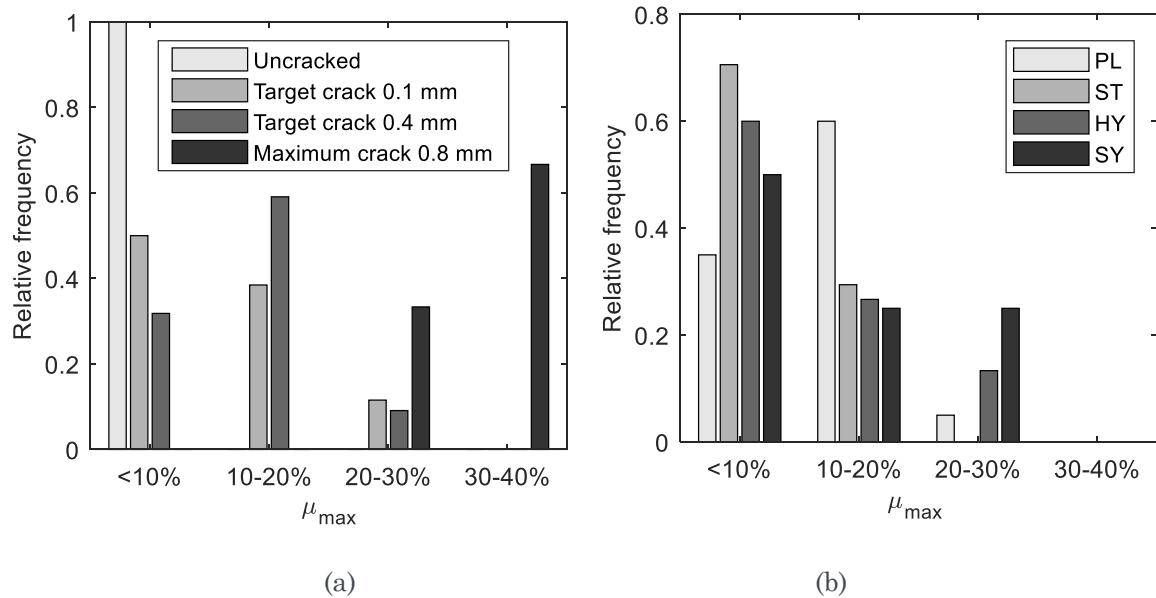


Fig. 12. Histograms of maximum local corrosion level: (a) under different maximum crack widths; (b) for different mixes.

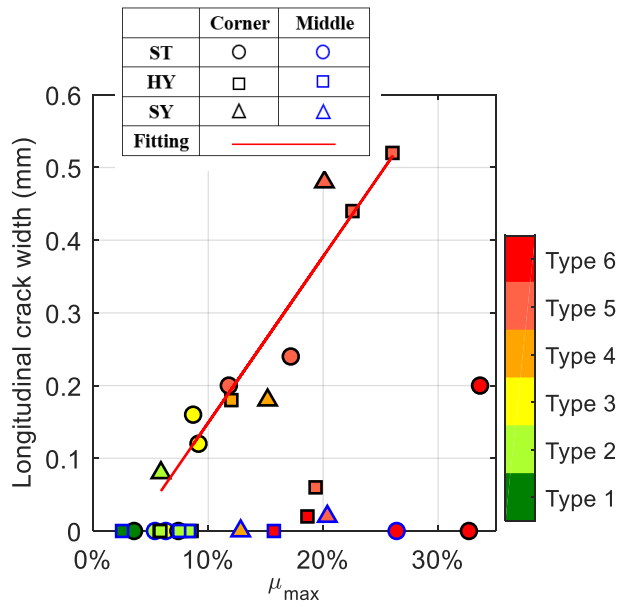


Fig. 13. Longitudinal crack width versus maximum local corrosion level.

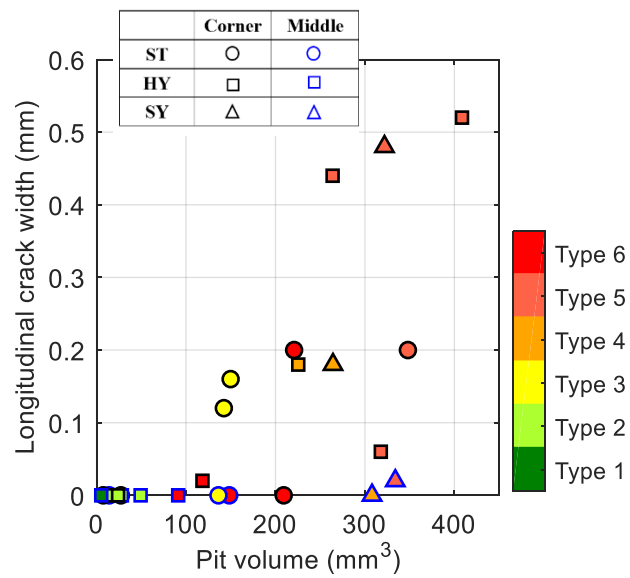


Fig. 14. Longitudinal crack width versus pit volume.

	Corner	Middle
With longitudinal cracks	★	★
Without longitudinal cracks	◇	◇

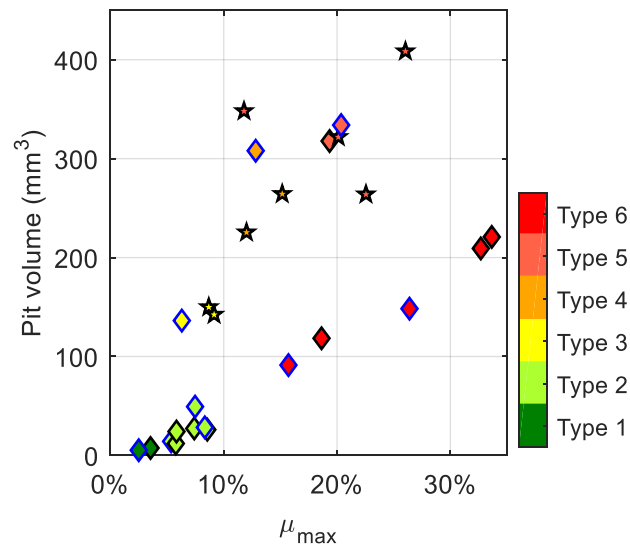


Fig. 15. Pit volume versus maximum local corrosion level.

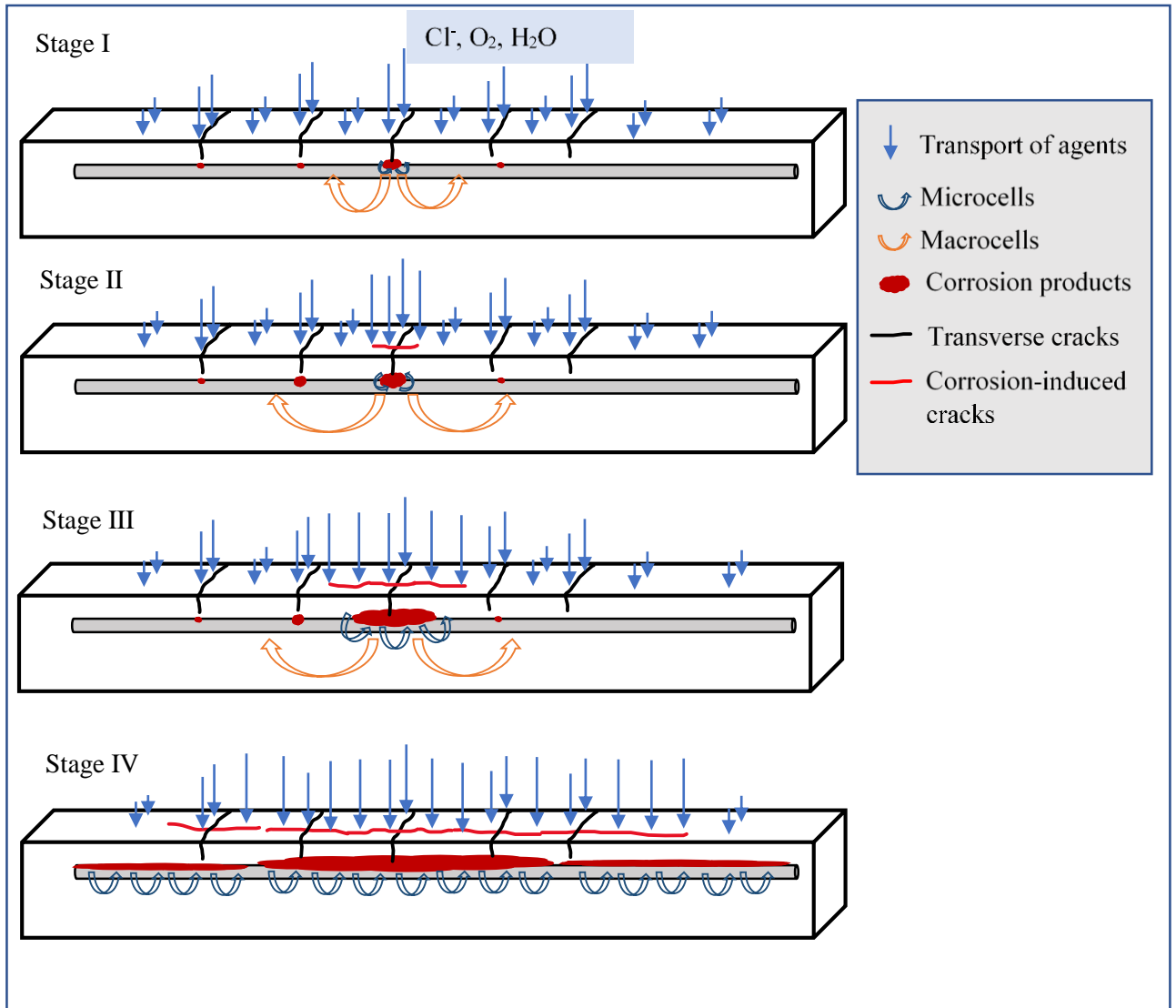


Fig. 16. Hypothesis for the interplay between transverse and longitudinal cracks and corrosion. Stage I: transverse cracks induce localised pitting corrosion. Stage II: longitudinal cracks start to form. Stage III: longitudinal cracks develop and corrosion length increases. Stage IV: longitudinal cracks spread along the whole beam length and corrosion becomes more general.

Table 1. Concrete mix proportions, in [kg/m³]

Component				
Cement (CEM I 42.5N SR 3 MH/LA)				360
Limestone filler (Limus 40)				165
Fine aggregate (sand 0/4)				770
Coarse aggregate (crushed 5/16)				833
Effective water				169
Superplasticizer – Glenium 51/18				5.76
Air entrainer – MicroAir 105				0.72
Fibre content (vol. %)	PC	ST	HY	SY
Steel – Dramix® 65/35-BN	-	0.5	0.35	-
PVA – Kuralon™ RFS400	-	-	0.15	-
PVA – Kuralon™ RF4000	-	-	-	0.75

Table 2. Summary of specimens' conditions.

Load conditions		Series	Target crack widths (mm)		No. of beams	Pre-loading time	Exposure period	Storing period before testing	Crack documentation before testing	
Uncracked		PL	-		1	10-week age	3 years	18 months	only crack pattern on tension surface	
		ST	-		1			24 months	all crack pattern and crack width	
		HY	-		1			24 months	all crack pattern and crack width	
		SY	-		1			24 months	all crack pattern and crack width	
Cracked	Unloaded	1 cycle	PL	0.1	0.4			2	18 months	only crack pattern on tension surface
			ST	0.1	0.4			2	18 months	only crack pattern on tension surface
			HY	0.1	0.4			2	24 months	all crack pattern and crack width
			SY	0.1	0.4			2	24 months	all crack pattern and crack width
		5 cycles	PL	0.1	0.4			2	18 months	only crack pattern on tension surface
			ST	0.1	0.4 (0.8)			2	24 months	all crack pattern and crack width
			HY	0.1	0.4			2	24 months	all crack pattern and crack width
	Loaded	PL	0.1	0.4	2	18 months	only crack pattern on tension surface			
		ST	0.1	0.4	2	24 months	all crack pattern and crack width			









Note: specimens tested after 18-month and 24-month storage in the laboratory following the exposure period are differentiated by  and .

Table 3. Pit morphology classification.

Light	Moderate		Severe		
$\mu_{max} \leq 5\%$	$5\% < \mu_{max} \leq 10\%$		$\mu_{max} > 10\%$		
$x_p < r_0/5$	$x_p < r_0/3$		$x_p < r_0/3$	$x_p > r_0/3$	
$l_p < d_0/2$	$l_p < d_0$	$l_p > 2.5d_0$	$l_p > 2.5d_0$	$l_p > 2.5d_0$	$l_p < 2.5d_0$
Type 1	Type 2	Type 3	Type 4	Type 5	Type 6
Tiny pit 	Small elliptical pit 	Long pitting range with shallow pit depth 	Long pit with shallow pit depth 	Long pit with locally deep pit depth 	Elliptical pit with deep pit depth 

Note: r_0 and d_0 are the nominal radius and diameter of rebar.

Nomenclature

A_0^{min}	uncorroded cross-sectional area at the minimum cross-section
A_c^{min}	remaining cross-sectional area at the minimum cross-section
A_c	remaining area at each cross-section
V_p	pit volume
d_0	nominal diameter of steel reinforcement
k	coefficient taking into account the removal of mill-scale during sand-blasting
l_p	pit length
m_0	initial weight of reinforcement before casting
m_f	final weight of reinforcement after corrosion
r_0	nominal radius of steel reinforcement
x_p	pit depth
x_u	equivalent uniform corrosion depth
$x_{u,ave}$	equivalent uniform corrosion depth for the corrosion level μ_{ave,l_p}
$x_{u,max}$	equivalent uniform corrosion depth for the corrosion level μ_{max}
α_{ave}	pitting factor calculated from $x_{u,ave}$
α_{max}	pitting factor calculated from $x_{u,max}$
μ_{ave,l_p}	average corrosion level within the pit length
μ_{max}	maximum local corrosion level, defined as the maximum cross-sectional area loss percentage
μ_g	global corrosion level of the whole bar, measured from weight loss
PL:	plain reinforced concrete, i.e. conventional reinforced concrete
ST:	concrete reinforced with conventional steel bars and steel fibres
HY:	concrete reinforced with conventional steel bars and hybrid fibres (steel fibres and synthetic fibres)
SY:	concrete reinforced with conventional steel bars and synthetic fibres

Appendix

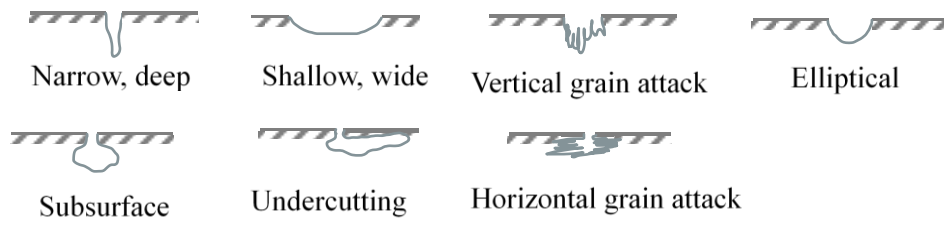


Fig. 17. Sketch of common pit shapes; redrawn from [25].

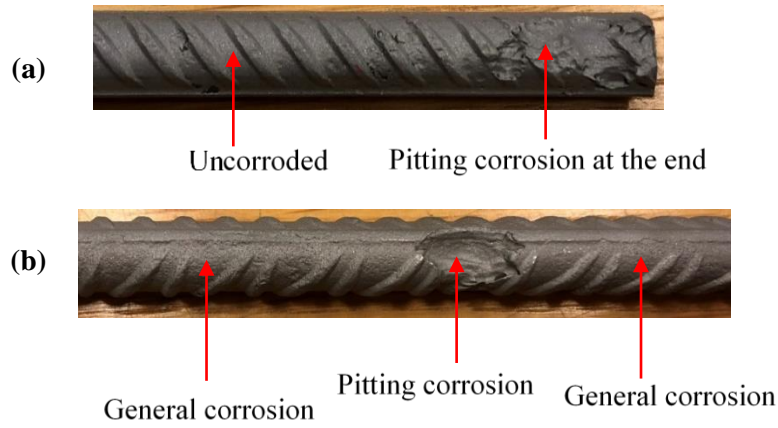


Fig. 18. Corrosion pictures: (a) pitting at the end; (b) general corrosion and pitting corrosion.

Chen E., Berrocal, C. G., Fernandez I., Löfgren I., & Lundgren K. (2020): Assessment of the mechanical behaviour of reinforcement bars with localised pitting corrosion by Digital Image Correlation. *Engineering Structures* 219(2020).

ASSESSMENT OF THE MECHANICAL BEHAVIOUR OF REINFORCEMENT BARS WITH LOCALISED PITTING CORROSION BY DIGITAL IMAGE CORRELATION

E Chen¹, Carlos G. Berrocal^{1,2}, Ignasi Fernandez¹, Ingemar Löfgren^{1,2}, Karin Lundgren¹

¹Chalmers University of Technology, Division of Structural Engineering, Göteborg, SE-41296, Sweden

²Thomas Concrete Group AB, Södra Vägen 28, Göteborg, 41254, Sweden

ABSTRACT

Corrosion of reinforcement in concrete impairs the mechanical behaviour of rebars by decreasing their strength and deformation capacity. In this study, uniaxial tensile tests were carried out on 61 rebars taken from 22 pre- and un-cracked reinforced concrete beams subjected to drying and wetting cycles in chloride solution for over three years. A 3D-scanning technique was used to characterise the maximum local corrosion level, μ_{max} , and different pit shape parameters. Digital Image Correlation (DIC) was used to capture the displacement field of the test bars; the engineering strain was measured through the virtual extensometers created in the DIC post-processing software. The proof and ultimate forces showed linear decreasing trends of μ_{max} , while the proof and ultimate strengths (based on the minimum residual cross-sectional area) were not obviously affected by corrosion. The ultimate strain of corroded bars depended on the gauge length due to strain localisation in the pit. Thus, it was emphasised that the ultimate strain may be overestimated if measured based on a short gauge across the pit. It was also observed that when μ_{max} exceeded a critical local corrosion level (μ_{crit} depending on the ratio between the yield and ultimate strengths of the steel), the region outside the pit did not develop yielding. A lower bound of ultimate strain was further derived as a function of the mechanical parameters of uncorroded steel and maximum local corrosion level. This provided a good comparison with the experimental results. Ultimately, a hypothesis for time-dependent assessment of strain capacity is proposed, considering the evolution of corrosion morphology over time.

Keywords: pitting corrosion; mechanical properties; strain measurement; 3D-scanning; Digital Image Correlation

Highlights:

- Strength (based on minimum residual area of corroded bars) was almost constant.
- Steel outside the pit did not yield when critical corrosion level was exceeded.
- Analytical lower-bound model was given for ultimate strain.
- Semi-analytical model was developed to calculate ultimate strain at any gauge length.
- Ultimate strain depends on corrosion level, pit morphology and gauge length.

Introduction

Corrosion of steel in concrete is a major cause of impaired safety and durability of infrastructure. As existing structures deteriorate over time due to corrosion, assessing the residual performance of concrete structures accurately becomes imperative, if engineers are to carry out safe, economical maintenance and rehabilitation operations. Corrosion damage in reinforced concrete mainly includes cover cracking, bond degradation of the steel-concrete interface, and undermining the mechanical behaviour of rebars. None of these three issues has been satisfactorily quantified with respect to the corrosion level, even though they have attracted wide interest in recent decades. This may be due to various difficulties including, but not limited to: i) difficulty of quantifying corrosion level accurately and non-destructively; ii) experimental studies usually use higher corrosion rates due to time limitations, altering the corrosion process compared to what occurs in real structures, thus leading to different corrosion morphologies and behaviour of the corrosion products; and iii) corrosion of steel in concrete involves several coupled multi-physical and mechanical processes, which are complex and the interactions of which are not yet fully understood.

In reinforced concrete elements, reinforcing steel is the main component carrying tensile stress. Understanding the mechanical properties of corroded rebars is essential to the development of reliable assessment models for corroded structures. The effects of corrosion on the mechanical properties of reinforcing bars have primarily been investigated through experimental testing. Empirical relationships which fit the mechanical properties to various corrosion features have been suggested, see [1-14] for example. Although existing research indicates that the load capacity and ductility of steel bars are reduced with increasing corrosion level, the empirical relationships derived for the mechanical parameters (as a function of corrosion level) vary significantly between different studies and, in some cases, even contradict each other. This is most likely attributable to variations in the type of corrosion condition and type of steel, plus the different evaluation methods used in quantifying corrosion levels and mechanical properties, see [1, 2, 4, 6, 11, 14] for example.

The specimens examined in the literature include bare bars and bars extracted from concrete. Bar corrosion was produced using several different methods: applying impressed current [1, 2, 6, 7, 12], exposure to chloride spray in the laboratory [4, 5, 10, 11], simulating corrosion damage with machined defects [1, 2, 11], and natural corrosion in real structures [13, 14]. From previous studies, the reduction in both yielding force and maximum force displayed a linear trend with increasing corrosion level. Moreover, some studies [6, 14] indicated that the decreasing slope is strongly dependent on how the corrosion level is determined: average cross-sectional area loss from the total weight loss or maximum cross-sectional area loss from advanced image techniques such as 3D-scanning. The type of steel may also influence the results, as mentioned in [14]. For steel with heterogeneous microstructure and mechanical properties throughout the bar cross-section, such as TEMPCORE steel [15], the relative contribution of the area loss in each layer to the strength loss may differ.

For the stresses at yielding force and maximum force, when these were calculated as the ratio between the force and the nominal cross-sectional area or average remaining cross-sectional area, a decreasing trend with increasing average corrosion level was observed [1, 5-7, 14]. When the minimum remaining cross-sectional area was used to calculate the stress, it was observed [5, 6, 14] that the stresses at yielding and at maximum force were not significantly affected by corrosion. They even exhibited a slightly increasing trend at higher corrosion levels.

Regarding the deformation and ductility behaviour of corroded rebars, it has been widely reported that, compared to the loss of load capacity, the ultimate strain decreased more markedly

with increasing corrosion levels [2, 4-6, 10, 11, 14]. It should be noted that, in most studies, “ultimate strain” referred to the strain at maximum force, whereas a few used it to mean the strain at failure. Throughout this paper, “ultimate strain” is defined as the strain at maximum force. Many studies [5, 6, 10, 11] have proposed an exponential decaying function for the ultimate strain versus the corrosion level, with different studies suggesting different empirical coefficients. One study [11] demonstrated that different corrosion morphologies led to significantly different decaying factors of the ultimate strain in terms of corrosion level, by comparing three groups of specimens with artificial notches of various shapes. Furthermore, in the tensile test, it is evident that different extensometer gauge lengths have been chosen by different researchers to measure the ultimate strain, such as 50 mm [7, 14], 100 mm [4], 200 mm [1], five times the bar diameter [13], ten times the bar diameter [11], and the total length of tested bars [6]. A previous study [1] speculated that the gauge length may influence the strain results, as the local yielding elongation over the failure zone may be very different compared to the total elongation of corroded rebars. However, to the authors’ knowledge, there have been no prior studies specifically investigating the effect of gauge length on the deformation capacity of corroded rebars.

Most literature studied bars corroded by impressed current [1, 2, 6, 7, 12], which induced corrosion throughout the length of the bar and a mixed morphology of general and pitting corrosion. A few studies investigated bars taken from real structures, which had naturally corroded for decades [13, 14]. They simultaneously exhibited noticeable uniform corrosion and pit attacks, representing the advanced stages of chloride-induced corrosion [14]. The corrosion morphology of isolated localised pits formed under natural corrosion conditions has rarely been studied. However, this type of corrosion is common in practical reinforced concrete structures [16], particularly in the early stages of corrosion, which is caused by pre-existing cracks in concrete. Furthermore, localised pitting is a more dangerous corrosion condition compared to general corrosion and extensive pitting corrosion (in other words, when pitting corrosion spreads over the whole bar surface). This is because there may be a lack of warning, in the form of visible corrosion-induced cover cracking [16].

This study tested corroded bars extracted from pre- and un-cracked reinforced concrete beams which had been subjected to cyclic wet-drying exposure to chloride solution for over three years. The bars showed isolated corrosion pits, with negligible superficial corrosion surrounding the pits. The purpose of this study was to quantify the strength and strain capacity of TEMPCORE steel rebars with localised pitting corrosion as a function of corrosion level. A 3D-scanning technique was used to characterise the pit morphology accurately, while Digital Image Correlation (DIC) was used to measure the deformation of the corroded bars during tensile testing. The local strain distribution and ultimate strain (based on different virtual extensometers created in the DIC post-processing software) were evaluated using a real-time displacement field along the bar and within the measuring volume of the DIC cameras. Based on the DIC findings, an analytical model and a semi-analytical model were proposed to calculate the ultimate strain for any gauge length greater than the pit length. Subsequently, the experimental results of the ultimate strain were compared to other studies investigating bars with different corrosion morphologies and using different strain measurement lengths. Finally, the degradation of strain capacity with corrosion time is discussed, relative to the evolution of corrosion morphology over time.

Experimental description

Specimens

Hot-rolled ribbed TEMPCORE steel reinforcement bars were used in this study. The steel class was normal-ductility B500B, as defined in Appendix C of Eurocode 2 [17]. The bars had a nominal diameter of 10 mm. They were extracted from 22 reinforced concrete beams (1100 x 180 x 100 mm), with 18 beams pre-cracked to a crack width of either 0.1 or 0.4 mm under a three-point bending configuration. The remaining four were uncracked. After the initial pre-cracking, all beams were subjected to cyclic wet-drying exposure to chloride solution (of 16.5% NaCl concentration) for three years and stored in the laboratory for an additional one or two years before the bars were extracted. Further details of the beams' preparation and corrosion environment can be found in [18].

After the rebars were extracted from the beams, they were cleaned by sand-blasting, according to [19]. They were then cut with an electrical rebar cutter to obtain 500 mm segments, with the most severe pitting located near the centre. Where more than two pits of similar severity were found in relatively close proximity, the segment length was extended to 550 mm, to incorporate both pits within the same specimen. A total of 61 bars were tested, including five uncorroded bars.

Corrosion level evaluation with 3D-scanning

Traditionally, the corrosion level is determined by the gravimetric weight loss method. The gravimetric weight loss of all specimens (i.e. cut bar segments) in this study was found to be less than 3.5%. However, this method is not considered appropriate for evaluating pitting corrosion, as the weight loss in the pit was very small compared to the weight of the whole bar. Instead, the local corrosion level was evaluated by 3D-scanning of the steel bar surface. A portable laser scanner (Handy Scan 700TM from Creaform) was used, with an accuracy of up to 20 μm and a maximum spatial resolution of 0.05 mm in the resulting point cloud. Based on the method developed in [20], the point cloud constituting the surface mesh was imported into MATLAB [21] to evaluate the cross-sectional area along the bar and the geometrical parameters of the pit. The 3D surface mesh of one bar is shown in Fig. 19a, with details of the most severe pit amplified.

Fig. 19b shows the cross-sectional area A along the axis direction for one bar. The periodic variation in cross-sectional area of the plot is due to the presence of ribs on the bar surface. The local corrosion level is defined as the area loss percentage at each cross-section. According to Equation (1), the maximum local corrosion level, μ_{max} , is determined at the section with minimum remaining cross-sectional area, A_{min} :

$$\mu_{max} = \frac{A_{0,min} - A_{min}}{A_{0,min}} \quad (1)$$

where $A_{0,min}$ is the original cross-sectional area of the section with the minimum remaining cross-sectional area. The original uncorroded cross-section was found using an iterative process developed in [22] by comparing the healthy part of the corroded section with each section in the uncorroded segment covering a complete interval of transverse rib variation. The 3D coordinates of points composing the bar surface are shown in a 2D plot, with the colour representing the radius of every point, as in Fig. 19c. The appearance of the minimum cross-section and its original uncorroded section are shown in Fig. 19d. The pit length l_p was the length of the corrosion pit along the bar axis, while the pit depth x_p and pit width w_p were determined at the minimum cross-section, as shown in Fig. 19d.

Tensile test procedure

Monotonical uniaxial tensile tests were conducted on the steel bars, using an MTS universal testing machine and according to BS EN ISO standard [23]. At each bar end, a 60 mm length was clamped in the grip zones. Hence, the tested length subjected to tension was 380 mm for the 500

mm bars and 430 mm for two 550 mm bars. The loading was applied under displacement control, with a 0.5 mm/min rate in the elastic stage and 2 mm/min afterwards. The force applied and total machine displacement were recorded.

2.3.1 DIC system

The DIC measurements conducted in this study were carried out using the ARAMIS Adjustable camera system, equipped with 12Mp sensors, dual-LED lighting and ARAMIS Professional software. The camera resolution in this system is 4096 x 3000 pixels and the frame rate goes from 25 to 100 frames per seconds (fps). The measurement area ranges from 20 x 15 mm² to 5000 x 4000 mm².

Before testing, a stochastic speckle pattern was created on the bar surfaces by alternate spraying with black and white paint [24]. Fig. 20 shows the painted bars and Fig. 21 the experimental setup with the DIC equipment. The camera lenses were 75 mm and the system was initially calibrated to calculate the position and orientation of each camera. The camera rig was then adjusted horizontally and vertically, without changing the relative positions of the cameras. This was done to include the most severe pit in the measurement volume and allow the failure zone to be captured. Based on the quality of the speckle patterns generated on the bar surfaces, the measurement volume was set to 100 x 75 x 55 mm to ensure good measurement resolution, while the facet size was set to 15 x 13 pixels. The acquisition rate was set to 5 Hz. To reduce the file size of the results, only every twentieth image was stored (or every four seconds) by setting the frequency divider to 20. A ring buffer was set to ensure storage of the last 150 images before failure (equivalent to the last 30 seconds of the test). Moreover, the data logger of the MTS machine was connected to the ARAMIS software, to synchronise data measurements of the applied force and total displacement of the testing machine.

2.3.2 Post-processing of the DIC measurement

The results were post-processed in GOM Correlate Professional software [25]. The engineering strain was computed for this study; this is defined as the change of a reference length relative to its original length. The reference length for the strain calculations was defined by constructing virtual extensometers, using a built-in feature of the GOM software. To compare the strain at different regions of the corroded bars, a total of six virtual extensometers were created along the bar axis; three across the failure zone with lengths of 25, 50 and 75 mm, and three outside the failure zone with lengths of 5, 10 and 25 mm (see Fig. 22). The constraints of the measuring volume (and elongation of the bar itself) limited the maximum length of the virtual extensometer to 75 mm.

In the following sections, to avoid confusion when describing the strain values, the gauge length of the extensometer will be indicated, when necessary, as a superscript to the strain symbol ε . For example, ε^{50} represents the strain measured by the 50 mm gauge across the failure zone, and ε^{25_out} the 25 mm gauge outside it. Also, to validate the DIC measurements, a traditional extensometer was mounted on three specimens, with a gauge length of 50 mm. Fig. 23 shows the force-strain curve of one of the bars, which exhibits excellent agreement between both measurements.

2.3.3 Definitions of the mechanical parameters of bars

First, the terminology for the mechanical parameters studied in this paper was defined. The maximum force is termed “ultimate force”. Correspondingly, the stress at maximum force is defined as “ultimate strength”. The stress of corroded bars is calculated from the minimum cross-sectional area, as in Equation (2):

$$\sigma = \frac{F}{A_{min}} \quad (2)$$

where σ is the stress and F is the force.

For steel with an obvious yield plateau, as illustrated in Fig. 24a, the yielding force F_y and yield strength f_y can be defined according to the BS EN ISO standard [23]. However, for steel without a yield plateau, yield strength is replaced by proof strength, which is defined as the stress at a prescribed plastic or total extension [23]. Even though the uncorroded steel bars used in this study presented a distinct yield plateau, the pronounced effect of corrosion on the force-strain diagram made it difficult to accurately determine the force and stress upon yielding for corroded bars. Consequently, in this study, a total extension of 0.5% (based on a 50 mm extensometer) was defined as the proof strain. This is noted as $\varepsilon_{t0.5}$ and was measured so as to obtain the proof force (defined as the force at proof strain, noted as $F_{t0.5}$) and proof strength (noted as $f_{t0.5}$) of all the corroded bars, see Fig. 24b. It should be noted that for uncorroded bars and lightly corroded bars exhibiting the yield plateau, the proof strength $f_{t0.5}$ is nearly the same as the yield strength. This is because the proof strain of 0.5% is within the yield plateau, where the stress is almost constant.

The mechanical characteristics of the uncorroded bars were calculated by averaging the results of five uncorroded bars. From the average values of yielding force F_{y0} and ultimate force F_{u0} , and the nominal area of the uncorroded bars ($A_0 = 78.54 \text{ mm}^2$), the yield strength f_{y0} and ultimate strength f_{u0} were calculated as 532 MPa and 613 MPa. The strain at onset of yielding and hardening of uncorroded bars was $\varepsilon_{y0} = 0.27\%$ and $\varepsilon_{sh0} = 2.7\%$ respectively, while the strain at ultimate force ε_{u0} was 10.79%.

Results

This section presents the results of corrosion characteristics and mechanical parameters. All the data appears in Table 4 and Table 5.

Corrosion morphology

Along the rebar length, corrosion pits were generally found near the flexural cracks. In uncracked beams, numerous tiny pits were also formed on the surface of the bars. The observed shape of the pits was mainly elliptical, while some pits exhibited extended corrosion next to the elliptical cavity, probably caused by longitudinal corrosion-induced cracks along the beams. However, the pit length did not exceed 100 mm in any of the studied rebars. Surrounding the pit, the surface of the bars showed almost no corrosion. Unlike bars subjected to impressed current or natural corrosion for decades, the corrosion of the bars in this study was particularly localised. This may relate to the corrosion condition in the present study; the high chloride concentration may have caused a very high local corrosion rate in the pits. Moreover, during the relatively short exposure time (three years), the corrosion process near the flexural cracks had not been significantly influenced by corrosion-induced (longitudinal) cracks, as they had not developed along the whole beam length. Similar type of corrosion may be formed in practice due to the undesirable pre-existing cracks and/or highly non-uniform exposure conditions between different regions of the structures. The correlation between concrete cracks and corrosion characteristics of the beams in this study can be found in a previous study of the authors [26].

The relationships between the main pit morphology parameters shown in Table 4 were examined. Bars with higher maximum local corrosion level usually exhibited greater pit depth and pit width too, however, the correlations between maximum local corrosion level and pit depth

or pit width were generally poor. It was found that the product of the pit depth and pit width had a clear linear relationship to the maximum local corrosion level. Therefore, the maximum local corrosion level can actually reflect the combined feature of pit depth of pit width for the specimens in this study. The pit length, however, has no obvious correlation with the maximum local corrosion level or other pit geometries. In the following, the maximum local corrosion level was used as the main parameter for correlating with the mechanical properties, while the influence of pit length was examined as well on the strain properties.

Force-strain curves

The force-strain curves of all the bars are shown in Fig. 25. The strain in those curves was based on the 50 mm extensometer, which is five times the nominal diameter; a length specified in the BS EN ISO standard [23]. The colour of each curve, changing from dark blue to bright red, represents the maximum local corrosion level, μ_{max} , ranging from 0 to 35%. As clearly observed in Fig. 25, the shape of the force-strain curve is deeply affected by the maximum local corrosion level. Uncorroded steel bars exhibit a distinct yield plateau before strain-hardening. However, when μ_{max} is greater than about 10%, the yield plateau becomes indiscernible and the strain-hardening stage is simultaneously reduced, leading to a brittle failure at higher corrosion levels.

Strength versus maximum local corrosion level

The relationships of the proof and ultimate forces ($F_{t0.5}$ and F_u) to the maximum local corrosion level are shown in Fig. 26, in which a clear, decreasing linear trend is observed. These relationships were determined using the following linear expression, which is commonly used in the literature [14]:

$$F_{corr} = F_0(1 - \alpha\mu) \quad (3)$$

where F_{corr} is the proof or ultimate force of corroded bars, either $F_{t0.5}$ or F_u , F_0 is the yielding or ultimate force of uncorroded bars, either F_{y0} or F_{u0} , μ is the corrosion level (either average corrosion level or maximum local corrosion level) and α is the empirical coefficient indicating the degradation rate of the force loss (ranging from 1-3 in most previous studies). The maximum local corrosion level μ_{max} was used in the above expression. From the linear regression, the α coefficients were found to be 1.05 and 0.87 for the proof and ultimate forces respectively. These results indicate that the proof force decreases at a similar rate to that of the maximum cross-sectional area loss, while the degradation rate of the ultimate force is slightly less than the maximum cross-sectional area loss.

The proof and ultimate strengths ($f_{t0.5}$ and f_u) were obtained using Equation (2). Their relationships to the maximum local corrosion level are shown in Fig. 26b. There is no clearly observed dependence of strength on maximum local corrosion level. Considering the natural scatter of the strength of uncorroded bars, it may be inferred that the strength was almost unaltered. Indeed, a small increasing tendency is observed at higher corrosion levels, similar to the results reported in [5, 6, 14]. One possible explanation for this behaviour was given in [14], where it was hypothesised that bars with higher corrosion levels present less necking and that, consequently, the apparent stress (measured from the minimum cross-sectional area before loading) is closer to the true stress than for uncorroded steel bars.

Another possible reason may be related to the properties of TEMPCORE steel, which has a higher-strength martensitic crown and a lower-strength ferrite core. Although uniformly reducing the steel cross-section from the out-layer towards the inner core can result in a gradual loss of strength (as shown in [27]), this may not be the case for pitting corrosion. This is because, in bars with localised area loss at higher corrosion levels, the relative percentage of inner core

area loss may increase. However, this explanation needs further verification through the microstructure characterisation of the TEMPCORE steel cross-section.

Strain properties

3.4.1 Local strain distribution and evolution

The axial strain, computed as the maximum principal strain in the local coordinate, was examined at every point on the bar surface within the measuring volume captured using DIC. To illustrate how corrosion affected the axial strain distribution of bars and its evolution during the tensile test, seven different maximum local corrosion levels, including the uncorroded case, were selected for comparison: 0%, 5.4%, 11.2%, 15.7%, 20.4%, 26.0% and 32.7%. Fig. 27 shows the axial strain field at proof strain ($\varepsilon_{t0.5}$) and ultimate strain (ε_u), for each corrosion level. To facilitate comparison of the results between the seven bars, the upper and lower limits of the legend were kept constant. Histograms showing the distribution of local strain values along the bar were also displayed next to the legends.

Further, the local strain values along one longitudinal section (at proof and ultimate strains) were obtained for all bars shown in Fig. 27. These are plotted in Fig. 28, where the longitudinal strain distribution at different corrosion levels may be compared quantitatively. Additionally, the local strain distribution of the uncorroded bar at two loading stages additional to $\varepsilon_{t0.5}$ and ε_u (namely $\varepsilon_1 < \varepsilon_{t0.5}$ and $\varepsilon_2 > \varepsilon_u$) is shown in Fig. 29. At ε_1 , the strain distribution was uniform along the whole bar length; at $\varepsilon_{t0.5}$, yielding developed only within a limited region in the rebar. Subsequently, yielding and hardening spread along the whole bar without strain localisation until ε_u was reached. This implies that for the uncorroded bar, the ultimate strain (measured by extensometer) would be independent of gauge length and position, provided the gauge length was greater than the distance between two consecutive ribs. Finally, at ε_2 (a stage following necking of the uncorroded bar), strain localisation in the necking zone became apparent, as shown in Fig. 29.

From Fig. 28a, at the proof strain, the maximum value of the local strain for all the corroded bars was much higher than that of the uncorroded bar. This indicates very early strain localisation in corroded bars, even when the maximum local corrosion level was only 5.4%. At ultimate strain, the maximum local strain was also greater in corroded bars than in the uncorroded bar. This was because strain localisation for the uncorroded bar did not occur until after ultimate strain. At ultimate strain, it displayed a rather uniform strain distribution of about 10%. Conversely, corroded bars displayed much lower local strain values outside the pit; a phenomenon which becomes more pronounced as the maximum local corrosion level increases.

3.4.2 Ultimate strain ε_u^{50} versus μ_{max} and influence of pit length

The ultimate strain ε_u^{50} (normalised by the value of uncorroded steel bars ε_{u0}) versus the maximum local corrosion level μ_{max} is plotted in Fig. 30. There is a clear decreasing trend, yet the scatter is large; at similar maximum local corrosion levels, the measured strain differed by a factor of almost 2. As the pit shape in different bars was diverse in numerous ways, the scatter is not surprising when only the maximum local corrosion level was plotted against the ultimate strain. The other pit geometry parameters should also influence the ultimate strain. Since the pits introduce a sudden change in geometry that disrupts the strain field in a bar, it was hypothesised that pit length may play an important role in strain localisation. Thus, pit length was introduced in Fig. 30 to examine its influence and is depicted by marker colour. It can be observed that, at similar maximum local corrosion levels, most of the points with longer pit length have greater strain than shorter pits represented by the blue and green points.

The local strain distribution of bars with similar maximum local corrosion levels but a major difference in pit length was examined in the four bars (labelled in Fig. 30 by their respective numbers). Fig. 31 shows their local strain distribution at ultimate strain, plus their corrosion morphologies. In bars with longer pits, strain localisation occurred across a greater portion of the bar length. As a result, the strain over a given gauge length was greater (almost one time larger) for the bar with much longer pit length than the bar with shorter pit length although their maximum local corrosion level was close. Therefore, besides the maximum local corrosion level, the pit length also plays an important role in the ultimate strain of corroded bars.

3.4.3 Influence of gauge length and position on the relationship between ultimate strain versus μ_{max}

As the local axial strain is non-uniform along the corroded bars, the strain computed from different gauge lengths and at different locations varies. The ultimate strains from six different extensometers shown in Fig. 22 are compared in Fig. 32. They are all normalised in respect of the average ultimate strain for uncorroded bars. The ultimate strains calculated from the total elongation of the original tested length 380 or 430 mm, labelled as $l_g = 380 \text{ mm}$ are also shown in Fig. 32. The normalised ultimate strain shows clear decreasing tendencies with increasing μ_{max} , except for ϵ_u^{25} . For ϵ_u^{25} , some points are close to, or even greater than, the strain of uncorroded bars while others are less. This might be due to the fact that the pit length is greater than 25 mm for some bars. In this case, the extensometer can only measure the local yielding level inside the pit, while the strain outside the pit is not captured.

For the same bar, increasing the gauge length of the extensometer across the failure zone from 25 mm to 75 mm results in a decrease in ultimate strain. This can be explained by the progressive reduction of the relative contribution of the local strain in the pit to the total deformation over the gauge length, as the gauge length increases. Accordingly, the ultimate strain based on the total elongation of the tested length ϵ_u^{380} is further reduced, as can be seen in Fig. 32.

In contrast to this, the ultimate strain from the extensometers outside the failure zone is not influenced by the gauge length (5, 10 and 25 mm). Moreover, most values of $\epsilon_u^{5_{out}}$, $\epsilon_u^{10_{out}}$, $\epsilon_u^{25_{out}}$ are lower than ϵ_u^{380} , as the large local strain inside the pit contributes to an increase in the value of ϵ_u^{380} . In a few bars, however, the values of $\epsilon_u^{5_{out}}$, $\epsilon_u^{10_{out}}$, $\epsilon_u^{25_{out}}$ are greater. This can be explained by the position of the extensometers, which were located outside the failure zone but remained within the corrosion pit zone, where strain localisation still occurred.

Moreover, it is interesting to note that a sudden, greater loss of ultimate strain ($\epsilon_u^{5_{out}}$, $\epsilon_u^{10_{out}}$, $\epsilon_u^{25_{out}}$ and ϵ_u^{380}) occurred at a corrosion level between 13-15%. Quantitatively speaking, the ultimate strain values measured outside the pit for higher corrosion levels dropped below the yield strain of uncorroded bars, $\epsilon_{y0} = 0.27\%$. Conversely, the values of ϵ_u^{380} were still greater than the yield strain, even at greater corrosion levels, due to the contribution of strain localisation at the pit. From Fig. 27e-g, it can also be observed that the local strain outside the pit is below the yield strain for bars with higher corrosion levels. It may thus be inferred that a critical local corrosion level exists and that it prevents the yield penetration from developing outside the corrosion pit.

Discussion

Ultimate strain over any gauge length of corroded bars

When analysing the structural behaviour of reinforced concrete analytically or numerically in engineering practice, the reinforcing bars are usually treated as a homogeneous material. For

corroded rebars, since the strain capacity along the bar length becomes non-uniform due to the strain localisation, the defined ultimate strain of corroded rebars should be able to represent their strain capacity in an appropriate structural scale length. However, it is not obvious what gauge length should be used to determine the strain capacity of corroded bars. To be on the safe side, long gauge lengths should ideally be selected, although further study on this aspect is still required. This section has attempted to derive the ultimate strain of a corroded bar as a function of gauge length and corrosion level.

4.1.1 Lower-bound solution of the ultimate strain of corroded bars with single localised pit

This section proposes an analytical model for calculating the ultimate strain of a corroded bar, for cases when the gauge length, l_g , is greater than the pit length, l_p , as presented schematically in Fig. 33. According to the results from the DIC measurement described above, the distribution of local strain in a pit was found to be strongly dependent on pit morphology, whilst being almost constant outside the pit, except for the rib effect. Therefore, the ultimate strain of a corroded bar may be obtained from the following equation:

$$\varepsilon_u^{l_g} = \frac{\int_0^{l_g} \varepsilon_u(x) dx}{l_g} = \frac{\int_0^{l_p} \varepsilon_u(x) dx + (l_g - l_p) \varepsilon_u^{out}}{l_g} \quad (3)$$

where $\varepsilon_u^{l_g}$ is the ultimate strain over the gauge length, l_g , $\varepsilon_u(x)$ is the local strain at ultimate strain (which is dependent on the pit morphology) and ε_u^{out} is the ultimate strain outside the pit, over any gauge length greater than one rib spacing.

To express the ultimate strain outside the pit ε_u^{out} , the ultimate stress outside the pit σ_u^{out} was first described. The local bending effect in the pit was considered negligible, so a uniaxial force equilibrium was established. Furthermore, the ultimate strength was assumed to be unaffected by corrosion, as only a slight increase was observed at higher corrosion levels, as presented in section 3.3. When the stress in the minimum cross-section reaches the ultimate strength f_{u0} , the stress outside the pit can be calculated from:

$$\sigma_u^{out} A_0 = f_{u0} A_{min} \quad (4)$$

As the minimum cross-sectional area A_{min} is related to the maximum local corrosion level through Equation (1), the stress outside the pit can be expressed as a function of the maximum local corrosion level:

$$\sigma_u^{out} = f_{u0} (1 - \mu_{max}) \quad (5)$$

The stress-strain relationship of the steel outside the pit follows the constitutive law of the uncorroded steel. However, the stress and strain state cannot reach the ultimate state of uncorroded steel, due to premature failure in the pit. The following formula was adopted for the constitutive law of uncorroded steel. It incorporates a linear elastic part, yield plateau and strain-hardening curve described by a power function [28]:

$$\sigma = \begin{cases} E_0 \varepsilon, & \varepsilon < \varepsilon_{y0} \\ f_{y0}, & \varepsilon_{y0} \leq \varepsilon \leq \varepsilon_{sh0} \\ f_{u0} - (f_{u0} - f_{y0}) \left(\frac{\varepsilon_{u0} - \varepsilon}{\varepsilon_{u0} - \varepsilon_{sh0}} \right)^P, & \varepsilon_{sh0} < \varepsilon \leq \varepsilon_{u0} \end{cases} \quad (6)$$

where E_0 is Young's modulus, equal to $\frac{f_{y0}}{\varepsilon_{y0}}$, and P is the strain-hardening power, as defined in Equation (7) [28]:

$$P = E_{sh0} \frac{\varepsilon_{u0} - \varepsilon_{sh0}}{f_{u0} - f_{y0}} \quad (7)$$

where E_{sh0} is the tangent slope at the onset of strain-hardening, ε_{sh0} , also referred to as strain-hardening modulus. From the experimental results from five uncorroded bars, the strain-hardening modulus was about $0.15E_0$. Fig. 34a shows the experimental stress-strain curves of these five uncorroded bars and the theoretical constitutive law, as described by Equation (6).

From Equation (6), the strain is expressed in terms of the stress, as in Equation (8):

$$\varepsilon = \begin{cases} \frac{\sigma}{E_0}, & \sigma < f_{y0} \\ \in [\varepsilon_{y0}, \varepsilon_{sh0}], & \sigma = f_{y0} \\ \varepsilon_{u0} - (\varepsilon_{u0} - \varepsilon_{sh0}) \left(\frac{f_{u0} - \sigma}{f_{u0} - f_{y0}} \right)^P, & f_{y0} < \sigma \leq f_{u0} \end{cases} \quad (8)$$

Replacing the stress σ in Equation (8) by σ_u^{out} in Equation (5), the following relationship between the ultimate strain outside the pit and maximum local corrosion level can be expressed:

$$\varepsilon_u^{out} = \begin{cases} \varepsilon_{u0} - (\varepsilon_{u0} - \varepsilon_{sh0}) \left(\frac{f_{u0}}{f_{u0} - f_{y0}} \mu_{max} \right)^P, & \mu_{max} < \mu_{crit} \text{ or } f_{y0} < \sigma_u^{out} \leq f_{u0} \\ \in [\varepsilon_{y0}, \varepsilon_{sh0}], & \mu_{max} = \mu_{crit} \text{ or } \sigma_u^{out} = f_{y0} \\ \frac{f_{u0} \varepsilon_{y0}}{f_{y0}} (1 - \mu_{max}), & \mu_{max} > \mu_{crit} \text{ or } \sigma_u^{out} < f_{y0} \end{cases} \quad (9)$$

where μ_{crit} represents the critical local corrosion level above which the bar outside the pit would not yield upon failure within the pit, expressed as follows:

$$\mu_{crit} = 1 - \frac{f_{y0}}{f_{u0}} \quad (10)$$

From the values of f_{y0} and f_{u0} of the bars in this study, the critical local corrosion level μ_{crit} is calculated as 13.3%.

It is interesting to note that the decreasing trend in ultimate strain outside the pit with increasing maximum local corrosion level follows exactly the full constitutive law of uncorroded steel, with the stress replaced by $f_{u0}(1 - \mu_{max})$, as shown in Fig. 34b. Further, the comparison between the theoretical results of ε_u^{out} from Equation (9) and experimental results of $\varepsilon_u^{25.out}$ in Fig. 34b shows good agreement on the location of the critical local corrosion level, where a sudden drop in ultimate strain was observed for the experimental data $\varepsilon_u^{25.out}$. However, the experimental data generally shows greater strain values than the analytical solution of ε_u^{out} . This may be because the experimental specimens did not have the idealised single pit shown in Fig. 33. Other minor pits also existed in some bars, which also led to some strain localisation outside the failure zone. Also, in some bars, the 25mm extensometer outside the failure zone was actually located across part of the corrosion region, due to the DIC's limitations in capturing volume.

The strain inside the pit is much more complex as it is non-uniform and dependent on both the maximum local corrosion level and pit morphology. However, the ultimate strain outside the pit, ε_u^{out} in Equation (9) can be regarded as a lower-bound solution of Equation (3) when $l_g \gg l_p$, as it is on the safe side to neglect the strain inside the pit. Consequently, a lower bound for the ultimate strain of a corroded rebar can be estimated directly from the constitutive law for uncorroded rebars, if the maximum local corrosion level is known. This may prove very valuable in engineering practice.

To determine a more accurate ultimate strain value, including the contribution of local strain within the pit, the relationship between local strain distribution and pit morphology needs to be unravelled. Nevertheless, a semi-analytical model is proposed below, as a feasible means of calculating a more accurate ultimate strain value over any gauge length. This is based on the proposed analytical method, using the empirical relationships between ultimate strain and maximum local corrosion level shown in the experimental data from the present study.

4.1.2 Semi-analytical model for rebars in this study

Although the first part of the numerator in Equation (3) $\int_0^{l_p} \varepsilon_u(x)dx$ (the total strain within the pit) is not known explicitly for each corrosion level, the strain measured from the extensometer across the failure zone included this part. From the experimental results in this study, an empirical relationship was obtained for the ultimate strain over a 50 mm extensometer ε_u^{50} , as a function of the maximum local corrosion level. For the second part of the numerator in Equation (3), the strain outside the pit, ε_u^{out} , can be described by Equation (9), or related empirically to the maximum local corrosion level from the experimental results. As discussed in the previous section, Equation (9) gives lower values than the experimental data. Therefore, an empirical relationship of $\varepsilon_u^{25.out}$ versus the maximum local corrosion level from the experimental results was used.

With empirical relationships describing ε_u^{50} and $\varepsilon_u^{25.out}$ as functions of the maximum local corrosion level, the ultimate strain over any gauge length greater than 50 mm can be calculated as:

$$\varepsilon_u^{l_g} = \frac{(50\text{mm}) \varepsilon_u^{50} + (l_g - 50\text{mm}) \varepsilon_u^{25.out}}{l_g} \quad (11)$$

An exponential fitting was conducted for ε_u^{50} versus maximum local corrosion level. This fitting has been commonly used in previous studies [5, 6, 10, 11]. A piecewise relationship was used for the relationship between $\varepsilon_u^{25.out}$ and maximum local corrosion level, as the ultimate strain dropped suddenly at the critical local corrosion level. Using an exponential formula (below the critical local corrosion level) and a linear decreasing line (above the critical local corrosion level), the experimental results were well fitted, see Fig. 35a. Theoretically, the exponential curve passes the point (0,1) which represents the average ultimate strain of tested uncorroded bars. Moreover, the second branch for $\varepsilon_u^{25.out}$ ends at the point (1,0), representing zero strain capacity when the maximum local corrosion level approaches 100%. The empirical relationships for ε_u^{50} and $\varepsilon_u^{25.out}$ are given in Equations (12) and (13):

$$\varepsilon_u^{50} = \varepsilon_{u0} e^{-2.78\mu_{max}} \quad (12)$$

$$\varepsilon_u^{25.out} = \begin{cases} \varepsilon_{u0} e^{-8.38\mu_{max}}, & \mu_{max} < \mu_{crit} \\ \varepsilon_{u0} (0.0262)(1 - \mu_{max}), & \mu_{max} \geq \mu_{crit} \end{cases} \quad (13)$$

The experimental results and fitting relationships are shown in Fig. 35a, with the semi-analytical results of $\varepsilon_u^{l_g}$ for l_g equal to 100, 200, 300, 400 and 500 mm obtained from Equations (11-13). For a given maximum local corrosion level, as the gauge length increases, the ultimate strain decreases and tends to approach the value of $\varepsilon_u^{25.out}$. Taking the gauge lengths as 75 mm and 380 mm, the semi-analytical results compare well with the experimental results of ε_u^{75} and ε_u^{380} , as shown in Fig. 35b. As a result, the semi-analytical model can be used to calculate the ultimate strain over any gauge length greater than 50 mm for bars which have localised pitting corrosion and material properties similar to the bars in this study.

Comparison of the ultimate strain with the literature

The present experimental data was compared to the results of three previous studies which also measured the maximum local corrosion level of the bars. From Fig. 36, the first noteworthy observation is the large range of results obtained across the different studies. As described in section 3.4.3, the reported strain values depend on the gauge length used, so the comparison has been made under conditions that are as similar as possible.

A study was reviewed in which the total tested length of the bars (203 mm) had been used to evaluate the ultimate strain (cf. [6]). The results were then compared to those from this study, in which the total elongation had also been measured. This comparison revealed that, for a similar corrosion level, the loss of ultimate strain in the present study was much greater than in [6]. This may be explained by the different corrosion morphologies of the bars in each study. The bars in [6] were corroded along the whole bar surface under impressed current, as opposed to the localised pitting corrosion seen in this study. This indicates that localised pitting corrosion impacts the ductility of corroded bars more adversely than extensive pitting corrosion.

Comparing the results of [13, 14], in which short extensometer gauge lengths were adopted (60 mm and 50 mm; similar to the 50 mm extensometer used in this study), again, it may be seen that, for a similar corrosion level, most values in [13, 14] are greater than those in the present study. The bars in [13, 14] were naturally corroded in real structures. Extensive pitting corrosion along the whole bar surface was observed according to the 3D-scanning results reported in [13, 14]. As a result, the bar surfaces in [13, 14] presented conspicuous corrosion over the entire length of the extensometer gauge, whereas most of the bars in the present study featured pit lengths shorter than the 50 mm gauge length, as shown in Table 4. Consequently, strain localisation most likely did not occur to the same extent in the bars with extensive pitting corrosion and thus greater ultimate strains were obtained than in this study.

Time-dependent assessment of the strain capacity

The corrosion morphology of rebars in real structures is commonly classified as general corrosion induced by concrete carbonation, or pitting corrosion induced by chlorides. For chloride-induced corrosion, the corrosion morphology evolves during the corrosion propagation period. At an early stage, localised pitting corrosion is more likely to initiate near pre-existing cracks, as observed in this study. However, as corrosion-induced cracks propagate longitudinally in rebars, chlorides, oxygen and moisture may penetrate through them, thus promoting broader development of pitting corrosion along the bar length. This argument has also been manifested in [29], in which the study authors compared the corrosion morphology and corrosion-induced cracks of RC beams at different exposure times.

Since the strain capacity of corroded reinforcement bars is significantly affected by corrosion morphology, the time-varying nature of corrosion morphology must therefore be borne in mind when making an assessment. A hypothesis is proposed to illustrate the time-dependent strain capacity at three different corrosion stages in which distinct corrosion patterns are dominant, see Fig. 37. In stage I, corrosion pits are only formed locally; the majority of bars in this study exhibit the corrosion morphology of this stage. The strain capacity decreases rapidly with increasing maximum local corrosion level. In stage II, pits grow along the bar as corrosion-induced cracks develop; a few bars in this study can be classified to this stage. As discussed in section 3.4.2, longer pits most likely have greater strain capacity than shorter ones of similar maximum local corrosion level. It is therefore feasible that the strain capacity may be partially recovered in this stage. In stage III, when the corrosion-induced cracks extend and connect throughout the whole beam surface, corrosion eventually spreads over the whole rebar surface. The corrosion morphology in this stage is that commonly seen in rebars taken from the real structures that

have been corroded for decades, as in [13, 14]. The comparison of the ultimate strain with the results from the literature [13, 14] in section 4.2 has shown that the degradation of strain capacity in naturally corroded bars with increasing maximum local corrosion level is slower compared to the bars in this study. Consequently, a more gentle slope is expected for the decreasing trend in strain capacity at this stage.

Finally, a naturally corroded rebar retrieved from the edge beam of a real bridge (the Stallbacka Bridge) after 35 years in service [14], was also examined using DIC. The local strain distribution of the naturally corroded rebar was compared to that of a bar with similar maximum local corrosion level and the longest pit length corroded in the laboratory of this study (bar #130), as shown in Fig. 38. Both bars were corroded along the entire length of the DIC capture volume. Large local strains were observed along the whole bar; however, the distribution of the local strain in the naturally corroded bar had more peaks, due to its more irregular corrosion pattern. The ultimate strain for the two bars (based on a 50 mm gauge length) is close. However, the corrosion level (as determined by the total weight loss, μ_{weight}) of the bar in this study was much lower than that of the naturally corroded bar, since the latter was severely corroded across its entire surface. As a result, with increasing corrosion time, although the total steel loss increases, the strain capacity may not necessarily decrease as it depends largely on the corrosion morphology. To predict the time-dependent strain capacity of corroded rebars requires further studies on the evolution of corrosion morphology with concrete cracking and corrosion time.

Conclusions

This paper has studied the tensile behaviour of reinforcement bars exhibiting localised pitting corrosion. The non-uniform local strain distribution along the bar length was captured during tensile testing, using the DIC technique. This revealed that the measured ultimate strain was dependent on the extensometer gauge length for a given corrosion pit. The strain localisation in the corrosion pit led to premature failure, whereupon the strain outside the pit could not adequately develop. A lower bound for the ultimate strain in corroded bars with a single localised pit was given as the ultimate strain that can be reached outside the pit. In summary, the following conclusions were drawn from this study:

- (1) The shape of the force-strain curve of steel bars was strongly influenced by corrosion. With increasing corrosion level, the force-strain curves displayed earlier yielding, with the yielding plateau disappearing progressively. The proof and ultimate forces decreased linearly with the maximum local corrosion level. However, the proof and ultimate strengths that were based on the minimum remaining cross-sectional area remained nearly constant as the corrosion level increased. There was a slight ascending trend at higher corrosion levels.
- (2) The measured ultimate strain of corroded bars depends strongly on gauge length. Caution is therefore advised if experimental results or empirical relationships relating to ultimate strain will be used to assess corroded structures, as few previous studies have covered this.
- (3) The ultimate strain outside the corrosion pit reduced significantly as the maximum local corrosion level increased. Moreover, a sudden great loss was observed at a critical local corrosion level. When this was exceeded, the bar outside the pit did not yield. It was shown that the critical local corrosion level is 1 minus the ratio between yield strength and ultimate strength. For the rebars in this study, the value was 13.3%.
- (4) A simple analytical model giving a lower-bound solution for ultimate strain was proposed. This was expressed as a function of the mechanical parameters of uncorroded steel and

maximum local corrosion level. It compared well with the experimental results and may prove valuable when used in engineering practice.

(5) The empirical relationships were determined of the ultimate strain to the maximum local corrosion level for results from a 50 mm extensometer across the failure zone and a 25 mm extensometer outside it. Based on them, a semi-analytical model was formulated to calculate the ultimate strain over any gauge length exceeding 50 mm. A good comparison was obtained, between the calculated ultimate strain across a long gauge and the experimental results. The choice of the most appropriate gauge length to describe the strain capacity of corroded rebars in concrete structures is a question that requires further study. However, to be on the safe side, a long gauge length should be used.

(6) At similar maximum local corrosion levels, bars with much longer pit length in this study displayed a greater ultimate strain than bars with shorter pit length. Moreover, via comparison with the literature, localised pitting corrosion was found to reduce strain capacity more than extensive pitting corrosion.

(7) As corrosion morphology progresses from localised pitting corrosion (during early corrosion) to extensive pitting corrosion as corrosion-induced cracks propagate, the strain capacity of corroded rebars may initially decrease more rapidly. Thereafter, it may decrease slowly and even gradually increase as the corrosion time progresses. For this reason, it is important to quantify the corrosion morphology and relate it to the strain capacity of corroded bars.

Credit authorship contribution statement

E Chen: Conceptualization, Investigation, Methodology, Formal analysis, Visualization, Writing – Original Draft.

Carlos G.Berrocal: Conceptualization, Software, Methodology, Writing – Review & Editing.

Ignasi Fernandez: Conceptualization, Resources, Writing – Review & Editing.

Ingemar Löfgren: Conceptualization, Funding acquisition, Project administration, Writing – Review & Editing.

Karin Lundgren: Conceptualization, Formal analysis, Supervision, Writing – Review & Editing.

Declaration of Competing Interest

The authors declare that they have no conflict interest.

Acknowledgements

The work reported in this paper has been supported by: the Swedish Transport Administration, under the project grant TRV 2018/36506; the construction industry's organisation for research and development (SBUF) under the project grant 13683; Chalmers University of Technology; Thomas Concrete Group; and Cements AB (Heidelberg Cement Group).

Reference

- [1] Du Y, Clark L, Chan A. Residual capacity of corroded reinforcing bars. *Magazine of Concrete Research*. 2005;57:135-47.
- [2] Cairns J, Plizzari GA, Du Y, Law DW, Franzoni C. Mechanical properties of corrosion-damaged reinforcement. *ACI Materials Journal*. 2005;102:256.

- [3] Zhang W, Song X, Gu X, Li S. Tensile and fatigue behavior of corroded rebars. *Construction and Building Materials*. 2012;34:409-17.
- [4] Apostolopoulos CA, Demis S, Papadakis VG. Chloride-induced corrosion of steel reinforcement–Mechanical performance and pit depth analysis. *Construction and Building Materials*. 2013;38:139-46.
- [5] François R, Khan I, Dang VH. Impact of corrosion on mechanical properties of steel embedded in 27-year-old corroded reinforced concrete beams. *Materials and Structures*. 2013;46:899-910.
- [6] Tang F, Lin Z, Chen G, Yi W. Three-dimensional corrosion pit measurement and statistical mechanical degradation analysis of deformed steel bars subjected to accelerated corrosion. *Construction and Building Materials*. 2014;70:104-17.
- [7] Moreno E, Cobo A, Palomo G, González MN. Mathematical models to predict the mechanical behavior of reinforcements depending on their degree of corrosion and the diameter of the rebars. *Construction and Building Materials*. 2014;61:156-63.
- [8] Fernandez I, Bairán JM, Marí AR. Corrosion effects on the mechanical properties of reinforcing steel bars. Fatigue and σ – ϵ behavior. *Construction and Building Materials*. 2015;101:772-83.
- [9] Qiao D, Nakamura H, Yamamoto Y, Miura T. Evaluation method of tensile behavior of corroded reinforcing bars considering radius loss. *Journal of Advanced Concrete Technology*. 2015;13:135-46.
- [10] Lu C, Yuan S, Cheng P, Liu R. Mechanical properties of corroded steel bars in pre-cracked concrete suffering from chloride attack. *Construction and Building Materials*. 2016;123:649-60.
- [11] Zhu W, François R, Poon CS, Dai J-G. Influences of corrosion degree and corrosion morphology on the ductility of steel reinforcement. *Construction and Building Materials*. 2017;148:297-306.
- [12] Sun X, Kong H, Wang H, Zhang Z. Evaluation of corrosion characteristics and corrosion effects on the mechanical properties of reinforcing steel bars based on three-dimensional scanning. *Corrosion Science*. 2018;142:284-94.
- [13] Subramanian SJ, Sharma S, Rajagopal R, Pillai RG. Assessment of Stress-Strain Behavior of Corroded Steel Reinforcement Using Digital Image Correlation (DIC). *Journal of Testing and Evaluation*. 2018;46:1874-90.
- [14] Fernandez I, Berrocal CG. Mechanical Properties of 30 Year-Old Naturally Corroded Steel Reinforcing Bars. *International Journal of Concrete Structures and Materials*. 2019;13:9.
- [15] Fernandez I, Bairán JM, Marí AR. Mechanical model to evaluate steel reinforcement corrosion effects on σ – ϵ and fatigue curves. Experimental calibration and validation. *Engineering Structures*. 2016;118:320-33.
- [16] Angst U, Elsener B, Jamali A, Adey B. Concrete cover cracking owing to reinforcement corrosion–theoretical considerations and practical experience. *Materials and Corrosion*. 2012;63:1069-77.
- [17] Eurocode. 2: design of concrete structures–Part 1-1: general rules and rules for buildings: EN 1992-1-1. European Committee for Standardization; 2004. p. 225.
- [18] Berrocal CG, Löfgren I, Lundgren K, Tang L. Corrosion initiation in cracked fibre reinforced concrete: influence of crack width, fibre type and loading conditions. *Corrosion Science*. 2015;98:128-39.
- [19] Fernandez I, Lundgren K, Zandi K. Evaluation of corrosion level of naturally corroded bars using different cleaning methods, computed tomography, and 3D optical scanning. *Materials and Structures*. 2018;51:78.
- [20] Tahershamsi M, Fernandez I, Lundgren K, Zandi K. Investigating correlations between crack width, corrosion level and anchorage capacity. *Structure and Infrastructure Engineering*. 2017;13:1294-307.
- [21] MATLAB R2017b. The MathWorks, Inc. Natick, Massachusetts, United States.
- [22] Berrocal CG, Löfgren I, Lundgren K. The effect of fibres on steel bar corrosion and flexural behaviour of corroded RC beams. *Engineering Structures*. 2018;163:409-25.
- [23] ISO. BS EN 6892-1. Metafile Metallic materials-Tensile testing-Part 12016.
- [24] Cato A, Raju MR. Mechanical properties of naturally corroded steel bars: Experimental study [Master of Science]. Göteborg, Sweden: Chalmers Univeristy of Technology; 2018.
- [25] GOM Correlate Professional 2018.
- [26] Chen E, Berrocal CG, Löfgren I, Lundgren K. Correlation between concrete cracks and corrosion characteristics of steel reinforcement in pre-cracked plain and fibre-reinforced concrete beams. *Materials and Structures*. 2020;53:1-22.

- [27] Fernandez I, Bairán JM, Marí AR. 3D FEM model development from 3D optical measurement technique applied to corroded steel bars. *Construction and Building Materials*. 2016;124:519-32.
- [28] Mander JB. Seismic design of bridge piers. Christchurch, New Zealand: University of Canterbury; 1983.
- [29] Zhang R, Castel A, François R. The corrosion pattern of reinforcement and its influence on serviceability of reinforced concrete members in chloride environment. *Cement and Concrete Research*. 2009;39:1077-86.

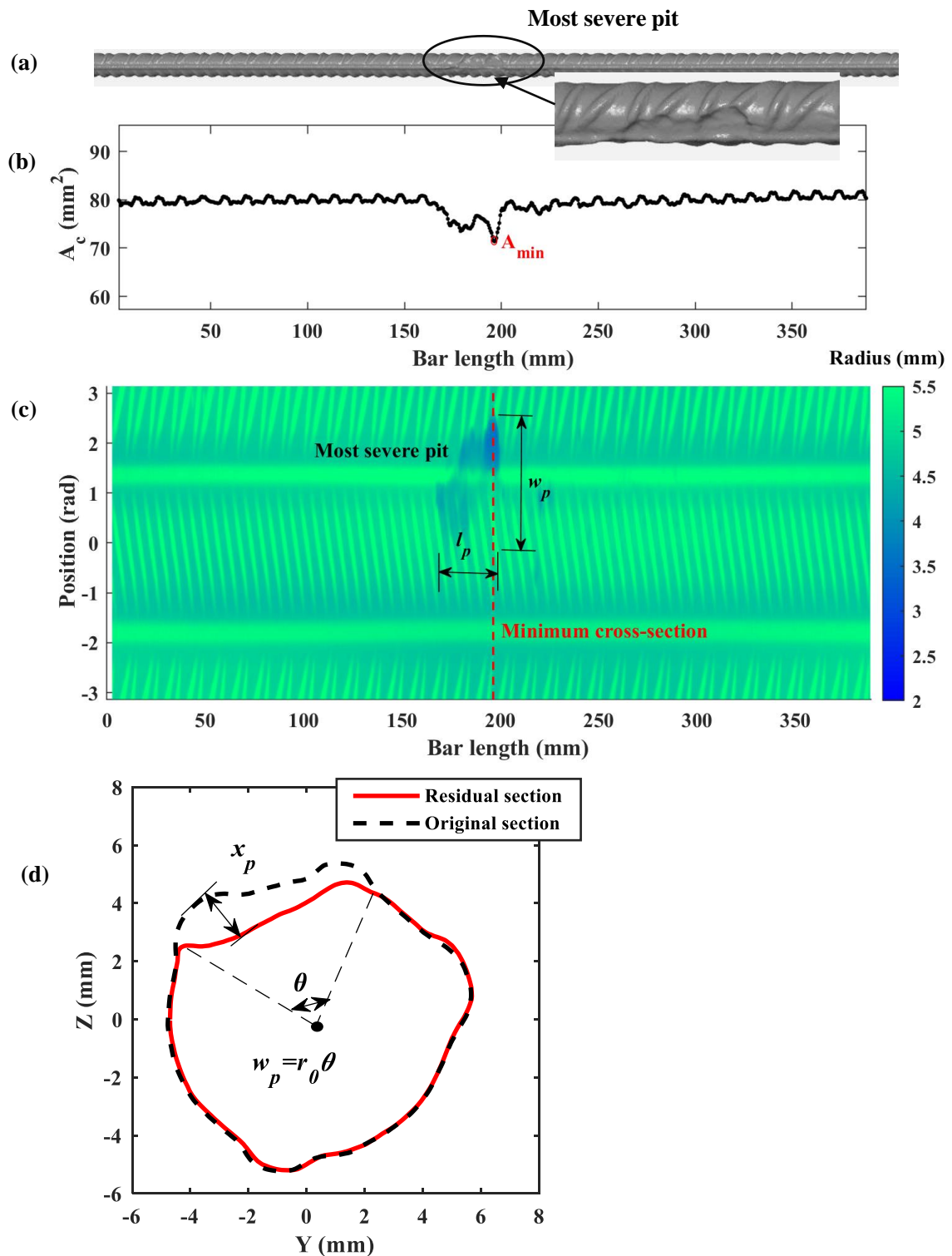


Fig. 19. Example illustrating corrosion evaluation from 3D-scanning: (a) reconstructed bar surface from 3D-scanning; (b) longitudinal variation of cross-sectional area along the scanned length; (c) 2D plot of the bar surface with colour scale showing the magnitude of radius; (d) residual and original cross-sectional appearance at the minimum cross-section.



Fig. 20. Steel bars with stochastic paint.

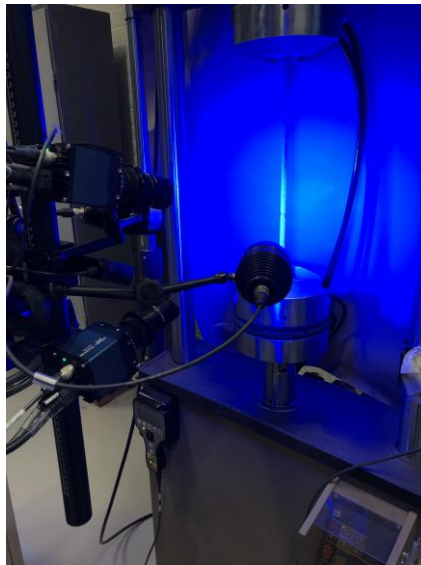


Fig. 21. DIC setup for the tensile test.

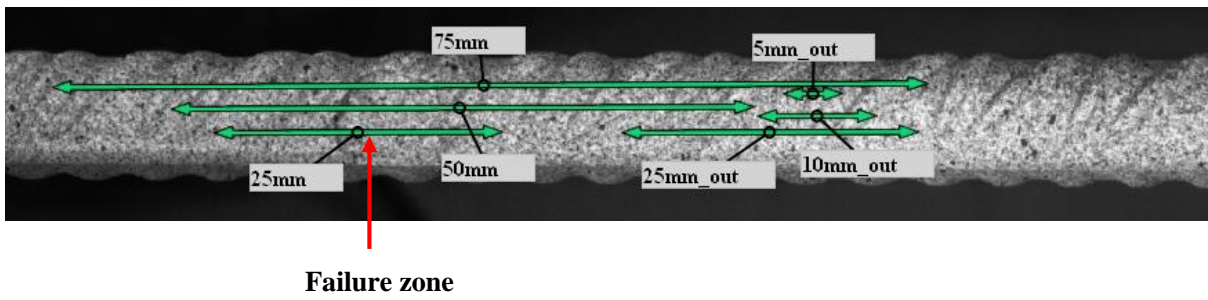


Fig. 22. Extensometers defined in the DIC post-processing software.

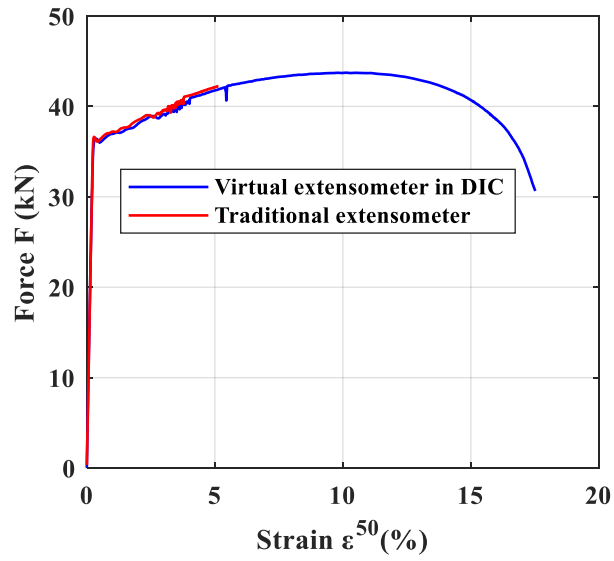


Fig. 23. Comparison of force-strain curves from the DIC and traditional extensometer.

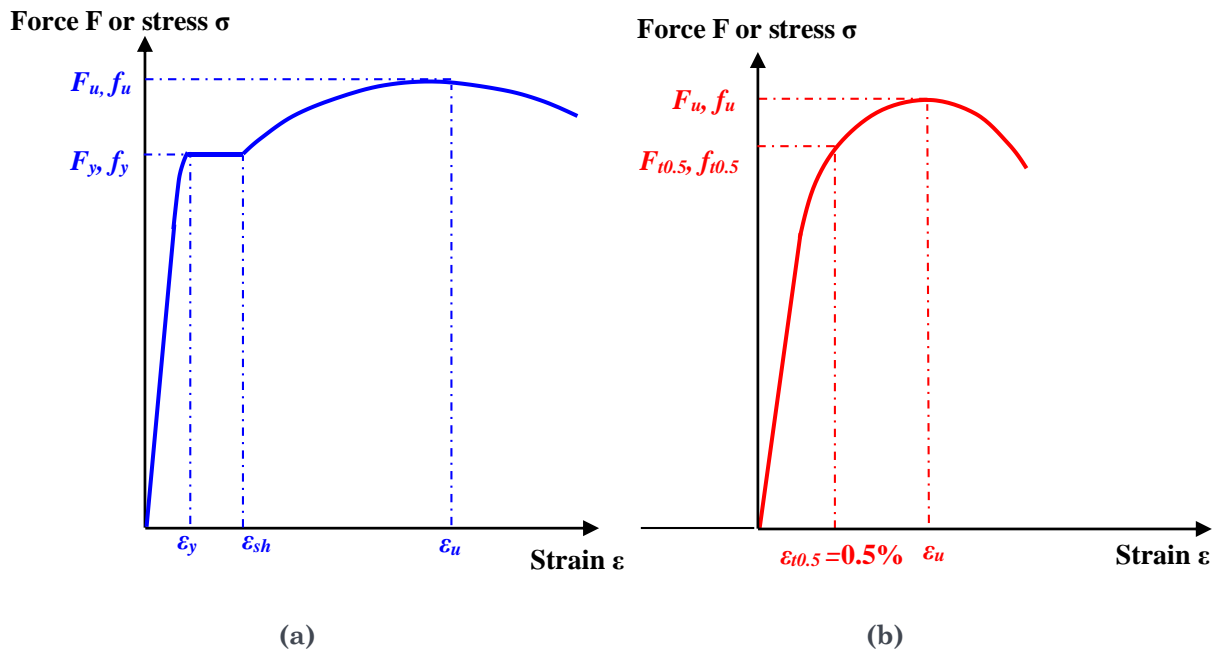


Fig. 24. Definition of main mechanical parameters according to the standard [23]: (a) for steel with obvious yield plateau; (b) for steel without yield plateau.

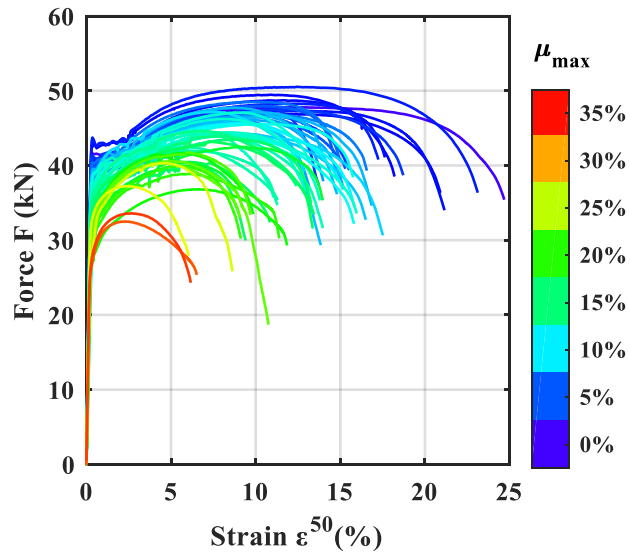
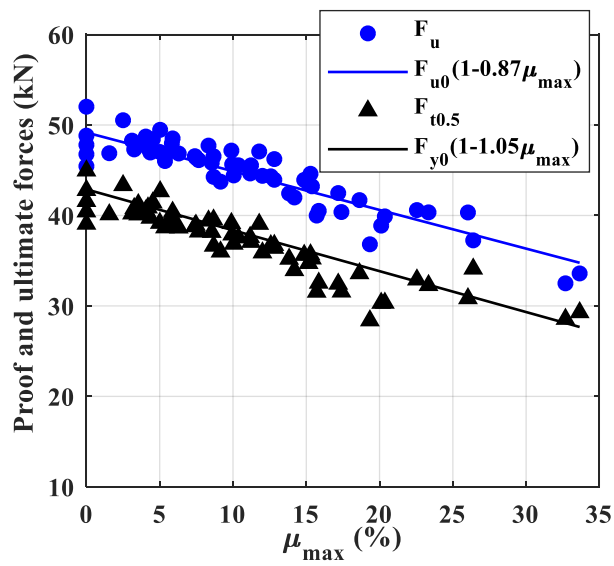


Fig. 25. Force-strain curves of bars with different maximum local corrosion levels.



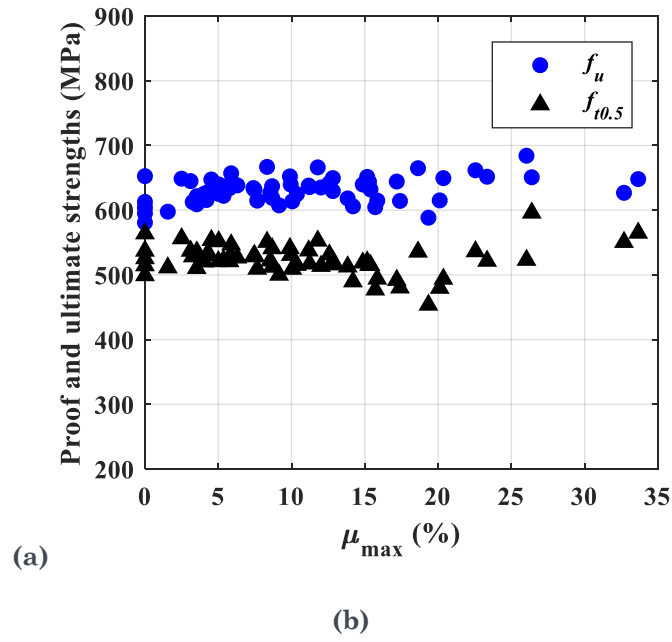
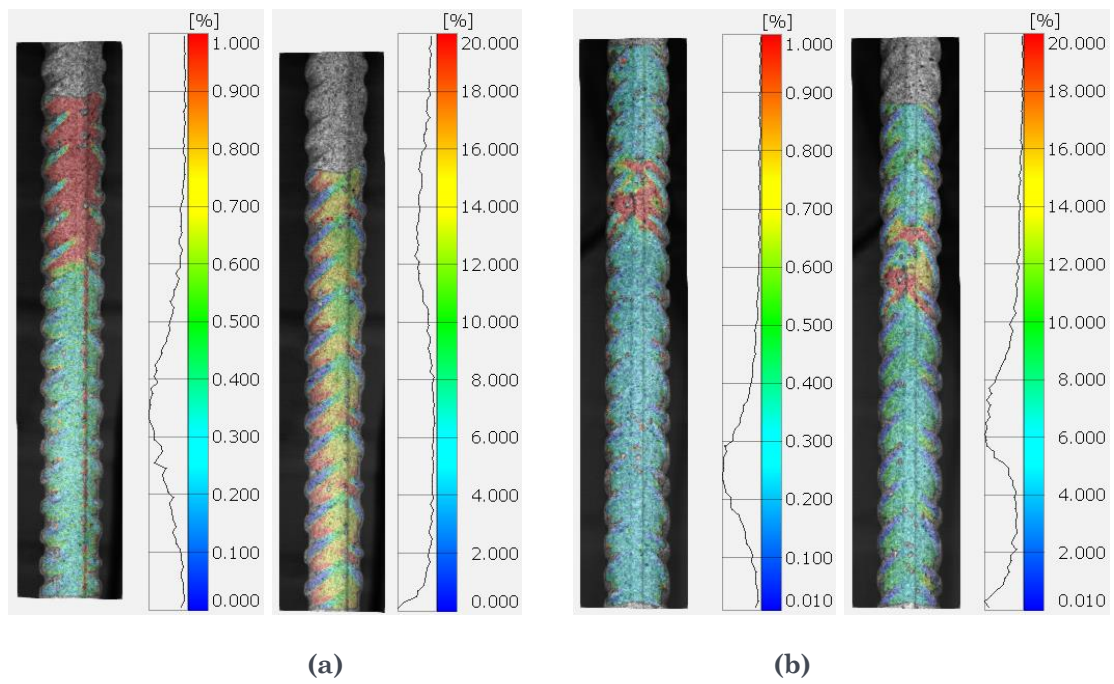
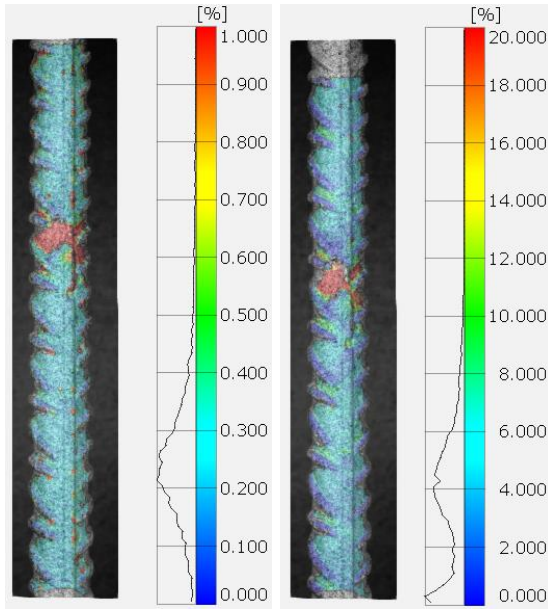
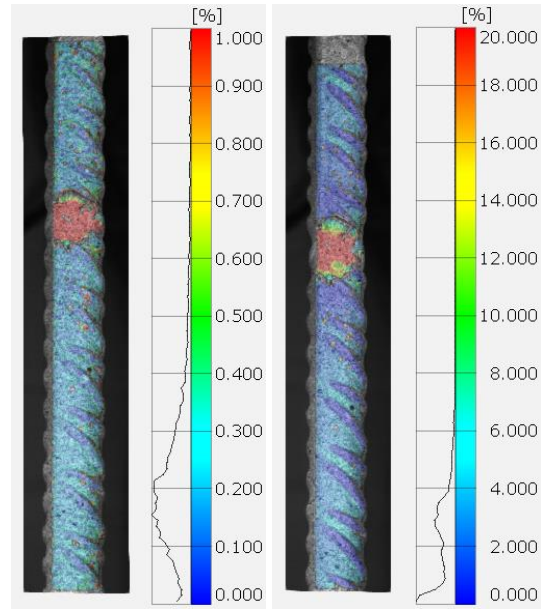


Fig. 26. (a) Proof and ultimate forces versus maximum local corrosion level, with fitting relations; (b) proof and ultimate strengths versus maximum local corrosion level.

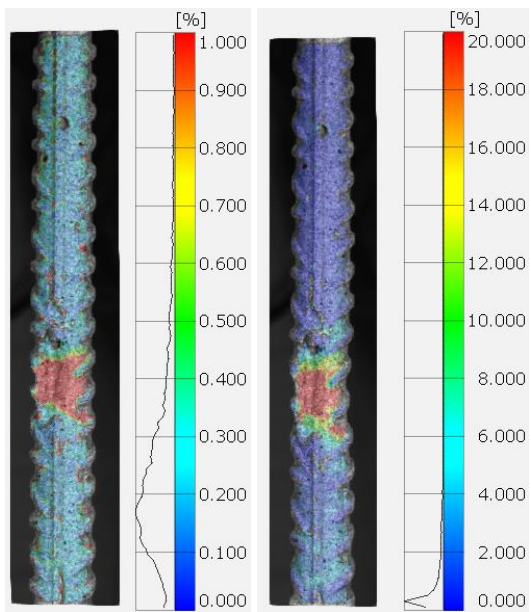




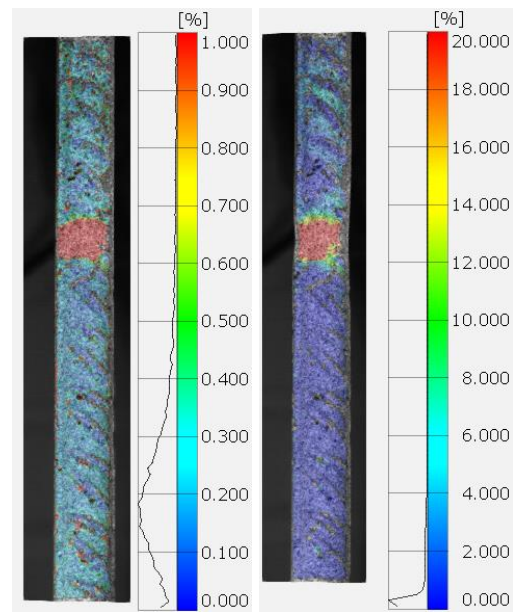
(c)



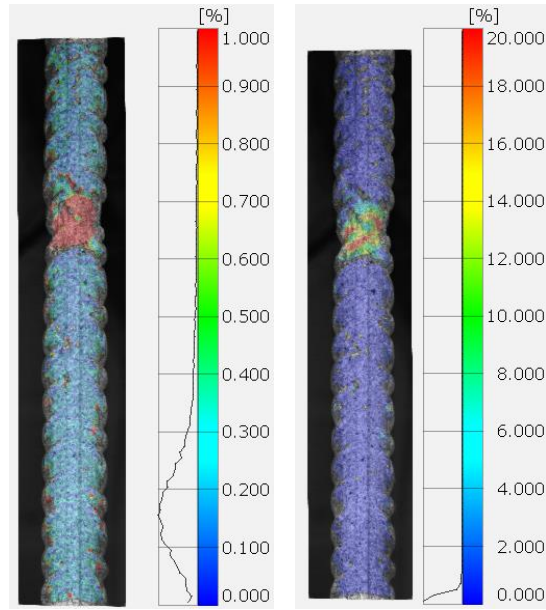
(d)



(e)

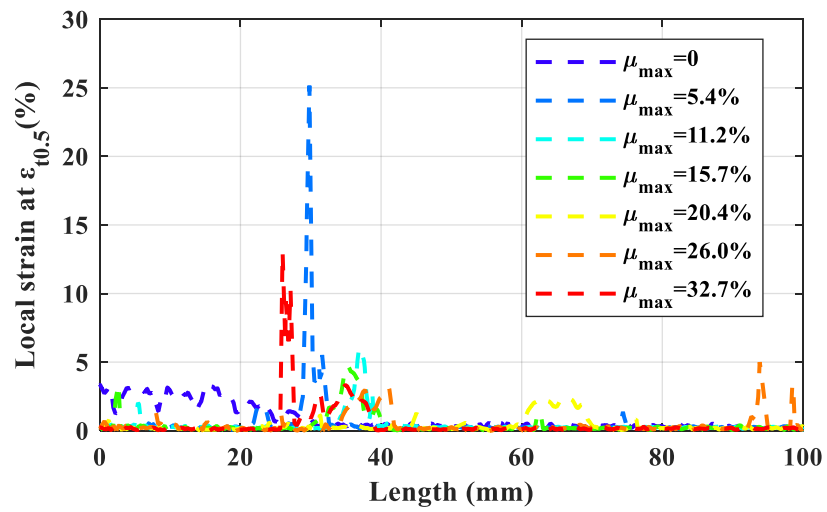


(f)

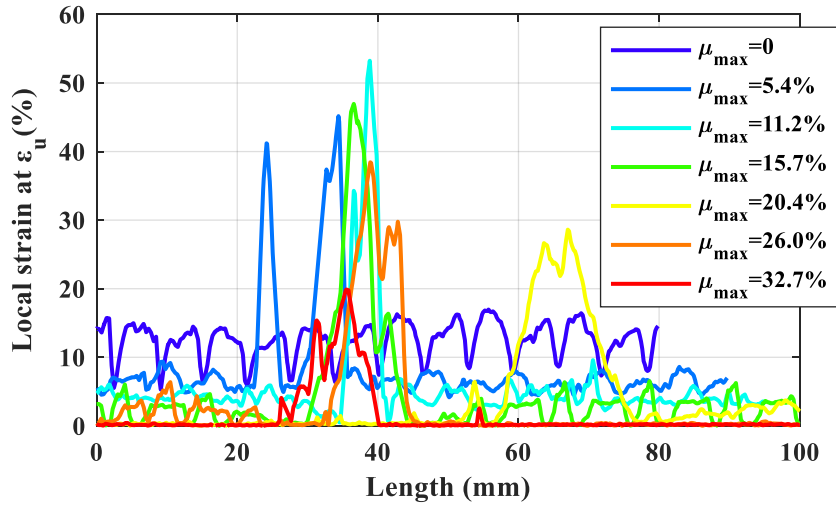


(g)

Fig. 27. Local axial strain field at $\epsilon_{t0.5}$ and ϵ_u for different corrosion levels: (a) $\mu_{max}=0\%$ (b) $\mu_{max}=5.4\%$; (c) $\mu_{max}=11.2\%$; (d) $\mu_{max}=15.7\%$ (e); $\mu_{max}=20.4\%$; (f) $\mu_{max}=26.0\%$; (g) $\mu_{max}=32.7\%$.



(a)



(b)

Fig. 28. (a) Local axial strain distribution at $\epsilon_{t0.5}$; (b) local axial strain distribution at ϵ_u .

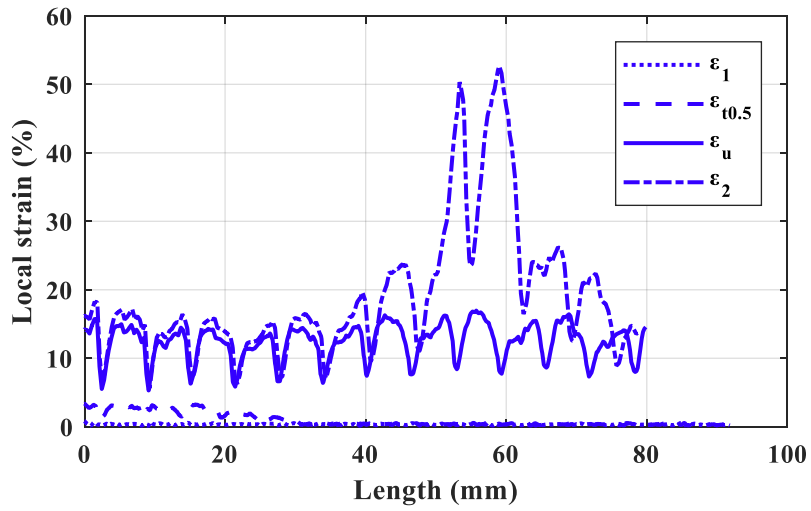


Fig. 29. Local axial strain distribution for an uncorroded bar at four different loading stages: ϵ_1 ($< \epsilon_{t0.5}$), $\epsilon_{t0.5}$, ϵ_u , ϵ_2 ($> \epsilon_u$).

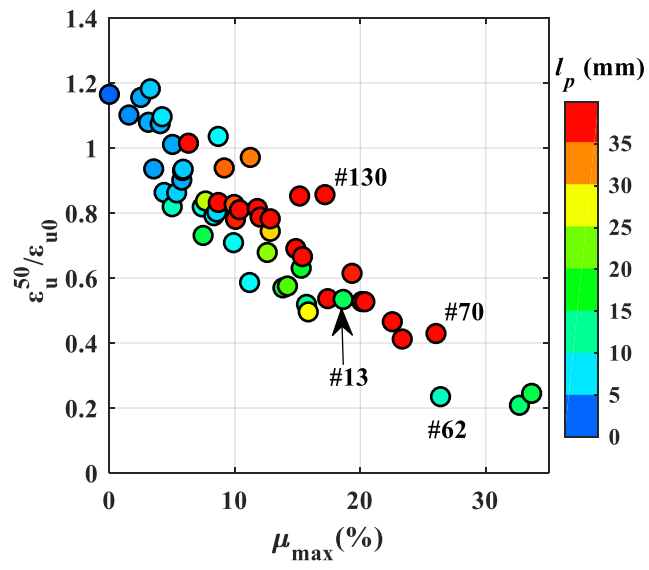


Fig. 30. Normalised ultimate strain ε_u^{50} versus maximum local corrosion level.

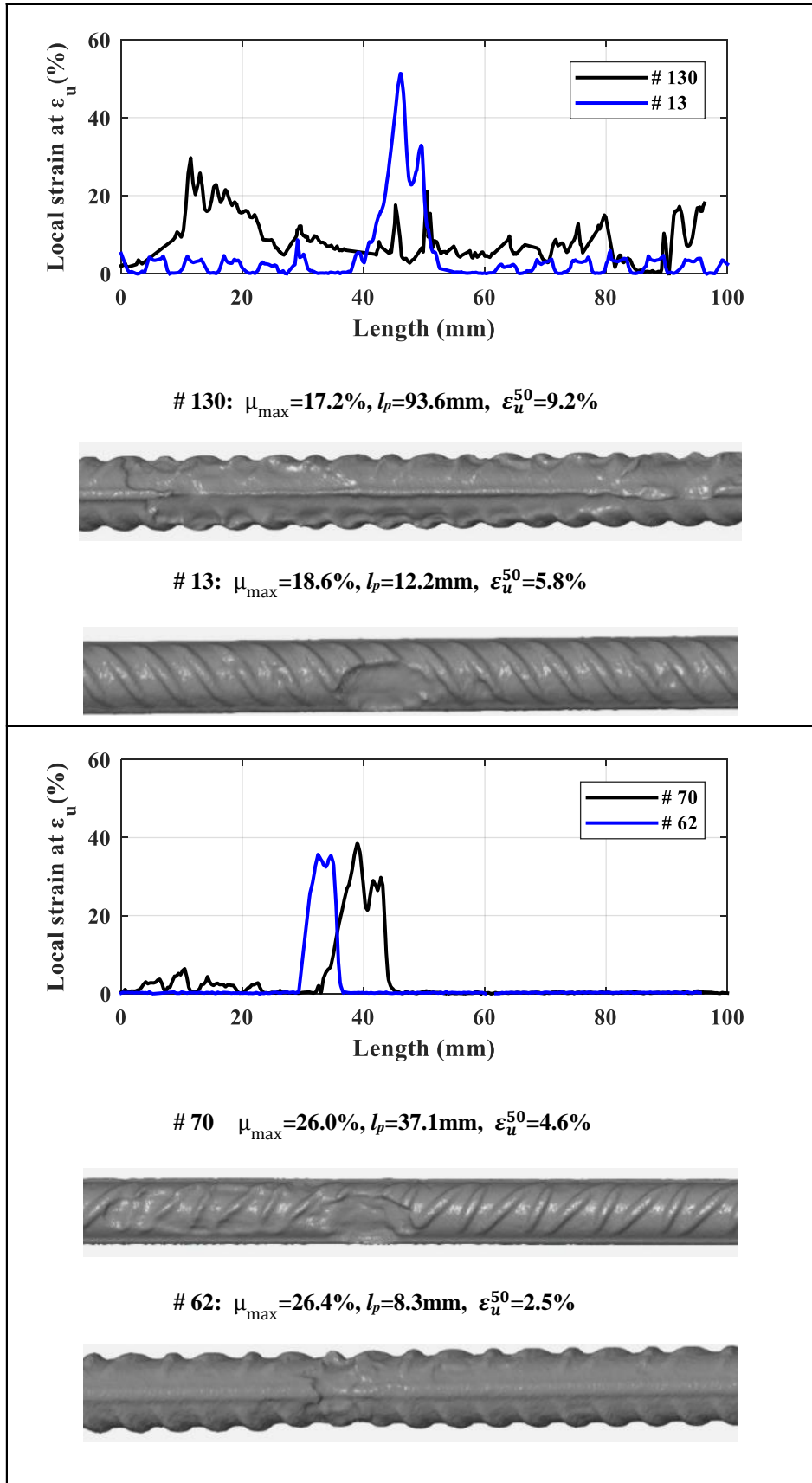


Fig. 31. Comparing local strain distribution under similar maximum local corrosion levels but with different pit lengths.

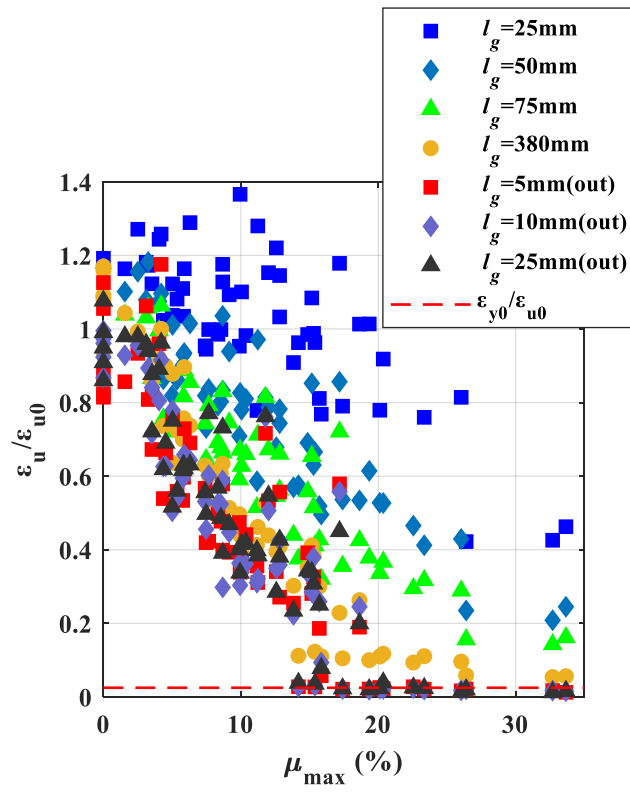


Fig. 32. Normalised ultimate strain from different extensometers versus maximum local corrosion level.

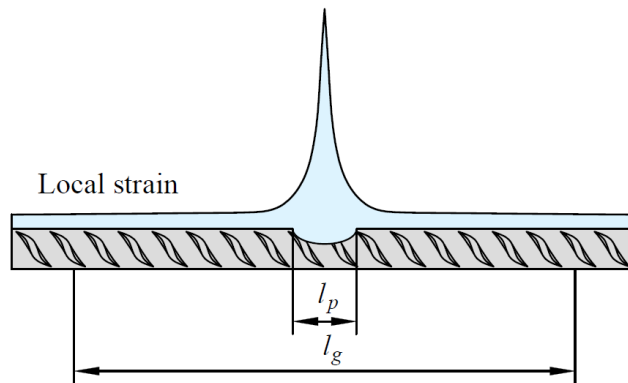


Fig. 33. Schematic diagram showing the bar with pit length l_p .

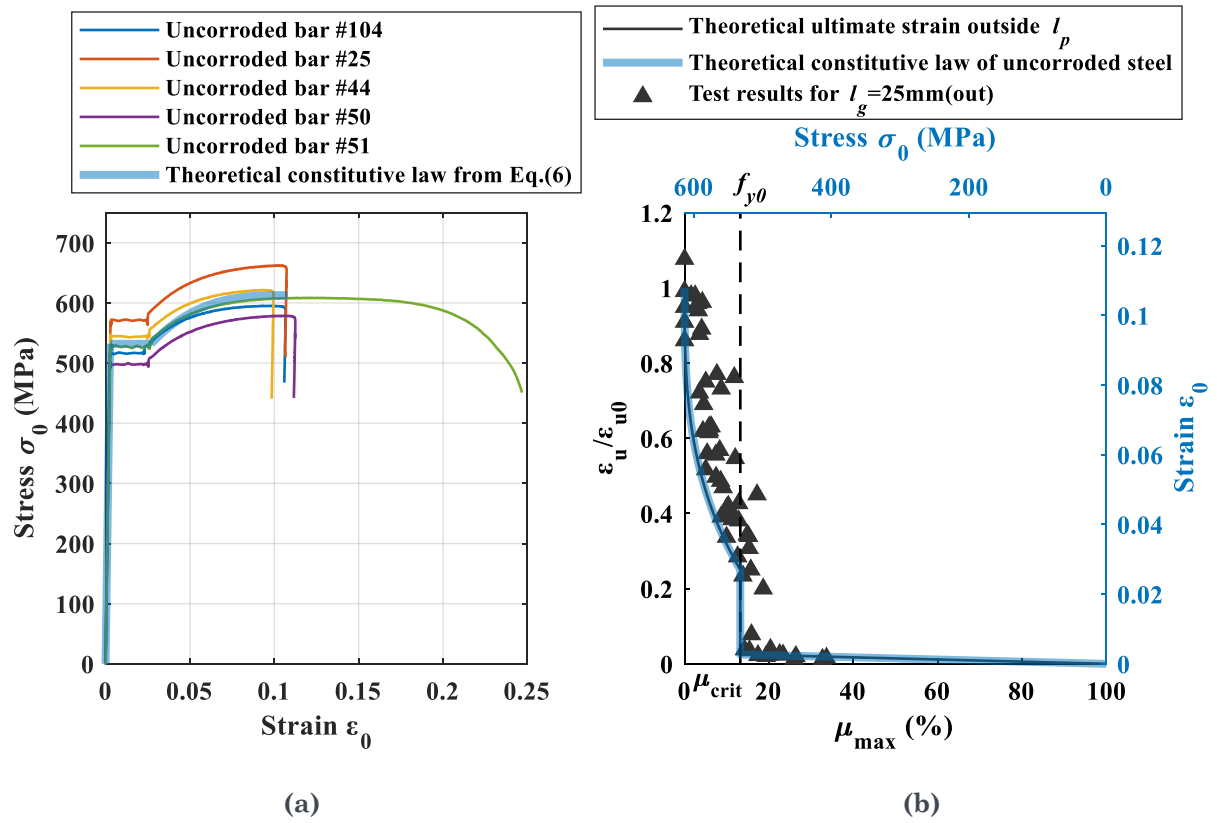


Fig. 34. (a) Stress-strain curves of uncorroded bars and theoretical constitutive law (n.b. the strain in four bars was unloaded because their failure zones were not captured in the DIC); (b) comparison of the theoretical relationship of $\epsilon_u^{out} - \mu_{max}$ and experimental results.

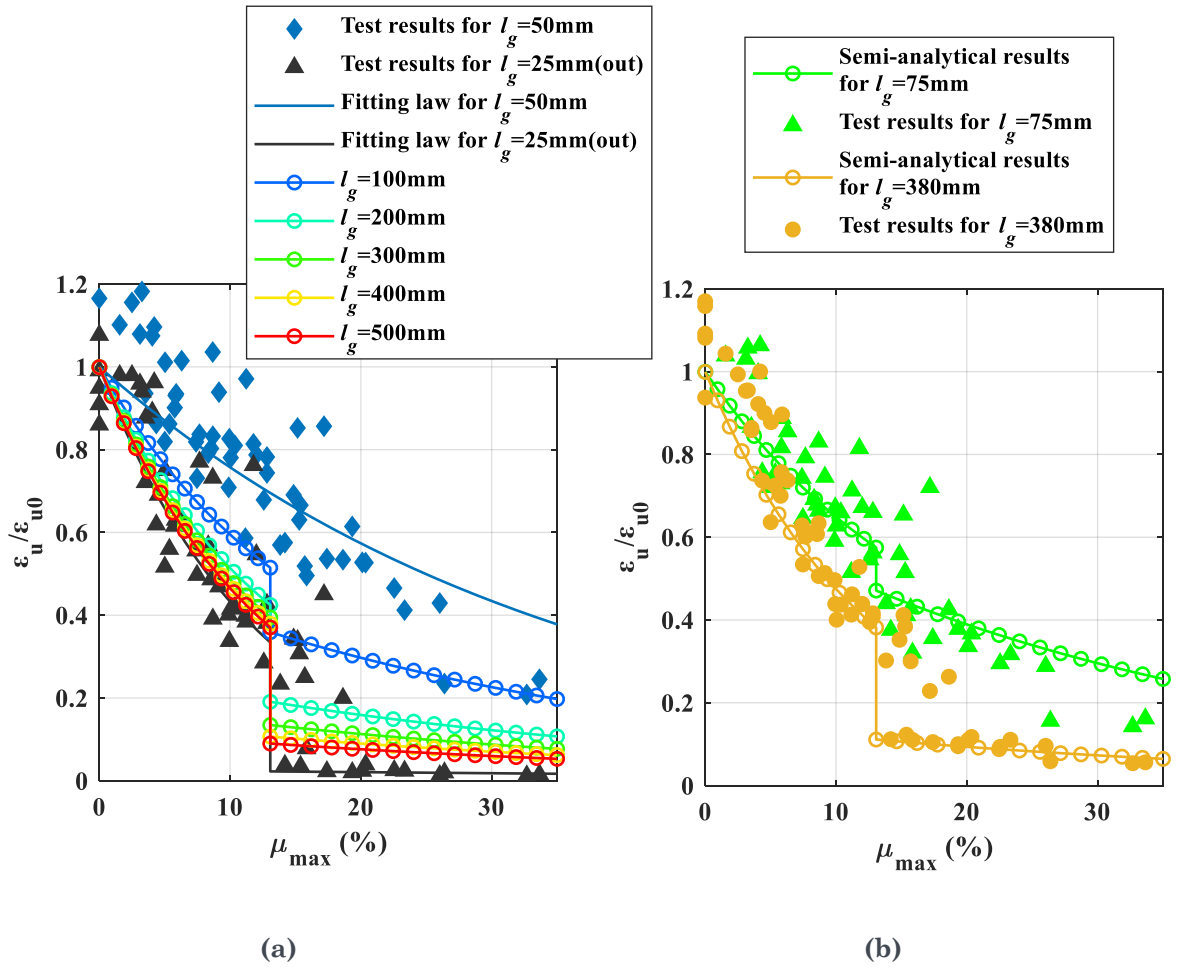


Fig. 35. (a) Ultimate strain for $l_g=50$ mm and $l_g=25$ mm(out) from experiments and fitting laws; ultimate strain at different gauge lengths obtained from the semi-analytical model; (b) comparison of the ultimate strain obtained from the semi-analytical model and experiments.

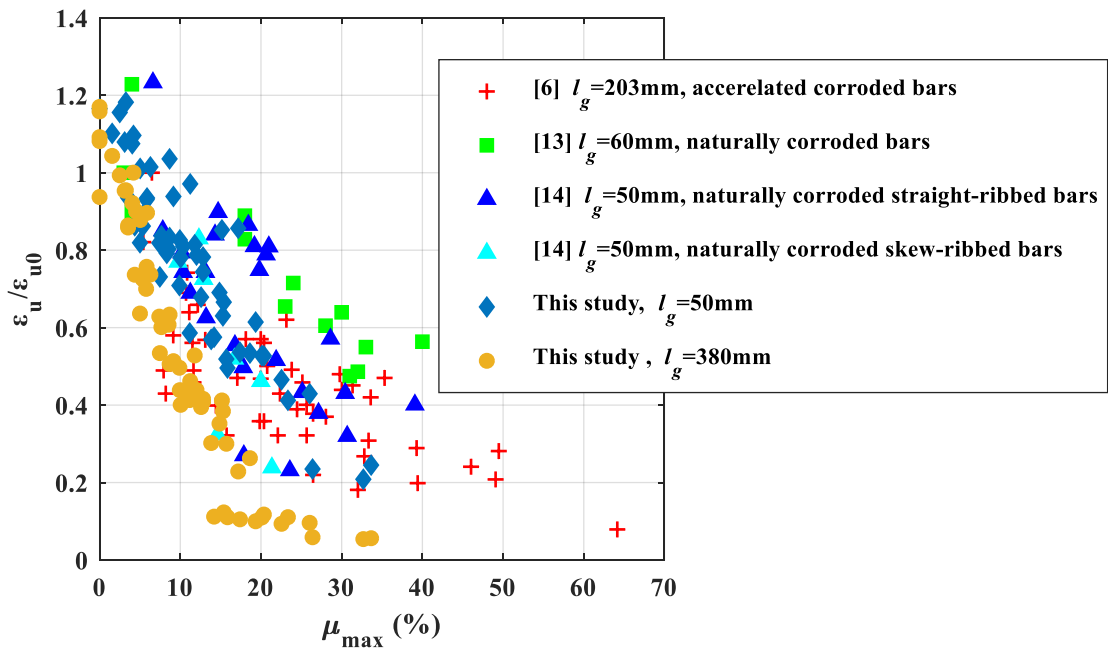


Fig. 36. Ultimate strain versus maximum local corrosion level from different studies.

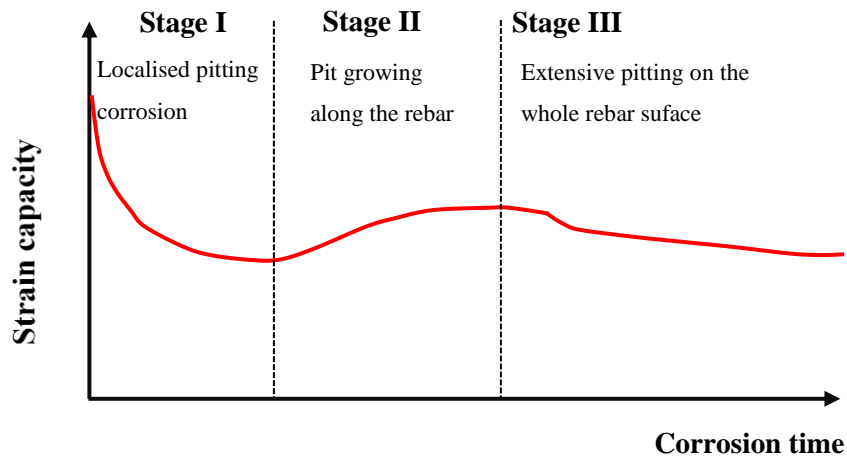


Fig. 37. Evolution of the strain capacity of corroded rebars as the pit morphology evolves with time.

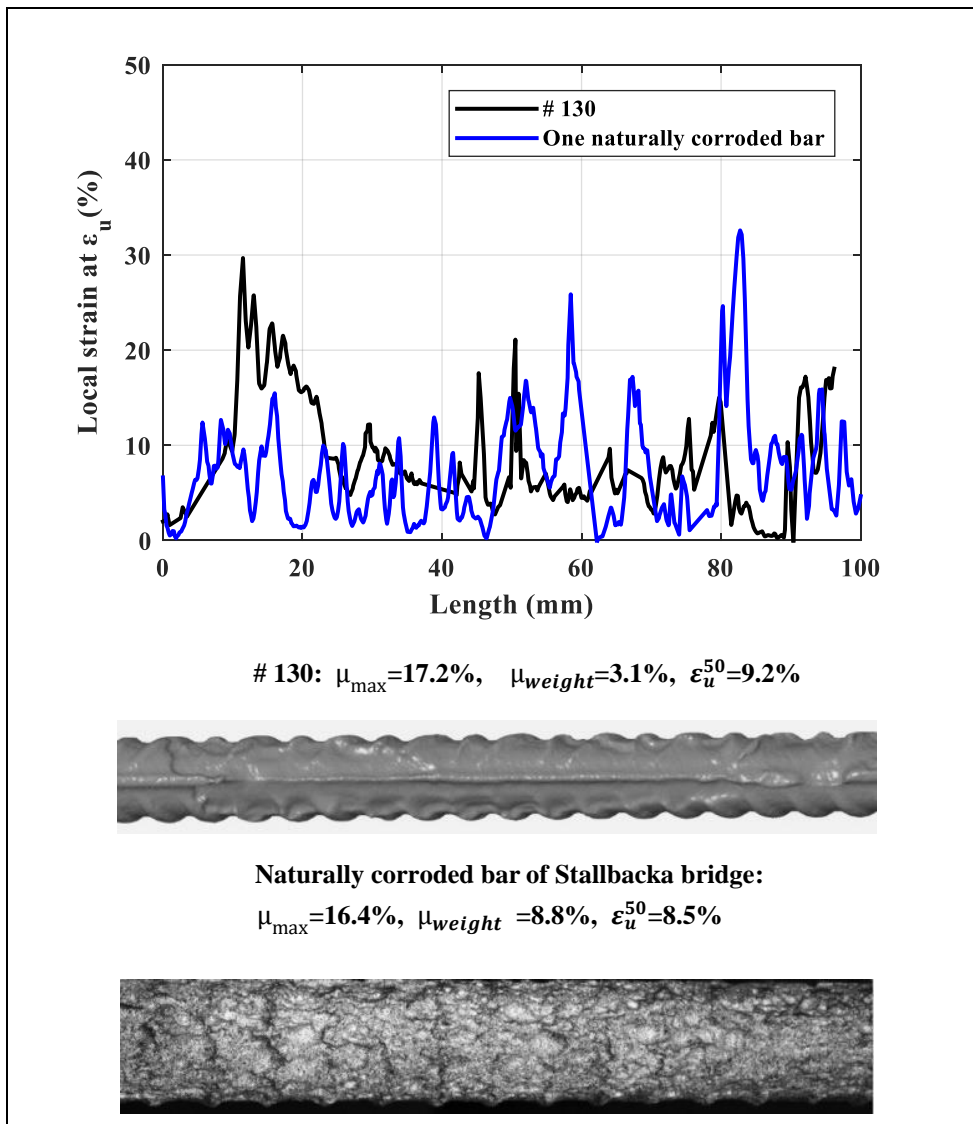


Fig. 38. Comparison of the local strain distribution of the bar with the greatest pit length in this study and a naturally corroded rebar in [14].

Table 4. Pit characteristics and ultimate strain.

bar No.	μ_{max} (%)	A_{min} (mm ²)	l_p (mm)	w_p (mm)	x_p (mm)	ε_u^{380} (%)	ε_u^{50} (%)
104	0.00	78.57	0.00	0.00	0.00	11.67	N/A
25	0.00	79.71	0.00	0.00	0.00	11.78	N/A
44	0.00	79.67	0.00	0.00	0.00	10.11	N/A
50	0.00	78.26	0.00	0.00	0.00	12.62	N/A
51	0.00	79.13	0.00	0.00	0.00	12.50	12.57
160	1.56	78.44	1.56	1.56	0.31	11.26	11.88
98	2.50	77.89	2.50	1.67	0.49	10.72	12.47
43	3.11	74.85	2.78	3.08	0.69	10.29	11.64
49	3.26	77.21	3.89	2.67	0.85	10.30	12.75
103	3.53	78.56	2.21	2.25	0.90	9.26	10.09
36	3.54	76.96	2.79	2.58	0.84	9.32	N/A
27	4.05	77.89	3.01	2.09	0.99	9.94	11.60
26	4.20	77.06	4.98	4.92	0.77	10.79	11.83
105	4.36	74.67	4.17	3.33	0.97	7.95	9.31
45	4.53	74.81	4.17	3.92	0.83	9.71	N/A
171	5.01	75.18	8.34	4.92	1.26	6.87	8.84
169	5.03	77.32	2.51	2.46	0.92	9.47	10.91
35	5.36	73.96	4.16	3.67	0.97	7.82	9.30
109	5.77	74.34	2.76	3.42	0.79	7.55	9.72
72	5.83	74.84	7.49	4.92	1.30	8.17	10.04
3	5.88	73.85	3.89	2.42	0.92	9.67	10.08
131	6.30	73.39	48.04	7.83	0.72	7.95	10.95
132	7.40	73.41	6.94	6.00	1.48	6.78	8.83
14	7.47	73.42	12.88	4.40	1.63	5.76	7.89
161	7.66	75.01	23.12	5.55	1.30	6.49	9.03
71	8.33	71.56	5.81	4.58	1.40	6.61	8.54
99	8.55	73.09	4.44	4.58	1.54	6.55	8.66
101	8.67	73.07	5.78	3.46	1.42	6.84	11.17
58	8.68	71.52	44.70	9.75	0.99	5.46	8.98
60	9.15	71.99	31.39	6.75	1.35	5.54	10.13
170	9.89	72.32	6.39	6.38	2.01	5.35	7.65
159	9.94	71.38	32.01	6.90	1.74	4.73	8.91
23	10.05	72.39	34.17	9.81	1.56	4.32	8.42
24	10.37	72.90	65.27	9.25	1.55	4.72	8.74
164	11.17	69.98	6.03	10.50	1.18	4.46	6.32
40	11.23	71.64	30.47	10.00	1.62	4.98	10.48
34	11.79	70.66	71.33	6.10	2.03	5.70	8.78
15	12.01	69.88	55.79	9.75	1.64	4.74	8.49
100	12.58	69.08	20.98	6.78	1.85	4.26	7.32
158	12.82	71.17	27.01	6.65	1.93	4.49	8.02
2	12.82	69.81	58.35	9.58	1.64	4.41	8.44
157	13.83	68.65	13.15	12.75	1.44	3.26	6.14

bar No.	μ_{max} (%)	A_{min} (mm ²)	l_p (mm)	w_p (mm)	x_p (mm)	ε_u^{380} (%)	ε_u^{50} (%)
22	14.19	69.29	18.60	12.88	2.12	1.21	6.21
162	14.86	68.67	45.03	10.42	1.59	3.80	7.45
1	15.16	66.74	36.65	12.55	1.53	4.44	9.19
165	15.29	69.27	14.33	7.81	2.11	4.14	6.80
163	15.39	68.39	42.49	13.37	1.70	1.33	7.18
110	15.71	66.13	10.00	8.42	2.07	3.24	5.60
42	15.85	65.89	25.32	15.49	1.66	1.19	5.35
130	17.18	65.93	93.58	12.55	1.69	2.47	9.24
174	17.40	65.73	39.75	9.47	3.42	1.13	5.79
13	18.63	62.72	12.22	8.42	2.65	2.84	5.76
111	19.34	62.57	34.16	13.67	1.82	1.08	6.63
67	20.11	63.20	46.12	13.85	2.35	1.19	5.69
68	20.36	61.43	62.79	9.00	2.70	1.27	5.69
97	22.55	61.35	40.26	13.00	2.60	1.01	5.02
172	23.34	61.90	43.13	8.20	3.08	1.19	4.45
70	26.03	58.95	51.43	11.25	3.36	1.04	4.63
62	26.39	57.23	8.33	23.92	1.77	0.63	2.53
61	32.68	51.85	11.39	16.17	2.30	0.58	2.25
63	33.65	51.84	12.78	21.67	2.26	0.61	2.64

Table 5. Tensile test results.

bar No.	L_0 (mm)	μ_{max} (%)	F_u (kN)	$F_{t0.5}$ (kN)	δ_u (mm)	ε_u^{380} (%)	ε_u^{25} (%)	ε_u^{50} (%)	ε_u^{75} (%)	$\varepsilon_u^{5_out}$ (%)	$\varepsilon_u^{10_out}$ (%)	$\varepsilon_u^{25_out}$ (%)
104	500	0.00	46.76	40.42	44.34	11.67	N/A	N/A	N/A	12.15	10.74	9.81
25	500	0.00	52.02	44.94	44.76	11.78	N/A	N/A	N/A	8.79	10.37	10.24
44	500	0.00	48.82	42.79	38.42	10.11	N/A	N/A	N/A	8.89	9.36	9.28
50	500	0.00	45.45	39.06	47.96	12.62	N/A	N/A	N/A	9.46	9.96	10.69
51	500	0.00	47.80	41.57	47.49	12.50	12.86	12.57	N/A	11.39	10.50	11.61
160	500	1.56	46.88	40.10	42.77	11.26	12.55	11.88	11.20	9.24	10.02	10.57
98	500	2.50	50.53	43.33	40.72	10.72	13.71	12.47	N/A	10.07	10.31	10.57
43	500	3.11	48.27	40.19	39.09	10.29	12.74	11.64	11.12	11.46	10.27	10.34
49	500	3.26	47.30	40.79	39.14	10.30	12.65	12.75	11.41	8.72	9.64	10.14
103	500	3.53	47.85	40.09	35.19	9.26	12.11	10.09	9.34	7.25	7.72	7.78
36	500	3.54	47.84	41.22	35.41	9.32	N/A	N/A	N/A	8.83	9.07	9.46
27	500	4.05	48.72	40.53	37.78	9.94	13.42	11.60	10.74	10.36	8.69	9.61
26	500	4.20	47.44	40.86	41.00	10.79	13.57	11.83	11.47	12.68	9.88	10.38
105	500	4.36	46.96	39.72	30.20	7.95	11.04	9.31	8.15	5.82	6.76	6.67
45	500	4.53	48.43	41.41	36.90	9.71	N/A	N/A	N/A	7.15	6.77	7.45
171	500	5.01	47.02	39.16	26.09	6.87	11.19	8.84	7.77	5.81	5.44	5.57
169	500	5.03	49.47	42.65	35.99	9.47	12.11	10.91	N/A	8.23	8.41	8.09
35	500	5.36	46.02	38.66	29.72	7.82	11.66	9.30	8.13	6.03	5.85	6.04
109	500	5.77	47.13	38.71	28.70	7.55	11.97	9.72	7.87	5.76	6.41	6.64
72	500	5.83	47.97	39.68	31.04	8.17	11.16	10.04	8.81	6.44	6.51	6.80
3	500	5.88	48.52	40.38	36.75	9.67	12.55	10.08	9.57	7.86	7.10	6.70
131	500	6.30	46.85	38.64	30.22	7.95	13.91	10.95	9.23	7.45	6.94	6.81
132	500	7.40	46.55	38.78	25.76	6.78	10.29	8.83	8.01	6.12	5.73	6.00
14	500	7.47	46.39	38.94	21.90	5.76	10.19	7.89	6.96	4.52	4.92	5.36
161	500	7.66	46.12	38.20	24.65	6.49	10.77	9.03	8.55	4.57	6.50	8.31
71	500	8.33	47.72	39.41	25.11	6.61	10.63	8.54	7.46	5.37	5.67	6.13

bar No.	L_0 (mm)	μ_{max} (%)	F_u (kN)	$F_{t0.5}$ (kN)	δ_u (mm)	ϵ_u^{380} (%)	ϵ_u^{25} (%)	ϵ_u^{50} (%)	ϵ_u^{75} (%)	$\epsilon_u^{5_{out}}$ (%)	$\epsilon_u^{10_{out}}$ (%)	$\epsilon_u^{25_{out}}$ (%)
99	500	8.55	45.83	38.16	24.91	6.55	10.77	8.66	7.32	5.15	5.65	5.24
101	500	8.67	46.55	39.52	25.98	6.84	12.68	11.17	8.96	6.24	6.35	7.89
58	500	8.68	44.26	36.63	20.75	5.46	12.17	8.98	7.16	4.30	3.21	4.22
60	500	9.15	43.73	35.99	21.05	5.54	11.79	10.13	8.04	4.24	4.82	5.06
170	500	9.89	47.17	39.14	20.35	5.35	10.28	7.65	6.37	5.11	3.92	4.32
159	500	9.94	45.65	37.87	17.98	4.73	14.74	8.91	7.24	3.65	3.27	3.64
23	500	10.05	44.42	36.85	16.43	4.32	11.87	8.42	6.77	3.97	3.66	4.48
24	500	10.37	45.55	37.55	17.92	4.72	10.59	8.74	7.12	4.76	3.90	4.53
164	500	11.17	44.64	37.60	16.93	4.46	8.40	6.32	5.56	3.84	3.35	4.29
40	500	11.23	45.54	37.06	18.94	4.98	13.81	10.48	7.68	3.36	3.47	4.14
34	500	11.79	47.07	39.05	21.65	5.70	8.58	8.78	8.79	7.73	8.20	8.22
15	500	12.01	44.38	35.89	18.00	4.74	12.44	8.49	7.25	5.75	5.47	5.90
100	500	12.58	44.33	36.69	16.19	4.26	13.16	7.32	5.89	3.68	3.77	3.08
158	500	12.82	46.23	36.72	17.06	4.49	11.14	8.02	6.07	2.93	3.87	4.11
2	500	12.82	43.94	36.40	16.75	4.41	12.35	8.44	7.13	6.01	4.59	4.60
157	500	13.83	42.43	35.19	12.38	3.26	9.80	6.14	4.75	2.75	2.41	2.53
22	500	14.19	41.99	33.93	4.59	1.21	10.39	6.21	4.05	0.30	0.30	0.41
162	500	14.86	43.93	35.62	14.44	3.80	10.63	7.45	6.02	4.23	3.64	3.70
1	500	15.16	43.47	34.72	16.89	4.44	11.70	9.19	7.06	3.03	3.08	3.66
165	500	15.29	44.61	35.68	15.75	4.14	10.66	6.80	5.56	3.52	4.09	3.32
163	500	15.39	43.22	35.22	5.04	1.33	10.39	7.18	4.43	0.29	0.33	0.38
110	500	15.71	39.99	31.55	12.30	3.24	8.75	5.60	4.62	2.01	2.80	2.70
42	550	15.85	40.51	32.54	5.12	1.19	8.29	5.35	3.46	0.63	1.01	0.84
130	500	17.18	42.48	32.43	9.37	2.47	12.71	9.24	7.77	6.25	6.02	4.86
174	550	17.40	40.38	31.56	4.87	1.13	8.52	5.79	3.84	0.23	0.23	0.24
13	500	18.63	41.70	33.59	10.78	2.84	10.93	5.76	4.59	2.05	2.64	2.15
111	500	19.34	36.81	28.38	4.10	1.08	10.94	6.63	4.08	0.23	0.21	0.22

bar No.	L_0 (mm)	μ_{max} (%)	F_u (kN)	$F_{t0.5}$ (kN)	δ_u (mm)	ϵ_u^{380} (%)	ϵ_u^{25} (%)	ϵ_u^{50} (%)	ϵ_u^{75} (%)	$\epsilon_u^{5_out}$ (%)	$\epsilon_u^{10_out}$ (%)	$\epsilon_u^{25_out}$ (%)
67	500	20.11	38.88	30.32	4.51	1.19	8.40	5.69	3.63	0.28	0.24	0.25
68	500	20.36	39.90	30.33	4.81	1.27	9.91	5.69	3.96	0.24	0.24	0.42
97	500	22.55	40.59	32.90	3.83	1.01	N/A	5.02	3.18	0.30	0.26	0.27
172	500	23.34	40.34	32.28	4.54	1.19	8.20	4.45	3.42	0.23	0.22	0.26
70	500	26.03	40.33	30.83	3.94	1.04	8.78	4.63	3.11	0.18	0.19	0.14
62	500	26.39	37.25	34.10	2.41	0.63	4.55	2.53	1.68	0.23	0.23	0.21
61	500	32.68	32.50	28.55	2.21	0.58	4.59	2.25	1.54	0.19	0.18	0.13
63	500	33.65	33.59	29.28	2.31	0.61	4.99	2.64	1.75	0.14	0.17	0.17

N.b. L_0 is the bar length, δ_u is the total displacement at the ultimate force. For the bars in which the failure zone was not captured by the DIC or the reference length moved outside the DIC measuring volume, some values of the ultimate strain were not available.

Nomenclature

A	cross-sectional area of a steel bar
A_{min}	minimum cross-sectional area along a bar
$A_{0,min}$	original area of the cross-section with the minimum remaining area
A_0	nominal cross-sectional area of uncorroded bars
E_0	Young's modulus of uncorroded bars
P	strain-hardening power of uncorroded bars
E_{sh0}	strain-hardening modulus of uncorroded bars, i.e. tangent slope at ε_{sh0}
F	tensile force
F_{corr}	proof or ultimate force of corroded bars, either $F_{t0.5}$ or F_u
F_0	yield or ultimate force of uncorroded bars, either F_{y0} or F_{u0}
$F_{t0.5}$	proof force, defined as the force at $\varepsilon_{t0.5}$ based on 50 mm extensometer
F_u	ultimate force
F_y	yield force
L_0	bar length
$f_{t0.5}$	proof strength, defined as the stress at $\varepsilon_{t0.5}$ based on 50 mm extensometer
f_u	ultimate strength
f_{u0}	ultimate strength of uncorroded bars
f_y	yield strength
f_{y0}	yield strength of uncorroded bars
l_g	extensometer gauge length
l_p	pit length
w_p	pit width at the minimum cross-section
x_p	pit depth at the minimum cross-section
ε_{sh0}	strain at the onset of hardening of uncorroded bars
$\varepsilon_{t0.5}$	proof strain when the total extension is 0.5%, based on the 50 mm extensometer
ε_u	ultimate strain, defined as the strain at the ultimate force

ε_{u0}	ultimate strain of uncorroded bars
$\varepsilon_u(x)$	local strain at ultimate strain at x position
ε_{y0}	strain at the onset of yielding of uncorroded bars
ε^{25}	strain measured from 25 mm extensometer across the failure zone
ε^{50}	strain measured from 50 mm extensometer across the failure zone
ε^{75}	strain measured from 75 mm extensometer across the failure zone
$\varepsilon^{5.out}$	strain measured from 5mm extensometer outside the failure zone
$\varepsilon^{10.out}$	strain measured from 10 mm extensometer outside the failure zone
$\varepsilon^{25.out}$	strain measured from 25 mm extensometer outside the failure zone
ε^{380}	strain measured from the total elongation of tested bars
ε_u^{25}	ultimate strain measured from 25 mm extensometer across the failure zone
ε_u^{50}	ultimate strain measured from 50 mm extensometer across the failure zone
ε_u^{75}	ultimate strain measured from 75 mm extensometer across the failure zone
$\varepsilon_u^{5.out}$	ultimate strain measured from 5 mm extensometer outside the failure zone
$\varepsilon_u^{10.out}$	ultimate strain measured from 10 mm extensometer outside the failure zone
$\varepsilon_u^{25.out}$	ultimate strain measured from 25 mm extensometer outside the failure zone
ε_u^{380}	ultimate strain measured from the total elongation of tested bars
$\varepsilon_u^{l_g}$	ultimate strain over the gauge length l_g
ε_u^{out}	ultimate strain outside the pit over any gauge length greater than one rib spacing
α	empirical coefficient to indicate the degradation rate of the force with μ_{max}
σ	tensile stress in steel bars, which is calculated based on A_{min}
δ_u	total displacement at the ultimate force
μ_{weight}	corrosion level from the weight loss method
μ	corrosion level
μ_{max}	maximum local corrosion level along a bar, defined as the maximum cross-sectional area loss percentage
μ_{crit}	critical local corrosion level, above which no yielding occurs outside the pit

Chen E., Berrocal, C. G., Löfgren I., & Lundgren K.: Comparison of the service life, life-cycle costs and assessment of hybrid and traditional reinforced concrete through a case study of bridge edge beams in Sweden. *Structure and Infrastructure Engineering* 2021.

Comparison of the service life, life-cycle costs and assessment of hybrid and traditional reinforced concrete through a case study of bridge edge beams in Sweden

E Chen^a, Carlos G. Berrocal^{a,b*}, Ingemar Löfgren^{a,b} and Karin Lundgren^a

^aDivision of Structural Engineering, Chalmers University of Technology, Göteborg, 412 96, Sweden;

^bThomas Concrete Group AB, 402 26 Göteborg, Sweden

*corresponding author: carlos.gil@chalmers.se

Comparison of the service life, life-cycle costs and assessment of hybrid and traditional reinforced concrete through a case study of bridge edge beams in Sweden

The edge beams of reinforced concrete bridges with de-icing salts sprayed experience extensive corrosion damage. The average service life of edge beams needing replacement in Sweden has been reported as only 45 years, causing great economic loss to both owners and users. Hence, finding a durable solution for edge beams would benefit society. Hybrid reinforced concrete structures, produced by adding a low-to-moderate fibre content into traditional reinforced concrete, can effectively limit the service crack width and improve resistance to chloride-induced corrosion damage. In this paper, different alternatives of hybrid and traditional reinforced edge beams were designed for a case study. The service life of the alternatives was compared by conducting chloride diffusion calculations and by applying a corrosion-induced cracking model. The economic and environmental (indicated by greenhouse gas emissions) benefits of using hybrid reinforced edge beams were assessed by life-cycle cost analysis and life-cycle assessment. The results showed that the service life of edge beams made of hybrid reinforced concrete can be prolonged by over 58%, thereby enabling a significant reduction in the total life-cycle costs and annual total greenhouse gas emissions.

Keywords: hybrid reinforced concrete; reinforcement corrosion; service life; life-cycle cost analysis; life-cycle assessment

1. INTRODUCTION

Civil infrastructures play a vital part in the social and economic development of a society and structures of greater importance should be designed to have a service life of over 100 years (International Federation for Structural Concrete, 2010). During their lifespan, structures may experience various types of deterioration due to environmental actions. In chloride environments, such as coastlines and regions where de-icing salt is sprayed on roads, the major deterioration mechanism of reinforced concrete (RC) structures is the corrosion of reinforcing steel, since chloride ions can destroy the passive film on the steel surface. The damage caused by reinforcement corrosion (cover cracking/spalling, bond degradation, and reduction in rebar cross-

section) poses a major threat to the durability and safety of RC structures, thus shortening their service life.

Maintaining the function of existing structures under deterioration requires measures which include maintenance, repair and rehabilitation (MR&R). This gives rise to a great amount of MR&R costs during the structures' service life. A comprehensive survey in 2002 (Koch et al.), reported that the annual direct cost of corrosion on infrastructure in the United States was estimated at \$22.6 billion. The user costs caused by traffic disruption during maintenance work may even take the major part of the total costs and be higher than the cost of MR&R (Thoft-Christensen, 2012). It is therefore of great importance to the whole society to consider the total costs of an infrastructure project. Life-cycle cost analysis (LCCA) is a technique which enables accounting the costs incurred 'from cradle to grave' and is becoming an important infrastructure management tool (Salokangas, 2013).

To improve the durability and extend the service life of infrastructure such as bridges, a variety of new materials and innovative structural solutions have been developed attempting to partially replace or compensate the traditional reinforced concrete (traditional RC) structures. LCCA has been applied in recent years to evaluate the economic performance of different design solutions or maintenance strategies (Safi et al., 2013; Veganzones Muñoz et al., 2016). In addition to the economic costs, environmental impact is another important factor of concern when evaluating alternative solutions; it is imperative nowadays to combat climate change and realise sustainable development (Niu & Fink, 2018; Penadés-Plà et al., 2017). Life-cycle assessment (LCA) is one such approach to quantifying the environmental impact of a project throughout its life cycle.

Bridge edge beams are structural elements known to suffer from extensive reinforcement corrosion damage due to the frequent use of de-icing salt. According to a previous survey of bridges in Sweden (Mattsson et al., 2007), the average age of 135 edge beams which needed

replacement was only 45 years, with a standard deviation of 11 years. This is much shorter than the design life of most bridges. Another study (Racutanu, 2001) analysed the inspection reports on 353 bridges in Sweden. The edge beams were found to be the most damaged part of a bridge; 21% of damage was associated with edge beams. According to the Swedish Transport Administration, the cost arising from repair or replacement of a bridge's edge beam system (mostly the edge beams and railing) may account for as much as 60% of the overall cost of the entire bridge during its lifespan, as stated in a recent study by Veganzones Muñoz et al. (2016). To discover cost-effective solutions for edge beams, recent studies have proposed different alternative designs to the traditional RC edge beam, including concrete edge beams reinforced with stainless steel, or removal of edge beams from bridge structures (Veganzones Muñoz, 2016; Veganzones Muñoz et al., 2016).

Adding fibres to traditional RC edge beams to create hybrid reinforced concrete (hybrid RC) edge beams, is another possible solution to the traditional choice. Since fibre reinforced concrete (FRC) can achieve better crack control, it is a promising material for alleviating the detrimental effects of concrete cracks and thus achieving prolonged service life. Hybrid RC members can reduce crack width under mechanical loading and restraint forces (Al-Kamyani et al., 2019; Berrocal & Löfgren, 2018; Vandewalle, 2000). They also exhibit better durability in chloride environments than traditional RC members. It was shown (Berrocal et al., 2015) that the corrosion initiation time in hybrid RC beams was delayed compared to traditional RC beams, even though the maximum width of surface cracks generated under bending was the same; the more tortuous internal crack morphology and reduced interface damage in hybrid RC beams was deemed beneficial in terms of resisting chloride penetration. A recent investigation found the chloride diffusion coefficient to be reduced by 30-38% in steel fibre reinforced concrete beams compared to plain concrete ones, when the maximum bending stress in each specimen type was half the ultimate strength (Wang et al., 2018). Other studies have also shown that adding fibres may

significantly reduce corrosion-induced cover cracking, prevent cover spalling (Z. Chen & Yang, 2019; Sadrinejad et al., 2018) and improve the residual post-peak bond capacity of corroded specimens (Berrocal et al., 2017), as compared to reinforced mortar or concrete specimens without fibres. Moreover, the residual flexural capacity and ductility of corroded hybrid RC beams were higher than those of traditional RC beams after the same period of rebar corrosion (Berrocal et al., 2018).

Although hybrid RC has better structural performance and improved cracking resistance compared to traditional RC, structure owners are still reluctant to use hybrid RC due to lack of long-term experience. Due to time constraints, most positive findings regarding rebar corrosion in FRC have been based on short-term laboratory investigations, including natural corrosion tests (Berrocal et al., 2015; Blunt et al., 2015) and accelerated corrosion tests with impressed current (Z. Chen & Yang, 2019; Sadrinejad et al., 2018). Moreover, the extra cost of fibres raises a concern that the investment costs of hybrid RC structures may be higher. On the other hand, hybrid RC members are expected to have a longer service life. The MR&R costs and user costs over the whole service life of the infrastructure may thus be reduced. However, the authors found very limited information in the literature regarding the comparison of life-cycle costs (LCC) for hybrid RC and traditional RC applications.

To quantify the benefits of using hybrid RC for structures in chloride environments, this study carried out service life prediction, LCCA and LCA for hybrid and traditional reinforced concrete. This involved a case study of a bridge edge beam, with multiple parameters chosen by carefully considering field data and experimental results from previous studies. The service life of hybrid RC and traditional RC edge beam were predicted via a chloride diffusion analysis and finite element modelling of the corrosion-induced cracking process. The predicted service life guided the replacement time for the edge beam. The other input parameters in the LCCA and LCA were

selected by referring to the literature and available databases. Finally, the influence of several main parameters was examined in a sensitivity analysis.

2. OVERVIEW OF THE CASE STUDY

2.1 Traditional RC edge beam

The edge beam is a structural member located at the sides of the bridge deck, see Figure 1. Its main functions are to support the railing and prevent cars or bridge users from driving or falling off and to accommodate the drainage system. It may also provide stiffness to the bridge deck, helping to distribute concentrated loads. The most common type of edge beam used in Sweden is made of reinforced concrete and integrated into the bridge deck (Veganzones Muñoz et al., 2016). Pre-fabricated edge beams are also sometimes used. According to the design rules of the Swedish Transport Administration (Trafikverket, 2011), the edge beam must be designed with sufficient load-bearing capacity for the railing attachment and its cross-sectional dimension should be at least 400×400 mm. Moreover, it is specified (Trafikverket, 2011) that the edge beam should have a longitudinal reinforcement of at least $7\text{Ø}16$ and a transverse reinforcement of at least $\text{Ø}10$ s 300 mm. Figure 2 shows a cross-sectional sketch of the edge beam, with the top surface inclined towards the bridge deck.

The exposure condition of road bridges with de-icing salt sprayed in winter corresponds to class XD3 in the standard BS EN 206:2013 (British Standards Institution, 2013). The allowable crack width for class XD3 should be limited to 0.3 mm (European Committee for Standardization, 2004). According to Swedish national requirements (Boverket, 2019), the allowable crack width in XD3 is even stricter: 0.15 mm for a design life of 100 years, and 0.20 mm for a design life of 50 years. One of the main causes of cracking in edge beams is shrinkage, see the restraint-induced cracks in Figure 1. Restraint forces arise when edge beams are cast after the bridge deck in a new bridge, or when new edge beams are substituted for the demolished ones. Pre-existing cracks can accelerate the ingress of undesirable substances (such as chloride ions, moisture and oxygen),

causing early corrosion in the cracked region. Alongside chloride-induced steel corrosion, frost attack and carbonation are the other two major deterioration mechanisms in edge beams (Mattsson et al., 2007). Nevertheless, only chloride-induced corrosion was considered in this study as this is the main cause of degradation.

2.2 Methodology of the case study

The steps of the case study are outlined in Figure 3. First, the alternative designs of hybrid RC and traditional RC edge beams were performed. The flexural moment capacity and restraint-induced crack width governed the quantity of steel rebars and fibres. A basic design of the traditional RC edge beam was chosen to satisfy the minimum requirements given in the regulations (Trafikverket, 2011). The flexural moment capacity of other alternative designs was checked to ensure it was adequate relative to the basic design. However, a detailed design for the necessary moment capacity to resist impact loading on the railing was beyond the scope of this study.

The second step involved predicting the service life of each design, which is a critical input parameter for LCCA and LCA. Although many service life models for RC structures deteriorated by steel corrosion have been proposed in research studies from the literature (cf. François et al., 2018; Weyers, 1998), they are still far from direct practical applicability due to the complex environmental conditions and load actions, probabilistic nature of material properties and so on. Rather, service life data grounded in experience has often been used in LCCA (Salokangas, 2013). As for the service life of hybrid RC structures, to the authors' knowledge, no such field data is currently available. Therefore, a service life model for the edge beam was established in this study. Moreover, the input parameters used in the service life model were calibrated by comparing predicted service life of the traditional RC edge beam with field data.

There then followed a comparative LCCA and LCA of the hybrid RC and traditional RC edge beam. The inventory of LCCA and LCA was defined and only items relating to the edge beam were considered. The necessary information and input parameters were collected from the

literature and databases. A sensitivity analysis was conducted as some parameters might display a large scatter in values.

3. ALTERNATIVE DESIGNS IN THE CASE STUDY

The edge beam considered in the case study had a length of 15 m and a cross-section of 450×450 mm. C40 grade concrete defined in Model Code 2010 (International Federation for Structural Concrete, 2010) was used. The parameters defining the concrete properties were calculated from the code. The total shrinkage strain was set as $600 \mu\epsilon$ and the restraint degree assumed to be 0.4. The characteristic yield strength of the steel was 500 MPa. The material parameters required in the restraint crack model are given in Table 1. The same concrete grade and same mechanical parameters of steel were used in the traditional and hybrid RC designs. The additional parameter in the hybrid RC designs, residual tensile strength of FRC, $f_{t,res}$ (which is dependent on the fibre content, fibre type and geometry), will be chosen in Section 3.2.

3.1 Analytical modelling of restraint-induced cracking

In the design codes, the width of cracks caused by external loading is usually controlled by designing a minimum reinforcement and limiting the stress in the reinforcement steel. In restrained concrete members subjected to shrinkage or thermal contraction, the calculation of crack width cannot be conducted in the same manner since the restraint force, which depends on the stiffness of the member, is not known a priori. An iterative procedure is needed to determine the number of cracks and their width.

Engström (2007) developed a model to calculate restraint crack width by taking into account the bond-slip behaviour between the reinforcement bar and the concrete. In the model, cracks are modelled as non-linear springs, as illustrated in Figure 4. At a cracked section in the traditional RC element, all the force is carried by the reinforcement, whereas the concrete is assumed to be stress-free. The model was extended by Löfgren (2007) to include the effect of fibre

reinforcement by introducing the residual tensile strength of FRC, see Figure 4. Berrocal and Löfgren (2018) further modified the model. In their work, the bond-slip relationship given in CEB 228 (Comite Euro-international du beton, 1995) was replaced by the one suggested in Model Code 2010 (International Federation for Structural Concrete, 2010) and a linear relationship of the debonding length adjacent to the crack due to radial cracking and the steel stress was considered. The equations to calculate the restraint-induced crack width are given in the Supplementary 1.

To design the quantity of steel rebars and fibres, the influence of residual tensile strength of FRC (expressed as a fraction of the tensile strength, i.e. $\alpha_f f_{ctm}$) and the reinforcement ratio ρ on the predicted maximum and mean crack width ($w_{cs, max}$ and $w_{cs, mean}$) was first examined for the edge beam with rebar diameter of 16 mm. From the results shown in Figure 5, the crack width is reduced with increasing reinforcement ratio and increasing residual tensile strength. In addition, the decreasing rate of crack width becomes slower as the quantity of rebar increases. To achieve a similar crack width in the hybrid RC edge beam, the required reinforcement ratio decreases as the residual tensile strength increases.

3.2 Reinforcement design

Six reinforcement designs using the same concrete grade C40 were chosen for the case study: two for the traditional RC edge beams (PL1 and PL2, where ‘PL’ denotes ‘plain concrete’) and four for the hybrid RC edge beams (FRC1, FRC2, FRC3 and FRC4), as listed in Table 2. All the designs had the same geometry and same stirrup arrangement ($\text{Ø}10$ s 300 mm). In all designs, the clear cover thickness was 45 mm. The basic design, PL1, was reinforced with 10 $\text{Ø}16$ longitudinal steel rebars. In PL2, 16 $\text{Ø}16$ longitudinal rebars were used to bring the shrinkage crack width below 0.3 mm. Since the reinforcement layout may influence the corrosion-induced crack pattern and crack width under the same amount of reinforcement, two different reinforcement layouts were considered for PL2: bundled rebars at the corners and middle height (PL2-I) and uniformly distributed bars in the top and bottom layers (PL2-II).

Steel fibres were used in the design of hybrid RC edge beams. Two volume fractions of fibres were considered: 0.5% vol. fibres for FRC1 and FRC2 and 1.0% vol. fibres for FRC3 and FRC4. The material parameters of the FRC were determined according to previous studies (Berrocal et al., 2018; Jepsen et al., 2018; Löfgren et al., 2005) which investigated the mechanical properties of FRC with 0.5% vol. and 1.0% vol. Dramix© (65/35) steel fibres and a water/cement ratio of 0.47 (comparable to C40 grade concrete). The two experimental studies (Berrocal et al., 2018; Löfgren et al., 2005) reported the load-crack mouth opening displacement (CMOD) curves of the FRC obtained from the three-point bending test on notched beams. The tensile stress-crack opening relationship of the FRC was derived inversely (Jepsen et al., 2018) by analysing the flexural load-CMOD results. It was shown (Berrocal et al., 2018) that the tensile strength of FRC with 0.5% vol. steel fibres was similar to that of plain concrete with a similar mix composition, while the tensile strength of FRC with 1.0% vol. steel fibres was slightly greater than that of FRC with 0.5% vol. steel fibres (Jepsen et al., 2018).

Accordingly, in the case study, the tensile strength of FRC with 0.5% and 1.0% vol. steel fibres was taken as 3.5 and 3.6 MPa respectively, see Table 2. It should be noted that the corrosion resistance of steel fibres has been found to be superior to that of traditional steel bars. Although low-carbon steel fibres located near the surface or bridging cracks may be readily corroded, embedded fibres have proven to remain free of corrosion despite high chloride contents (Raupach et al., 2004). Therefore, any potential degradation of the mechanical properties of steel fibre reinforced concrete due to fibre corrosion was not considered in this study.

Due to the contribution of fibres, the number or diameter of longitudinal rebars may be reduced. In FRC1, the rebars were the same as in PL1, while FRC2 and FRC3 had the same diameter but a reduced number of rebars. In FRC4, a smaller rebar diameter, Ø12, was used but the number of bars was the same as that of PL1. First, the load capacity at the ultimate limit state was checked. Only one-way flexural capacity was calculated as it is the most important indicator

of structural performance. Figure 6 shows the stress block in the section analysis, in which the rigid-plastic model for residual tensile stress distribution in Model Code 2010 (International Federation for Structural Concrete, 2010) was adopted. The moment capacity was calculated using the following equation:

$$M_u = \alpha \cdot f_c \cdot b \cdot \gamma d_n \cdot \left(h_0 - \frac{\gamma d_n}{2} \right) - f_{Ftu} b (h - d_n) \left(\frac{h - d_n}{2} - c \right) \quad (1)$$

where $\alpha = 1$ and $\gamma = 0.8$, according to Model Code 2010 (International Federation for Structural Concrete, 2010), c is the distance from the outer surface to the centroid of the rebars, b and h are the width and height of the section and d_n is the height of neutral axis (determined from the force equilibrium on the section). f_{Ftu} is determined as $f_{R3}/3$, where f_{R3} is the residual flexural tensile strength, corresponding to a CMOD of 2.5 mm. f_{Ftu} was taken as 1.5 and 2.4 MPa for FRC with 0.5% and 1.0% vol. steel fibres (according to the experimental results in Löfgren et al., 2005 and Berrocal et al., 2018). The total steel area A_s , steel area in one side (top or bottom) $A_{s,l}$ and moment capacity M_u in each design are presented in Table 2.

The residual tensile stress of FRC in the service limit range, $f_{t,res}$, was used to determine the maximum and mean restraint crack width. The residual tensile strength at the crack width ≤ 0.5 mm was almost a constant value of 2.0 and 3.0 MPa for FRC, with 0.5% and 1.0% vol. steel fibres respectively (Jepsen et al., 2018). The restraint crack width was calculated using these parameters (given in Table 2). It can be seen that using an increased number of steel rebars in traditional RC (PL2) or using FRC can reduce the restraint-induced crack width, although the crack width in all four hybrid RC choices is smaller than in PL2. The maximum restraint crack width in all the designs, except FRC3 and FRC4, exceeds the allowable crack width mentioned in Section 2.1. It should be noted that restraint-induced cracking is usually not well considered in current structural design; it is not uncommon to have crack widths exceeding the allowable limit on site.

In addition, larger cracks are often injected or sealed to satisfy regulatory requirements, as can be seen from Figure 1.

4. SERVICE LIFE PREDICTION

4.1 Assumptions in the service life model

The service life of RC deteriorated by reinforcement corrosion consists of the corrosion initiation phase and corrosion propagation phase. One of the main difficulties of service life prediction is understanding the role that concrete cracks play in the corrosion process. Unfortunately, no consensus on the long-term impact of cracks has yet been reached among researchers, although it has been investigated and discussed extensively.

It is generally agreed that transverse cracks generated before corrosion initiation can accelerate the ingress of chlorides, inducing early pitting corrosion in the rebar (Schießl & Raupach, 1997). However, structures subjected to decades of corrosion usually exhibit a mixed morphology of general and pitting corrosion. This may be because the chloride content in the region that is free of transverse cracks also reaches a threshold value to initiate corrosion, or because the earlier-corroded region near the transverse cracks spreads the corroded sites along the rebar length with the propagation of longitudinal corrosion-induced cracks, as discussed in a recent study by the authors (E. Chen et al., 2020). It is a challenging task to model the evolution of the corrosion morphology and interactions between the cracks (transverse and longitudinal) and the corrosion process. To obtain a preliminary estimate, the corrosion initiation time was calculated in the respective cracked and uncracked regions of the edge beam and the time difference was further examined to estimate the level of pitting corrosion.

The corrosion propagation phase is the time from corrosion initiation to a ‘critical state’ when the damage to the structure is unacceptable. From a technical perspective, this critical state depends on the corrosion morphology and application of the RC member. Under uniform corrosion, since the major consequence of the reinforcement corrosion is concrete cover cracking

and spalling, corrosion-induced cracking and bond loss is more likely to lead to failure of the member. Under pitting corrosion, the rebars' mechanical properties, including load resistance and ductility, are more adversely affected than cover cracking and bond degradation.

Previous investigations on real decommissioned edge beams taken from two bridges in Sweden (Robuschi et al., 2020; Tahershamsi et al., 2017) have reported extensive cover cracking and spalling due to corrosion. Based on this, the corrosion propagation time in the present study was mainly predicted using a corrosion-induced cracking model. Moreover, the cross-sectional area loss percentage was also examined, to check the residual moment capacity. The critical corrosion-induced crack width has been suggested as 0.3 mm for the service limit state (Andrade et al., 1993). The critical crack width proposed in DuraCrete (2000) is 1 mm for the delamination risk induced by corrosion; however, greater values (2 mm or 3 mm) have been given in other studies (François et al., 2018). In this study, the critical corrosion-induced crack width implying the end of service life was determined by combining the predicted results and average service life of real edge beams.

4.2 Predicting corrosion initiation from chloride diffusion

4.2.1 Input parameters for chloride diffusion in uncracked concrete

In uncracked concrete, the chloride diffusion is usually modelled by a one-dimensional diffusion process. The solution of the chloride concentration along the distance x (to the surface) at time t from Fick's second law is given as:

$$C(x, t) = C_s \cdot \operatorname{erfc}\left(\frac{x}{2\sqrt{D_0 \cdot t}}\right), \quad (2)$$

where C_s is the surface chloride content, D_0 is the chloride diffusivity of uncracked concrete and erfc is the complementary error function. A constant surface chloride content was assumed to be 1% by weight of cement (that is, 1.0 wt.-%/cement) based on the average chloride content found in field specimens exposed to a highway in Sweden sprayed with de-icing salts (Tang &

Utgenannt, 2007). The critical chloride content C_{crit} initiating corrosion was assumed to be 0.6 wt.-%/cement, which is a mean value proposed in the code (International Federation for Structural Concrete, 2006). According to the experimental results obtained by Berrocal (2017), the addition of steel fibres has a marginal effect on the chloride diffusivity of uncracked concrete. In that study, the chloride diffusion coefficients of PL and FRC with steel fibres with similar mix proportion (with water/cement ratio of 0.47) at age 420 days were 8×10^{-12} and 7.7×10^{-12} m²/s respectively. Consequently, in this case study, D_0 was taken as 8×10^{-12} m²/s for both PL and FRC.

5.1. 4.2.2 Chloride diffusion in cracked concrete

The corrosion initiation time in the cracked regions was predicted using a semi-empirical model proposed by Leung and Hou (2015), see the equations in the Supplementary 2. This model is particularly convenient to use as only the chloride diffusivity D_0 in Equation (2) needs to be replaced by an equivalent chloride diffusivity D_{eq} of cracked concrete. D_{eq} is related to D_0 , the chloride diffusivity in the crack D_{cr} and the crack width.

To determine D_{cr} for PL and FRC used in this case study, the experimental results reported previously (Berrocal, 2017; Berrocal et al., 2015) were examined and used in the semi-empirical model. In Berrocal et al. (2015), the corrosion initiation time t_{ini} was measured for rebars in uncracked and pre-cracked traditional and hybrid RC beams cyclically exposed to chloride solution with a chloride concentration of 0.75 wt.-%/concrete (that is, 4.8 wt.-%/cement) (Berrocal, 2017). The pre-existing cracks were produced using three-point bending; the maximum crack width reached before unloading (noted as w_{pre}) was set at 0.1, 0.2, 0.3 and 0.4 mm. The surface crack width after unloading in all pre-cracked beams ranged between 0.02 and 0.06mm. Moreover, the chloride diffusivity of uncracked concrete D_0 was also measured (Berrocal, 2017).

D_{cr} was assumed to be constant for the different crack widths in the tested range. The value of D_{cr} was found by inverse analysis, to match the predicted t_{ini} with the experimental results. When D_{cr} was 45×10^{-10} and 30×10^{-10} m²/s for PL and FRC respectively, the predicted results

compared well with the experimental results, except for t_{ini} at 0.1 mm crack width, see Figure 7. The predicted t_{ini} at 0.1 mm is higher than the experimental value. This may be because the smaller crack width is difficult to measure accurately in the experiments and t_{ini} is very sensitive to crack widths between 0.1 and 0.2 mm. The order of magnitude of D_{cr} was consistent with the results in Djerbi et al. (2008), although the values reported in that study were several times smaller. Moreover, D_{cr} in FRC was one third smaller than that in PL. This relationship is close to the results reported in Wang et al. (2018). The obtained D_{cr} was adopted in the case study to calculate the corrosion initiation time in the cracked region. The input parameters used in the chloride diffusion analysis are summarised in Table 3.

4.3 Finite element modelling of corrosion-induced cracking

4.3.1 Corrosion model

The corrosion-induced cracking propagation was modelled with the finite element (FE) software DIANA10.3. Uniform corrosion was assumed, so a two-dimensional plane-strain model was set up. The corrosion effect was modelled using a corrosion model developed by Lundgren (2005). In this model, corrosion expansion is simulated by applying swelling of the 2D zero-thickness interface layer between concrete and steel. The constitutive law of the corrosion products is described by a power law ($\sigma_n = K_{corr} \cdot \epsilon_{corr}^p$) to simulate the granular nature of corrosion products. For further details of the formulation, the reader is referred to the original work (Lundgren, 2005). The model is implemented by applying the corrosion penetration depth x_u incrementally in time steps. With the volumetric ratio of corrosion products n_v given, the free radial displacement of the interface u_{free} is calculated using Equation (3):

$$u_{free} = \sqrt{r^2 + (n_v - 1) \cdot (2rx_u - x_u^2)} - r \quad (3)$$

where r is the initial radius of the rebar and the other parameters are defined in Figure 8.

Due to the constraint of concrete cover, the real displacement of the interface u_{ncor} is smaller than the free increase. This results in a compressive state in the rust and generates compressive radial stresses and tensile hoop stresses in the concrete. Through the equilibrium and compatibility conditions in concrete elements, interface elements and steel elements, the stress and strain variables in concrete can be solved with the help of numerical schemes.

4.3.2 Description of the FE model

A thin slice of half the edge beam cross-section (with 20 mm thickness) was modelled, to reduce the number of elements and computational time. The displacement of the rear surface of the slice was constrained in the normal direction, to take the effect of surrounding concrete into account. A symmetrical boundary condition was applied at the mid-line of the cross-section. The top of the section was vertically constrained to avoid rigid body movement. In this modelling, only the rebars in the bottom layer were assumed to have corroded. This was to reduce the cracking elements and thereby computational time. Due to the large distance between the bars at the top and bottom, the corrosion in the top layer would have little influence on the internal stress distribution at the bottom region and vice versa. The element type for concrete and reinforcement bars was 3D tetrahedral (TE12L). The steel-concrete interface was modelled using a 2D interface element (T18IF). The meshes and boundary conditions of the case PL1 are shown in Figure 9.

The constitutive law of concrete was described by the compressive and tensile stress-strain curves including the softening branch. In addition to the strength and elastic modulus given in Table 1, the compressive behaviour of both PL and FRC was modelled using the curve suggested by Thorenfeldt (1987). The tensile softening of PL was modelled using the softening law proposed by Hordijk (1991) and the fracture energy of PL was calculated as 148 N/m, according to Model Code 2010 (International Federation for Structural Concrete, 2010). For the tensile behaviour of FRC, the multilinear curve obtained through an inverse analysis of the flexural test results (by Jepsen et al., 2018) was used. Concrete cracking was simulated using the total strain rotating crack

model. The crack band width was set as the cube root of the element volume (as proposed by Rots, 1988). The parameters of rust suggested by Lundgren (2005) were used: $K_{corr} = 14$ GPa, $p = 7$ and the volumetric ratio $n_v = 2$. The applied corrosion penetration depth was $2 \mu\text{m}$ at each time step. A Newton-Raphson iterative scheme was used in the FE analysis to solve the equilibrium equations.

5. LIFE-CYCLE COST ANALYSIS

5.1 Definitions of inventory

LCCA considers all relevant costs over a period of analysis and is expressed as a monetary value. The LCC of an infrastructure project is usually divided into three parts: agency costs, user costs and society costs (Salokangas, 2013). Agency costs are also called owner costs and include the costs of the planning and design, construction, maintenance and operation, and disposal phases. Costs arising from traffic delay and vehicle operations during the maintenance period are user costs. Society costs are associated with environmental impacts and accident costs. This study considered the investment costs due to construction (noted as ‘INV’), maintenance costs due to the edge beam replacement (noted as ‘REP’) and user costs caused by the replacement work (noted as ‘USE’). Other items were excluded for various reasons. Some of them do not cause any obvious differences between different alternatives, such as the planning and design costs and accident costs. Some may account for a minor proportion of the total costs, such as regular inspection and minor repair costs compared to replacement costs. Disposal costs were not considered since they are related to the reuse or recycle strategies, which are uncertain.

LCC is represented by the sum of the three parts considered in this study, see Equation (4). The calculation equations for each part are presented in the Supplementary 3.

$$\text{LCC} = \text{INV} + \text{REP} + \text{USE} \quad (4)$$

5.2 Input parameters in the case study

In the case study, different alternatives for the edge beam were designed for the same road bridge. The design service life of the bridge may influence the replacement interval of the edge beam. Two different lifespans T , of 80 and 120 years, were considered. Since the bridge length L_{bridge} influences the affected roadway length during the road work and thereby the user costs, a short bridge of 15 m and a long bridge of 150 m were both considered. The road type was assumed to be two-way single-lane, with lane width 3.5 m and shoulder width 2.0 m in each direction. The corresponding traffic speed for this road type was assumed based on the data given in (Veganzones Muñoz et al., 2016). The region of the bridge was not specified, but the average daily traffic ADT was assigned in the range of 5000-20000 vehicles/day for the sensitivity analysis.

The unit cost of steel fibres m_f on the market is normally in the range 15-25 SEK/kg (SEK = Swedish krona). Marginal additional costs may arise if the workability of the concrete is affected by adding fibres, but generally no additional labour cost for casting fibres is required. If zinc-coated or stainless-steel fibres were to be used to eliminate surface corrosion spots for aesthetic reasons, the price would be higher. A fibre cost ranging from 10 to 60 SEK/kg was therefore used in the sensitivity analysis.

The discount rate p is an important factor in LCCA where future costs are involved. A higher discount rate implies a lower present value of future costs. The currently recommended discount rate in Sweden is from 3.5% to 4%, although the actual future discount rate is uncertain. Thus, a greater range of discount rates from 2% to 7% was chosen in the sensitivity analysis.

All the input parameters in LCCA are given in the Supplementary 3. The unit cost of the edge beam replacement provided in the literature was regarded as the cost of the basic design (PL1). The unit replacement cost for other alternatives was adjusted by scaling the replacement cost of the basic design, based on the ratio of their investment cost.

6. LIFE-CYCLE ASSESSMENT

6.1 Definitions in LCA

The environmental impacts evaluated in the life-cycle assessment are categorised into classes according to the type of environment issues. The indicators related to potential environmental impacts from construction (EPD, 2019) include: global warming potential (GWP), acidification potential (AP), eutrophication potential (EP), formation potential of tropospheric ozone (POCP), abiotic depletion potential and water scarcity potential. They should be incorporated into the environmental product declarations (EPD) of a product.

A complete LCA of construction works should involve four stages of the life cycle (British Standards Institution, 2012): (1) material production stage (labelled A1-A3) including raw material extraction, transport of raw materials and manufacturing; (2) construction process stage (A4-A5) including transportation of the materials and equipment to the construction site, installation and construction work; (3) user stage (B1-B7) including maintenance, repair, replacement (MR&R) and operational energy and water use; and (4) end-of-life stage (C1-C4) including demolition, waste processing and associated transport and disposal. The reuse and recycling of materials beyond the life cycle may also be a part of LCA.

The environmental impacts during the construction process stage A4-A5 for the traditional and hybrid reinforced structures may be regarded as similar, so they were not considered in this comparative study. The environmental impacts caused by the edge beam replacement during the bridge's lifespan may be different; however, the EPD of the materials produced in the future decades are uncertain. Since the European Union aims to attain zero emissions by 2040/2050, both the steel and cement industries are looking at carbon capture and utilisation (CCU) and carbon capture and storage (CCS) strategies to reach the goal. If carbon neutrality is realised in the future, the EPD data of materials reported nowadays will not hold then. Therefore, the LCA analysis of the replaced edge beams was limited to a cradle to gate approach. Moreover, concrete absorbs CO₂ through carbonation in both its service life and recycling stage (Stripple et al., 2018). However, taking this into account is not straightforward. Due to these limitations, only the greenhouse gas

emissions responsible for the GWP during the material production stage (A1-A3) of the edge beam at the bridge construction stage were considered.

6.2 EPD of the materials

The greenhouse gas emissions of a product are reported in kg CO₂ equivalents in the EPD. The EPD of concrete from Svensk Betong and steel fibres from Mapei were collected from EPD-Norge Program (EPD-Norge, 2017a, 2017b). For steel rebars, it was found that the average GWP value provided by different producers may have several times variance; therefore, three producers (Arcelormittal, n.d.; Celsa, n.d.; UK CARES, n.d.) reporting distinct values were all considered. Table 4 lists the GWP arising from raw materials extraction, transport and manufacturing (A1-A3) used in this study.

7. RESULTS AND DISCUSSIONS

7.1 Results on the service life prediction

7.1.1 Corrosion initiation time

Table 5 gives the corrosion initiation time in cracked and uncracked regions for each design. The corrosion initiation time in the uncracked region $t_{i,u}$ was the same in all designs, while the corrosion initiation time in the cracked region $t_{i,cr}$ is longer at smaller crack width. The time difference between $t_{i,u}$ and $t_{i,cr}$ is reduced as the restraint crack width is decreased. The possible consequence of this reduced time difference may be a reduction in localised pitting corrosion before corrosion morphology becomes generalised.

Since pitting corrosion causes much less cover cracking (including crack width and crack length) than uniform corrosion, it was assumed that the corrosion initiation for uncracked concrete occurs before any cover cracking due to pitting corrosion. Considering this, in the service life model of the present study, the corrosion initiation time was taken as the time for the uncracked region $t_{i,u}$, after which the corrosion propagation period mainly exhibiting generalised corrosion started. It should be noted that this assumption may overestimate the service life. Furthermore, this

overestimation is greater for PL1 and PL2 than the FRC groups as the time difference of $t_{i,u}$ and $t_{i,cr}$ is greater in PL1 and PL2.

7.1.2 Corrosion propagation time

The FE modelling simulated the crack propagation with increasing corrosion depth. The contour plots of the maximum principal crack width at different corrosion depths are shown in Figure 10. Note that greater corrosion depths were selected for the FRC cases since cracking appears later and propagates more slowly in the FRC. As observed, crack localisation took place along a single row of elements, so the crack band width chosen for the model was appropriate.

From Figure 10, the difference in the final crack pattern for different reinforcement layouts can also be observed. Initially, the first localised crack or ‘main crack’ (marked as ‘*crack a*’) propagated to the nearest surface in all cases except PL2-II; in PL2-II, the main crack was formed between the rebars due to the smaller rebar spacing. In PL1, PL2-I, FRC1 and FRC4, with increasing corrosion depth, a second crack (marked as ‘*crack b*’) developed in the horizontal direction and connected with the horizontal crack caused by corrosion in the neighbouring rebar. The third crack (marked as ‘*crack c*’) was subsequently formed in an inclined direction. Once it reaches the outer surface, cover spalling in the corner will occur. The connected horizontal cracks may also cause delamination of the cover. The predicted crack patterns are close to those observed on-site. No horizontal delamination was formed in FRC2 and FRC3, as rebar spacing in them is greater than in PL1, PL2 and FRC1. Rather, the second crack tended to develop inclinedly towards to the edge. In FRC4, where smaller rebar diameter ($\varnothing 12$) was used, the cracking level was the lowest.

The crack width of the main crack (‘*crack a*’) versus the uniform corrosion depth ($w_{corr} - x_u$ relation) is plotted in Figure 11. The crack width $w_{corr} = 0.05$ mm, which at close proximity is visible to the naked eye, was defined as the surface crack initiation. It can be seen that surface crack initiation is delayed in all the FRC cases. Moreover, the crack starting from the steel-concrete

interface propagated to the surface in a sudden way in PL, whereas the progress was more gradual in FRC. It took the greatest corrosion depth for the visible crack to propagate to the surface in FRC4. After the surface crack initiation, the crack width increases almost linearly with the corrosion depth in PL1 and PL2, but slightly nonlinearly in the FRC. For the sake of comparison, a linear fitting was conducted to describe the $w_{corr} - x_u$ relationship in all cases. In those cases where results might not be accurately obtained due to convergence problems in the FE analysis, the crack width was calculated from this linear relationship. It is noteworthy that the predicted crack width from the linear fitting for the FRC would be slightly conservative.

From Figure 11, the slope of the $w_{corr} - x_u$ relationship is smaller in FRC than in PL. With the same fibre volume fraction but different reinforcement layouts, FRC2 (with 8Ø16) induces a larger surface crack width than FRC1 (with 10Ø16) since the second crack developing horizontally in FRC1 (due to smaller steel spacing) slowed the widening of the main crack. From all the FRC cases, FRC4 reduced the corrosion crack width the most. For the PL cases, the corrosion crack width in both PL2-I and PL2-II is larger than that in PL1 at the same corrosion depth. This can be explained by the fact that in PL2-I, a bundle of two rebars was used, thus exhibiting a similar effect to that of increasing the rebar diameter on the corrosion crack width, and that in PL-II, the decreased rebar spacing aggravated the horizontal crack propagation. As a result, although increasing the number of rebars can reduce the mechanically and restraint-induced crack width, it causes earlier corrosion cracking and increases the crack width of the main corrosion crack regardless of whether the rebars are bundled or placed at smaller spacing.

7.1.3 Service life comparison

For the corrosion propagation time, the corrosion rate is an important parameter for converting the corrosion depth in the model to time. A constant corrosion rate of 10 µm/year was assumed in all cases. This corresponds to a corrosion rate in the ‘high corrosion’ state as measured for beams exposed to de-icing salts on a highway (Tang & Utgenannt, 2007), or a ‘moderate corrosion rate’

according to Bertolini et al. (2013). Taking the critical crack width as 0.5 mm, the critical corrosion depth $x_{w0.5,u}$ and corrosion propagation time $t_{w0.5,u}$ were determined. The results are presented in Table 6. For the basic design PL1, the time to reach critical crack width, $t_{w0.5,u}$, was 35.5 years, and the service life, T_{eb} , was about 50 years, after adding the corrosion initiation time $t_{i,u}$ (14.3 years). The predicted service life is very close to the average service life of the edge beam in practice (that is, 45 years). Therefore, the critical crack width of 0.5 mm was regarded as a reasonable criterion in the present model, for those cases in which corrosion-induced cracking dominates the decommission of the edge beam.

For FRC4, it was found that the required corrosion penetration depth to induce a 0.5 mm crack width was excessively large, namely $x_u/r > 0.29$ (where $r = 6\text{mm}$). This resulted in a very high percentage of cross-sectional area loss ΔA_s (49.8%). This may cause the residual capacity of FRC4 to fail to satisfy the safety requirement well before reaching the critical crack width. Accordingly, the residual capacity criterion was also examined, to calculate the limit of cross-sectional area loss ΔA_s for the safety consideration. To the authors' knowledge, there is not a consensus regarding the admissible capacity loss in corroded RC structures. For residual safety considerations, a limit of 10% in rebar area reduction was suggested in Cairns et al. (2003) whereas 30% was used by Amey et al. (1998). In terms of load capacity loss, a limit of 50% was given by Torres-Acosta & Martínez-Madrid (2003), and a strength loss limit of 60% was used by Li (2004). It should be noted that the relationship between the strength/capacity loss and the rebar cross-sectional area loss strongly depends on the corrosion pattern (uniform corrosion or pitting corrosion) and whether the cross-sectional area loss is given as the average or the maximum local loss along the rebar. This may be one of the main reasons explaining the large variations in the admissible cross-sectional area loss or capacity loss proposed by different researchers. Considering the nature of generalised corrosion in this case study, a 15% limit of capacity loss was assumed. The limit value of ΔA_s , as well as the corresponding corrosion depth $x_{\Delta Mu=15\%}$ and corrosion

propagation time $t_{\Delta Mu=15\%}$ are given in Table 6. The smaller value of $t_{w0.5,u}$ and $t_{\Delta Mu=15\%}$ was taken as the corrosion propagation time t_p . With the exception of FRC4, the crack width criterion limits the end of service life for all cases.

The service life of different designs is compared in Table 7. The service life of PL2 is slightly shorter than PL1, while FRC1 and FRC2 extend the service life of the basic design by 94% and 58% respectively. FRC3 and FRC4 extend it by 104% and 154% respectively. The service life of FRC4 is even longer than the design life of most bridges. With the same amount of fibres, FRC1 performs better than FRC2 (for $v_f = 0.5\%$ vol.) and FRC4 better than FRC3 (for $v_f = 1.0\%$ vol.), due to the different reinforcement amounts and layouts and, therefore, corrosion crack widths.

7.2 LCCA results

The cost results were expressed as the costs per bridge length. The base values of the parameters which varied in the sensitivity analysis were selected as: $T = 120$ years, $L_{bridge} = 15$ m, $m_f = 20$ SEK/kg, $p = 3.5\%$, and $ADT = 10000$ vehicles/day. Detailed results are included in the Supplementary 4.

7.2.1 Influence of unit cost of fibre on investment costs and life-cycle costs

Figure 12a shows the influence of m_f on investment costs. When m_f is equal to, or less than, 20 SEK/kg, the investment costs of all FRC cases are close to, or slightly higher than, that of PL1 but less than that of PL2. Therefore, using a greater amount of reinforcement may be more expensive than using fibres to control the transverse crack width. At the highest fibre cost (which might correspond to, say, stainless-steel fibres), the investment costs of FRC3 and FRC4 are about 30% and 24% higher than that of PL1. The total LCC after considering replacement and user costs is compared in Figure 12b. The LCC in all the FRC cases is less than in PL1 and PL2, even at the highest fibre cost. Under a normal fibre cost ($m_f = 20$ SEK/kg), the total LCC of different hybrid

RC designs is 37-54% lower than that of the basic traditional RC design.

5.2. 7.2.2 Sensitivity analysis on life-cycle costs

The influence of the bridge design life T , bridge length L_{bridge} , average daily traffic ADT , and discount rate p , on the life-cycle costs are presented in Figure 13, Figure 14, Figure 15 and Figure 16 respectively. The main findings from the sensitivity analysis are: i) in all the studied cases, hybrid RC designs have lower LCCs than the traditional RC designs PL1 and PL2; ii) LCC is most sensitive to the discount rate but only slightly affected by the bridge design life, bridge length and average daily traffic; iii) the replacement and user costs of hybrid RC designs are reduced substantially, compared to that of traditional RC ones.

It is worth noting that, although the replacement and user costs at the investment time (that is, year 0) are similar, the present value of the replacement and user costs at the end of the edge beam's life for each design has a major difference. This is mainly because the present value of the future costs is related exponentially to the replacement time (that is, the service life of the edge beam). The significantly longer service life of hybrid RC edge beams delays the first-time replacement by over 29 years (see Table 7). In the traditional RC edge beam, the sum of replacement and user costs are comparable to the investment costs under a normal discount rate of 3.5%. However, in the hybrid RC edge beam, they are only a small fraction of the investment costs, or even zero.

The bridge length and average daily traffic only influence the user costs, see Figure 14 and Figure 15. Under the same average daily traffic, the user costs per meter are less for the longer bridge. As ADT increases, user costs occupy a higher portion of the total LCC. However, these two parameters have only a minor influence on the relative difference of LCC for hybrid RC and traditional RC designs.

The discount rate has a major influence on both the replacement and user costs. At the lowest discount rate of 2.0%, the replacement and user costs of the traditional RC designs are even

significantly higher than the investment costs, while they decrease to only a small fraction of the investment costs as the discount rate increases, see Figure 16. The replacement and user costs in the three hybrid RC designs (FRC1, FRC2 and FRC3), which need one-time replacement, are still less than the investment costs, even when the discount rate is very low due to the delayed replacement (as mentioned) and almost negligible at the highest discount rate. As for the total LCC, the reduction ratio of LCC for the hybrid RC designs relative to that of PL1 is greatest at the lowest discount rate and becomes insignificant as the discount rate increases to 7%. Therefore, hybrid RC designs can bring greater cost benefit at a lower discount rate. Only when the discount rate and fibre cost are both very high might the LCC of the hybrid RC designs be higher than that of traditional RC ones.

7.3 LCA results

The total GWP of the materials to produce the edge beam were calculated and expressed as kg CO₂ eq. per unit length of edge beam. The original data is included in the Supplementary 5. Figure 17 gives the GWP from the concrete, steel rebar and steel fibre in each alternative design. The results show that concrete takes up the majority of the total GWP. When steel rebar produces 0.37 or 0.839 kg CO₂ eq./kg, the total GWP in all the hybrid RC designs is slightly higher than that of traditional RC designs PL1; nevertheless, the difference is small. Under higher CO₂ eq. of steel rebar (1.23 kg CO₂ eq./kg), PL2 stands out a little, with the highest total GWP. This implies that when the GWP of steel rebar is high, it is not environmentally friendly to control the transverse crack width by increasing the number of steel rebars.

The annual total GWP of each design within the service life of the edge beam T_{eb} is compared in Figure 18. The annual total GWP of all the hybrid RC designs is lower than that of the traditional RC ones, regardless of the GWP value of steel rebar and it can be reduced by 33-60% relative to the basic traditional design PL1.

8. CONCLUSIONS

This paper presents a case study of a bridge edge beam in Sweden, in which the service life, economic and environmental performance of hybrid and traditional reinforced concrete were compared. The results obtained in this study demonstrate that a hybrid RC edge beam with a low-to-moderate fibre content can reach a significantly longer service life than the traditional edge beam. It also provides a sustainable solution for the edge beam, from the economic and environmental points of view. The main conclusions from this study are as follows.

- (1) Adding fibres can effectively control the restraint-induced cracking and corrosion-induced cracking, while possibly reducing the required number and/or diameter of traditional reinforcement bars. Conversely, increasing the amount of steel rebars to control restraint crack width in the traditional RC design had a negative effect on corrosion-induced crack propagation.
- (2) Among the different reinforcement configurations investigated, using 1.0% vol. steel fibres and reduced diameter of steel rebars was the most favourable combination for controlling corrosion cracks. However, the corrosion level required to reach the critical crack width entailed a great loss of steel area, thus posing a safety issue. Moreover, it should be noted that common warning signs of severe corrosion, such as wide corrosion cracks and cover spalling, may not be present in hybrid RC if high amounts of fibres are used.
- (3) The service life of the edge beam can be extended by 58-94% when adding 0.5% vol. fibres and by 104-154% when adding 1.0% vol. fibres.
- (4) The total LCC of different hybrid RC edge beam designs is about 37-54% less than the basic traditional RC design, under the base values for all the variable parameters. The investment costs of the hybrid RC designs are slightly higher than those of the traditional RC design at higher fibre costs, while the total LCC in all the hybrid RC designs is lower,

due to delayed replacement and reduced instances of replacement. The bridge design life, bridge length and average daily traffic do not obviously affect the comparative LCC results, while the discount rate has a major impact. The benefit in reducing LCC by using hybrid RC is greater at a lower discount rate.

- (5) LCA shows that the total GWP from the materials used in producing the hybrid RC edge beam is close to or slightly higher than that of the basic traditional design. However, the annual total GWP in the hybrid RC designs is 33-60% lower, owing to the longer service life.

The LCC and LCA results provided in the paper cannot be extrapolated to all sorts of structures, as they are very much dependent on the assumptions taken in the analysis. In addition, for new structural materials, due to the lack of long-term field data, the accuracy of the service-life model becomes central for the LCC and LCA analysis. Further studies on the criteria used to define the end of the corrosion propagation stage for hybrid RC are required to improve the developed service-life model in this paper.

Acknowledgements:

The work reported in this paper was supported by the Swedish Transport Administration under Grant TRV 2018/36506; construction industry's organisation for research and development (SBUF) under Grant 13683; Chalmers University of Technology; Thomas Concrete Group; and Cements AB (Heidelberg Cement Group).

Disclosure statement:

No potential conflict of interest was reported by the authors.

References:

- Al-Kamyani, Z., Guadagnini, M., & Pilakoutas, K. (2019). Impact of shrinkage on crack width and deflections of reinforced concrete beams with and without steel fibres. *Engineering Structures*, *181*, 387-396.
- Amey, S. L., Johnson, D. A., Miltenberger, M. A., & Farzam, H. (1998). Predicting the service life of concrete marine structures: an environmental methodology. *Structural Journal*, *95*(2), 205-214.

- Andrade, C., Alonso, C., & Molina, F. (1993). Cover cracking as a function of bar corrosion: Part I- Experimental test. *Materials and structures*, 26(8), 453-464.
- Arcelormittal. (n.d.). *Environmental Product Declaration* <https://epd-online.com/PublishedEpd/Download/9604>
- Berrocal, C. G. (2017). *Corrosion of steel bars in fibre reinforced concrete: Corrosion mechanisms and structural performance* [Doctoral Thesis, Chalmers University of Technology].
- Berrocal, C. G., Fernandez, I., Lundgren, K., & Löfgren, I. (2017). Corrosion-induced cracking and bond behaviour of corroded reinforcement bars in SFRC. *Composites Part B: Engineering*, 113, 123-137.
- Berrocal, C. G., & Löfgren, I. (2018). *Hybrid Reinforcement Systems for Crack Width Control in Concrete Structures* (Report No. SBUF project number 12250). Chalmers University of Technology
- Berrocal, C. G., Löfgren, I., & Lundgren, K. (2018). The effect of fibres on steel bar corrosion and flexural behaviour of corroded RC beams. *Engineering Structures*, 163, 409-425.
- Berrocal, C. G., Löfgren, I., Lundgren, K., & Tang, L. (2015). Corrosion initiation in cracked fibre reinforced concrete: influence of crack width, fibre type and loading conditions. *Corrosion Science*, 98, 128-139.
- Bertolini, L., Elsener, B., Pedferri, P., Redaelli, E., & Polder, R. (2013). *Corrosion of steel in concrete*. Wiley Online Library.
- Blunt, J., Jen, G., & Ostertag, C. P. (2015). Enhancing corrosion resistance of reinforced concrete structures with hybrid fiber reinforced concrete. *Corrosion Science*, 92, 182-191. <https://doi.org/https://doi.org/10.1016/j.corsci.2014.12.003>
- Boverket. (2019). *Boverkets konstruktionsregler, EKS11*. Swedish National Board of Housing, Building and Planning.
- British Standards Institution. (2012). *Sustainability of construction works-Environmental product declarations-Core rules for the product category of construction products* (BS EN 15804:2012).
- British Standards Institution. (2013). *Concrete. Specification, performance, production and conformity* (BS EN 206:2013).
- Cairns, D., Du, Y., & Law, D. (2003). Structural assessment of corrosion damaged bridges. (Ed.),^(Eds.). PROCEEDINGS OF THE 10TH INTERNATIONAL CONFERENCE AND EXHIBITION-STRUCTURAL FAULTS AND REPAIR CONFERENCE 2003, HELD LONDON, JULY 2003-CD ROM.
- Celsa. (n.d.). *Environmental Product Declaration* <https://gryphon4.environdec.com/system/data/files/6/8564/epd305%20Celsa%20Steel%20Service%202018.pdf>
- Chen, E., Berrocal, C. G., Löfgren, I., & Lundgren, K. (2020). Correlation between concrete cracks and corrosion characteristics of steel reinforcement in pre-cracked plain and fibre-reinforced concrete beams. *Materials and structures*, 53(2), 33.
- Chen, Z., & Yang, E.-H. (2019). Microstructural investigation of steel corrosion in strain hardening cementitious composite (SHCC). *Construction and Building Materials*, 211, 185-198.
- Comite Euro-internacional du beton. (1995). *High performance concrete, recommended extensions to the model code 90, research needs* (Bulletin 228).
- Djerbi, A., Bonnet, S., Khelidj, A., & Baroghel-Bouny, V. (2008). Influence of traversing crack on chloride diffusion into concrete. *Cement and Concrete Research*, 38(6), 877-883.

- DuraCrete. (2000). Probabilistic performance based durability design of concrete structures *The European Union -Brite EuRam III, Final technical report of Duracrete project, Document BE95 - 1347/R17*.
- Engström, B. (2007). *Restraint cracking of reinforced concrete structures*. Chalmers University of Technology.
- EPD-Norge. (2017a). *Mapei*. The Norwegian EPD Foundation <https://www.epd-norge.no/fiber-reinforcement/steelfibre-de-35-0-55-de-50-0-75-og-de-50-1-0-article1633-423.html>
- EPD-Norge. (2017b). *Svensk Betong*. The Norwegian EPD Foundation <https://www.epd-norge.no/betongvarer/betong-for-vagbro-article1540-316.html>
- EPD. (2019). *International EPD system, PCR basic module. CPC division 53: Constructions. Version 3.02* <https://www.environdec.com/PCR/Detail/?Pcr=7070>
- European Committee for Standardization. (2004). *Eurocode 2: Design of concrete structures: Part 1-1: General rules and rules for buildings* (BS EN 1992-1-1:2004). British Standards Institution.
- François, R., Laurens, S., & Deby, F. (2018). *Corrosion and its consequences for reinforced concrete structures*. Elsevier.
- Hordijk, D. A. (1991). *Local approach to fatigue of concrete* [Doctoral dissertation, Delft University of Technology].
- International Federation for Structural Concrete. (2006). *Model Code for Service Life Design* (Bulletin 34).
- International Federation for Structural Concrete. (2010). *fib Model Code for Concrete Structures 2010*.
- Jepsen, M. S., Damkilde, L., Lövgren, I., & Berrocal, C. (2018). Adaptive inverse analysis (AIA) applied and verified on various fiber reinforced concrete composites. *Materials and structures*, 51(3), 60.
- Koch, G. H., Brongers, M. P., Thompson, N. G., Virmani, Y. P., & Payer, J. H. (2002). *Corrosion cost and preventive strategies in the United States* (Report No. FHWA-RD-01-156, R315-01). United States. Federal Highway Administration
- Löfgren, I. (2007). *Calculation of crack width and crack spacing*. Nordic Mini Seminar" Fibre reinforced concrete.
- Löfgren, I., Stang, H., & Olesen, J. F. (2005). Fracture properties of FRC determined through inverse analysis of wedge splitting and three-point bending tests. *Journal of Advanced Concrete Technology*, 3(3), 423-434.
- Leung, C. K., & Hou, D. (2015). Numerical simulation of chloride-induced corrosion initiation in reinforced concrete structures with cracks. *Journal of Materials in Civil Engineering*, 27(3), 04014122.
- Li, C. Q. (2004). Reliability based service life prediction of corrosion affected concrete structures. *Journal of Structural Engineering*, 130(10), 1570-1577.
- Lundgren, K. (2005). Bond between ribbed bars and concrete. Part 2: The effect of corrosion. *Magazine of Concrete Research*, 57(7), 383-395.
- Mattsson, H.-Å., Sundquist, H., & Silfwerbrand, J. (2007). The real service life and repair costs for bridge edge beams. *Restoration of buildings and monuments*, 13(4), 215-228.
- Niu, Y., & Fink, G. (2018). Life Cycle Assessment on modern timber bridges. *Wood Material Science & Engineering*, 14(4), 212-225.
- Penadés-Plà, V., Martí, J. V., García-Segura, T., & Yepes, V. (2017). Life-cycle assessment: A comparison between two optimal post-tensioned concrete box-girder road bridges. *Sustainability*, 9(10), 1864.

- Racutanu, G. (2001). *The real service life of Swedish road bridges* [Doctoral dissertation, Institutionen för byggkonstruktion].
- Raupach, M., Dauberschmidt, C., & Eichler, T. (2004). *Corrosion behaviour of steel fibres in concrete containing chlorides*. EUROCORR2004 - European Corrosion Conference, Long Term Prediction and Modelling of Corrosion, Nice.
- Robuschi, S., Sumearll, J., Fernandez, I., & Lundgren, K. (2020). Bond of naturally corroded, plain reinforcing bars in concrete. *Structure and Infrastructure Engineering*, 53(2), 1-17.
- Rots, J. G. (1988). *Computational modeling of concrete fracture* [Doctoral dissertation, Delft University of Technology].
- Sadrinejad, I., Ranjbar, M. M., & Madandoust, R. (2018). Influence of hybrid fibers on serviceability of RC beams under loading and steel corrosion. *Construction and Building Materials*, 184, 502-514.
- Safi, M., Sundquist, H., Karoumi, R., & Racutanu, G. (2013). Development of the Swedish bridge management system by upgrading and expanding the use of LCC. *Structure and Infrastructure Engineering*, 9(12), 1240-1250.
- Salokangas, L. (2013). *ETSI project: Bridge Life Cycle Optimisation: stage 3*. Aalto University - School of Engineering
- Schießl, P., & Raupach, M. (1997). Laboratory studies and calculations on the influence of crack width on chloride-induced corrosion of steel in concrete. *Materials Journal*, 94(1), 56-61.
- Stripple, H., Ljungkrantz, C., Gustafsson, T., & Andersson, R. (2018). *CO₂ uptake in cement-containing products: Background and calculation for IPCC implementation* (Report No. B 2309). IVL Swedish Environmental Research Institute
- Tahershamsi, M., Fernandez, I., Lundgren, K., & Zandi, K. (2017). Investigating correlations between crack width, corrosion level and anchorage capacity. *Structure and Infrastructure Engineering*, 13(10), 1294-1307.
- Tang, L., & Utgenannt, P. (2007). *Chloride Ingress and Reinforcement Corrosion in Concrete under De-Icing Highway Environment-A study after 10 years' field exposure* (Report No. 2007:76). SP Technical Research Institute of Sweden
- Thoft-Christensen, P. (2012). Infrastructures and life-cycle cost-benefit analysis. *Structure and Infrastructure Engineering*, 8(5), 507-516.
- Thorenfeldt, E. (1987). *Mechanical properties of high-strength concrete and applications in design*. Symposium Proceedings, Utilization of High-Strength Concrete, Norway.
- Torres-Acosta, A. A., & Martínez-Madrid, M. (2003). Residual life of corroding reinforced concrete structures in marine environment. *Journal of Materials in Civil Engineering*, 15(4), 344-353.
- Trafikverket. (2011). *TRVR Trafikverkets tekniska råd Bro 2011: 086 D.1.4.1.6*. Swedish Transport Administration.
- UK CARES. (n.d.). *Environmental Product Declaration*
<https://ukcares.com/downloads/general/BREG%20EN%20EPD%20000125.pdf>
- Vandewalle, L. (2000). Cracking behaviour of concrete beams reinforced with a combination of ordinary reinforcement and steel fibers. *Materials and structures*, 33(3), 164-170.
- Veganzones Muñoz, J. J. (2016). *Bridge edge beams: LCCA and structural analysis for the evaluation of new concepts* [Licentiate thesis, KTH Royal Institute of Technology].

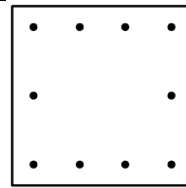
- Veganzones Muñoz, J. J., Pettersson, L., Sundquist, H., & Karoumi, R. (2016). Life-cycle cost analysis as a tool in the developing process for new bridge edge beam solutions. *Structure and Infrastructure Engineering*, 12(9), 1185-1201.
- Wang, Q., Sun, W., Guo, L., Gu, C., & Zong, J. (2018). Prediction of chloride ingress in steel fibre reinforced concrete under bending load. *Ceramics–Silikáty*, 62(1), 59-66.
- Weyers, R. E. (1998). Service life model for concrete structures in chloride laden environments. *ACI Materials Journal*, 95(4), 445-453.

Table 1. Material parameters of concrete and reinforcing steel in the restraint crack calculation.

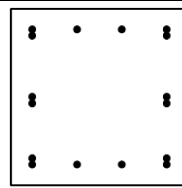
Parameter		Value
Concrete	grade	C40
	characteristic compressive strength f_{ck}	40 MPa
	mean compressive strength $f_{cm}=f_{ck}+8$	48 MPa
	mean tensile strength $f_{ctm}=0.3 (f_{ck})^{2/3}$	3.5 MPa
	modulus of elasticity $E_c=21500 \text{ MPa} (f_{cm}/10)^{1/3}$	36 GPa
	creep coefficient φ	0.8
	Effective modulus $E_{c,ef}=E_c/(1+\varphi)$	20 GPa
Steel	yield strength f_y	500 MPa
	Young's modulus E_s	200 GPa

Table 2. Alternative designs in the case study

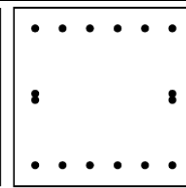
Alternative	steel bars	v_f (% vol.)	A_s (mm^2)	$A_{s,l}$ (mm^2)	f_t (MPa)	$f_{t,res}$ (MPa)	f_{Fu} (MPa)	M_u (kNm)	$w_{cr,max}$ (mm)	$w_{cr,mean}$ (mm)
PL1	10Ø16	0	2011	804	3.5	0	0	153	0.51	0.46
PL2	16Ø16	0	3217	1206	3.5	0	0	221	0.28	0.26
FRC1	10Ø16	0.5	2011	804	3.5	2.0	1.5	201	0.21	0.17
FRC2	8Ø16	0.5	1608	603	3.5	2.0	1.5	167	0.27	0.23
FRC3	8Ø16	1.0	1608	603	36	3.0	2.4	197	0.13	0.09
FRC4	10Ø12	1.0	1131	452	3.6	3.0	2.4	173	0.15	0.11



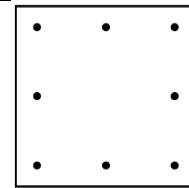
PL1, FRC1, FRC4



PL2-I



PL2-II



FRC2, FRC3

Longitudinal reinforcement layout

Table 3. Input parameters used in the chloride diffusion analysis.

Parameter	Value	Source
Surface chloride content C_s	1.0 wt.-%/cement	Tang and Utgenannt, 2007
Critical chloride content C_{crit}	0.6 wt.-%/cement	International Federation for Structural Concrete, 2006
Chloride diffusivity of uncracked PL and FRC D_0	$8 \times 10^{-12} \text{ m}^2/\text{s}$	Berrocal, 2017
Chloride diffusivity in the crack of PL designs D_{cr}	$45 \times 10^{-10} \text{ m}^2/\text{s}$	Inverse derivation from experimental data
Chloride diffusivity in the crack of FRC designs D_{cr}	$30 \times 10^{-10} \text{ m}^2/\text{s}$	Inverse derivation from experimental data

Table 4. EPD (A1-A3) of the materials from different producers.

Materials	CO ₂ eq.	Unit	Producer
Concrete	388	kg CO ₂ /m ³	Svensk Betong
Steel rebar	0.37	kg CO ₂ /kg	Celsa
	0.839	kg CO ₂ /kg	CARES
	1.23	kg CO ₂ /kg	ArcelorMittal
Steel fibre	0.703	kg CO ₂ /kg	Mapei

Table 5. Corrosion initiation time in cracked and uncracked region.

Alternative	D_0 (m ² /s)	$w_{cr,max}$ (mm)	D_{cr} (m ² /s)	$t_{i,u}$ (year)	$t_{i,cr}$ (year)	$t_{i,u} - t_{i,cr}$ (year)
PL1	8×10^{-12}	0.51	45×10^{-10}	14.3	2.7	11.6
PL2		0.28		14.3	5.4	8.9
FRC1		0.21	30×10^{-10}	14.3	8.8	5.5
FRC2		0.27		14.3	7.6	6.7
FRC3		0.13		14.3	10.4	3.9
FRC4		0.15		14.3	10.0	4.3

Table 6. Corrosion-induced crack width under uniform corrosion, and check of the residual moment capacity.

Alternative	v_{corr} ($\mu\text{m}/\text{y}$)	Corrosion-induced crack criterion $w_{corr}=0.5$ mm				Residual moment capacity criterion $\Delta M_u=15\%$		
		w_{corr} versus x_u	$x_{w0.5,u}$ (μm)	$t_{w0.5,u}$ (y)	ΔA_s	limit of ΔA_s	$x_{\Delta M_u=15\%}$ (μm)	$t_{\Delta M_u=15\%}$ (y)
PL1	10	$w_{corr}=0.00171x_u-0.107$	355	35.5	8.7%	15.3%	637	63.7
PL2		I: $w_{corr}=0.00190x_u-0.059$	294	29.4	7.2%	15.5%	646	64.6
		II: $w_{corr}=0.00173x_u-0.075$	332	33.2	8.1%			
FRC1		$w_{corr}=0.00062x_u-0.012$	827	82.7	19.6%	22.5%	957	95.7
FRC2		$w_{corr}=0.00079x_u-0.011$	647	64.7	15.5%	24.5%	1049	104.9
FRC3		$w_{corr}=0.00060x_u-0.026$	877	87.7	20.7%	30.0%	1307	130.7
FRC4		$w_{corr}=0.00029x_u-0.007$	1748	174.8	49.8%	34.0%	1126	112.6

Table 7. Comparison of the service life of difference designs.

Alternative	$t_{i,u}$ (y)	$t_p = \min(t_{w0.5,u}, t_{\Delta Mu=15\%})$ (y)	$T_{eb}=t_{i,u}+t_p$ (y)	Relative ratio to T_{eb} of PL1
PL1	14.3	35.5	50	100%
PL2	14.3	29.4	44	88%
FRC1	14.3	82.7	97	194%
FRC2	14.3	64.7	79	158%
FRC3	14.3	87.7	102	204%
FRC4	14.3	112.6	127	254%

Figure 1. A bridge edge beam in Sweden with cracks that have been injected and sealed.

Figure 2. A simple sketch of the cross-section of the edge beam.

Figure 3. Steps in the case study.

Figure 4. Restraint cracking model of hybrid RC element (after Löfgren, 2007); $w(\sigma_s)$ is the restraint crack width which is related to the steel stress σ_s ; $N(\sigma_s)$ and $N(f_{t,res})$ is the force carried by the reinforcement bars and FRC respectively.

Figure 5. Influence of reinforcement ratio ρ and residual tensile strength ($\alpha_f f_{ctm}$) of FRC on the (a) maximum restraint crack width $w_{cs, max}$ and (b) mean restraint crack width $w_{cs, mean}$ (for the 16 mm diameter rebar, the markers in each curve correspond to the number of rebar, namely 8, 10, 12, 14, 16 and 18 from the leftmost point to the rightmost one).

Figure 6. Stress block in hybrid RC cross section.

Figure 7. Corrosion initiation time versus pre-existing crack width from the model and experiments of Berrocal et al. (2015).

Figure 8. Physical interpretation of the variables in the corrosion model under uniform corrosion (after Lundgren, 2005).

Figure 9. Finite element mesh and boundary conditions for the corrosion-induced cracking analysis of a thin slice.

Figure 10. Corrosion-induced crack patterns at different corrosion penetration depths. (a) PL1 at $x_u = 100, 150, 200, 250 \mu\text{m}$; (b) PL2-I at $x_u = 100, 150, 200, 250 \mu\text{m}$; (c) PL2-II at $x_u = 100, 150, 200, 250 \mu\text{m}$; (d) FRC1 at $x_u = 150, 250, 350, 450 \mu\text{m}$; (e) FRC2 at $x_u = 150, 250, 350, 450 \mu\text{m}$; (f) FRC3 at $x_u = 150, 250, 350, 450 \mu\text{m}$; (g) FRC4 at $x_u = 150, 250, 350, 450 \mu\text{m}$.

Figure 11. Corrosion-induced crack width versus corrosion penetration depth from FE analysis and simplified linear fitting.

Figure 12. Influence of unit cost of fibre on (a) investment costs (INV) and (b) life-cycle costs (LCC), under the parameters $T = 120 \text{ y}$, $L_{bridge} = 15 \text{ m}$, $ADT = 10000 \text{ veh/d}$, $p = 3.5\%$.

Figure 13. Influence of the design life of a bridge ($T = 120$ or 80 y) on the LCC (including INV, REP and USE, representing investment, replacement and user costs respectively) for the six designs under the parameters $m_f = 20$ SEK/kg, $L_{bridge} = 15$ m, $ADT = 10000$ veh/d, $p = 3.5\%$.

Figure 14. Influence of bridge length ($L_{bridge} = 15$ or 150 m) on LCC (including INV, REP and USE, representing investment, replacement and user costs respectively) for the six designs under the parameters $m_f = 20$ SEK/kg, $T = 120$ y, $ADT = 10000$ veh/d, $p = 3.5\%$.

Figure 15. Influence of the average daily traffic ($ADT = 5000, 10000, 15000,$ and 20000 veh/d) on LCC (including INV, REP and USE, representing investment, replacement and user costs respectively) for the six designs under the parameters $m_f = 20$ SEK/kg, $T = 120$ y, $L_{bridge} = 15$ m, $p = 3.5\%$.

Figure 16. Influence of the discount rate ($p = 2\%, 3.5\%, 5\%$ and 7%) on LCC (including INV, REP and USE, representing investment, replacement and user costs respectively) for the six designs under the parameters $m_f = 20$ SEK/kg, $T = 120$ y, $L_{bridge} = 15$ m, $ADT = 10000$ veh/d.

Figure 17. Global warming potential (GWP) from the concrete, steel rebar and steel fibre in each design, with steel producers Celsa, CARES and ArcelorMittal respectively.

Figure 18. Comparison of the annual total global warming potential (GWP) in each design with steel producers Celsa, CARES and ArcelorMittal respectively.



Figure 1. A bridge edge beam in Sweden with cracks that have been injected and sealed.

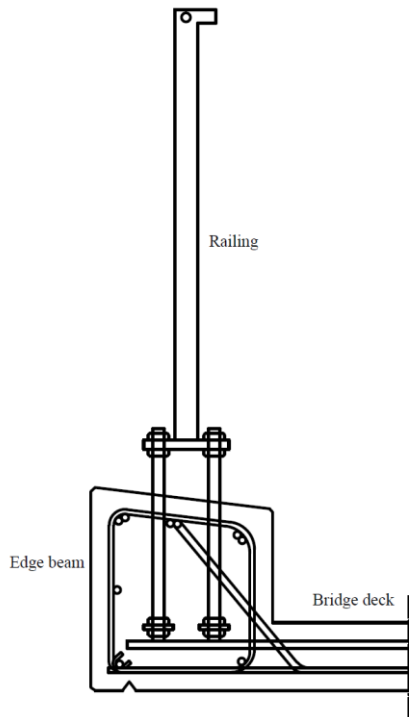


Figure 2. A simple sketch of the cross-section of the edge beam.

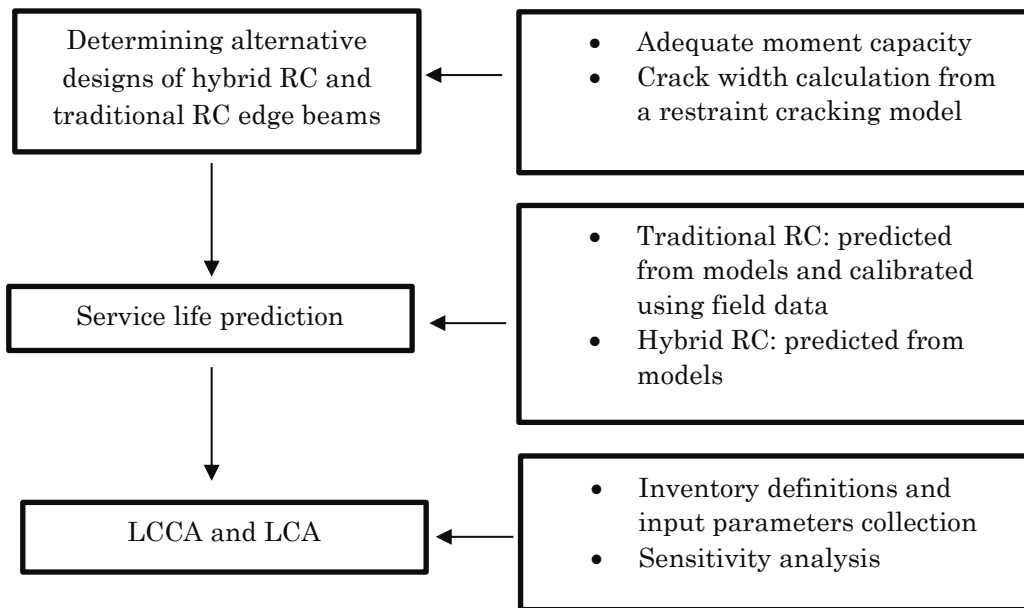


Figure 3. Steps in the case study.

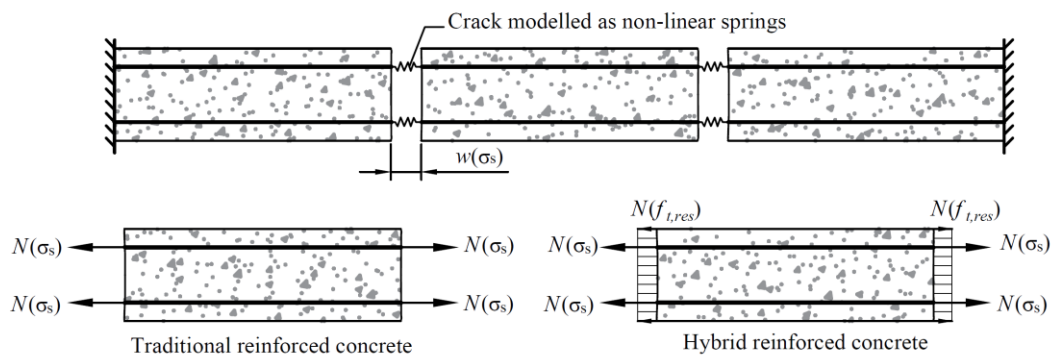


Figure 4. Restraint cracking model of hybrid RC element (after Löfgren, 2007); $w(\sigma_s)$ is the restraint crack width which is related to the steel stress σ_s ; $N(\sigma_s)$ and $N(f_{t,res})$ is the force carried by the reinforcement bars and FRC respectively.

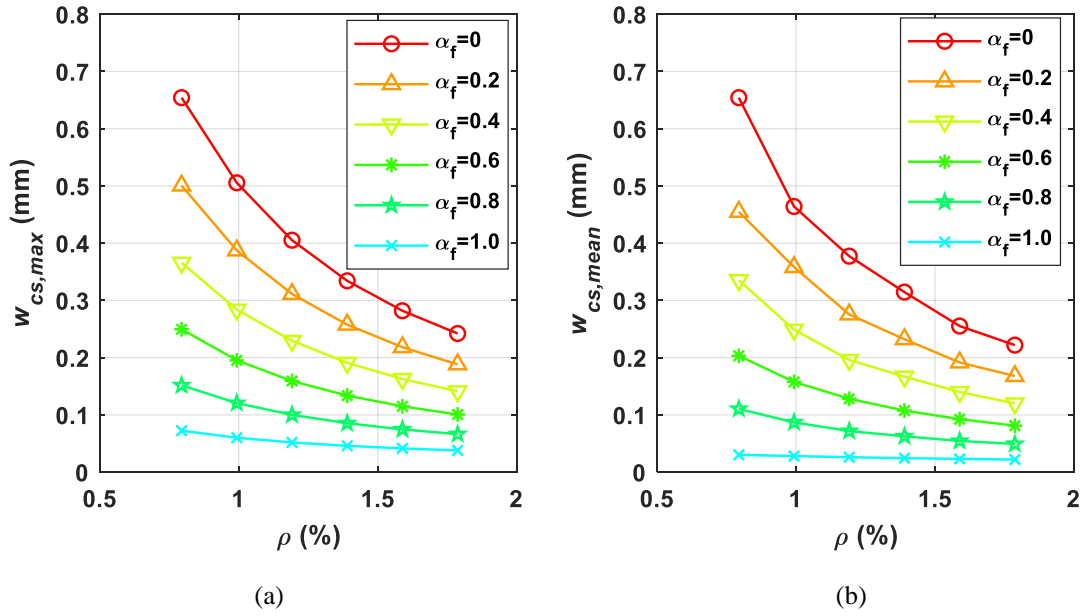


Figure 5. Influence of reinforcement ratio ρ and residual tensile strength ($\alpha_f f_{ctm}$) of FRC on the (a) maximum restraint crack width $w_{cs,max}$ and (b) mean restraint crack width $w_{cs,mean}$ (for the 16 mm diameter rebar, the markers in each curve correspond to the number of rebar, namely 8, 10, 12, 14, 16 and 18 from the leftmost point to the rightmost one).

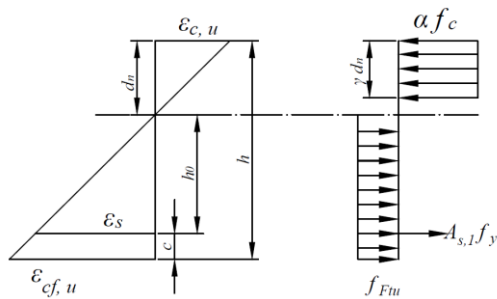


Figure 6 Stress block in hybrid RC cross section

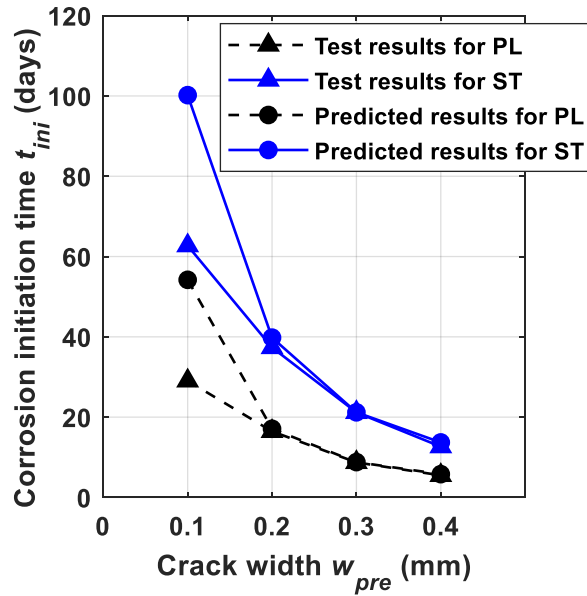


Figure 7. Corrosion initiation time versus pre-existing crack width from the model and experiments of Berrocal et al. (2015).

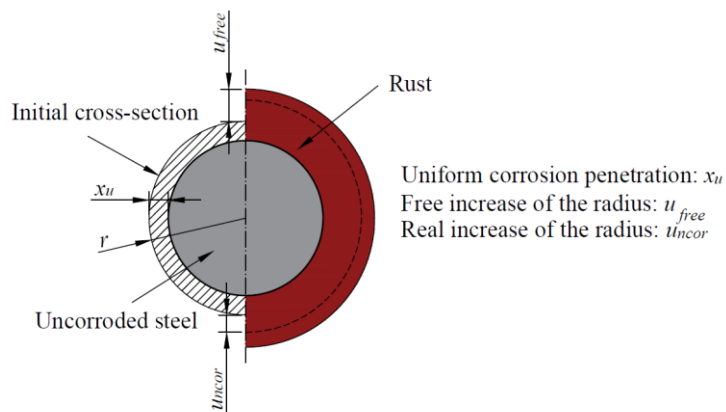


Figure 8. Physical interpretation of the variables in the corrosion model under uniform corrosion (after Lundgren, 2005).

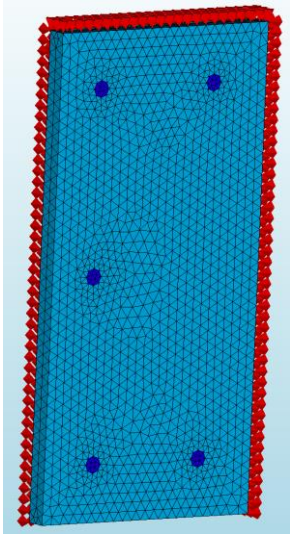
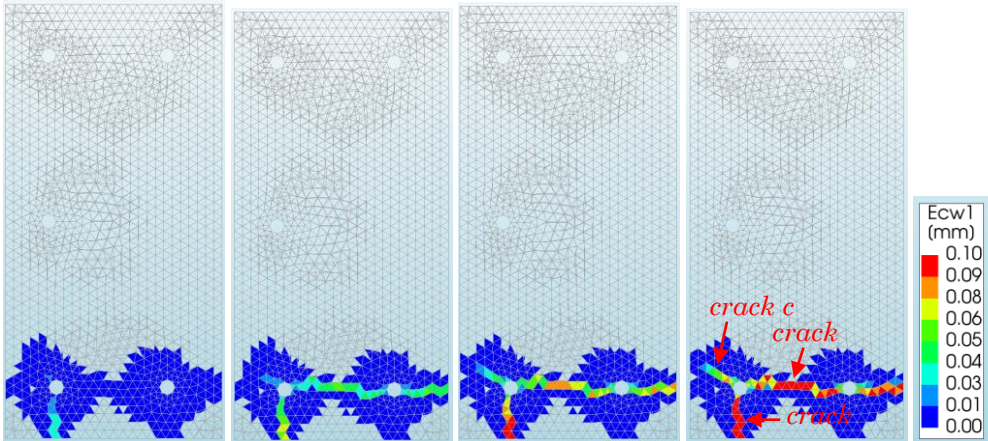
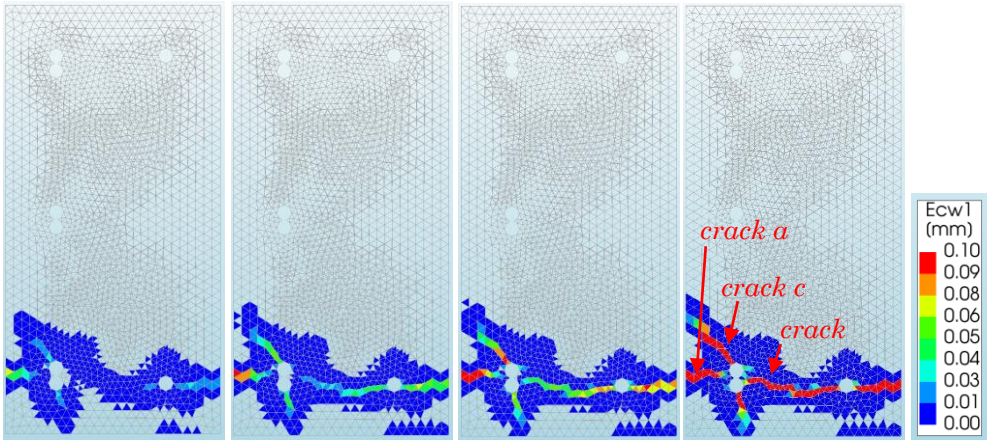


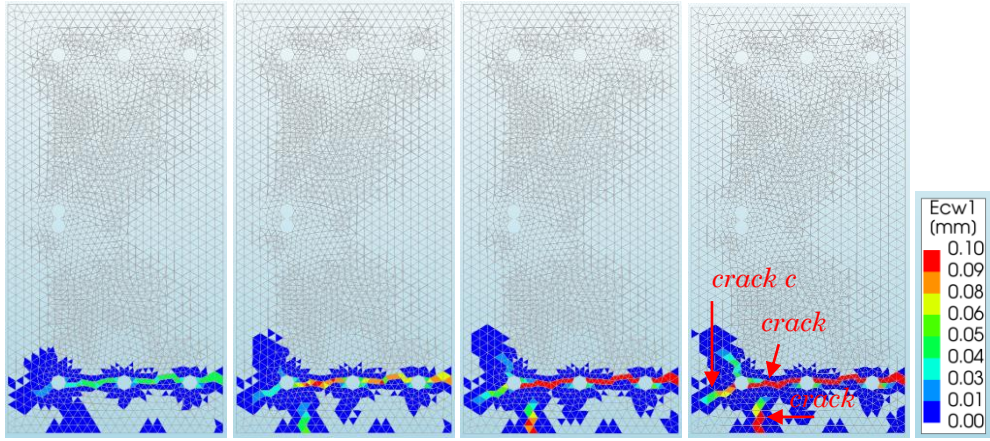
Figure 9. Finite element mesh and boundary conditions for the corrosion-induced cracking analysis of a thin slice.



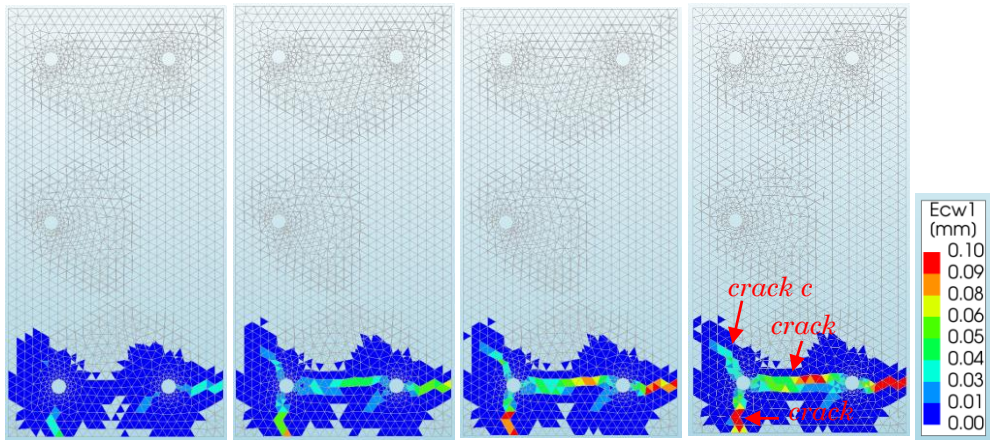
(a)



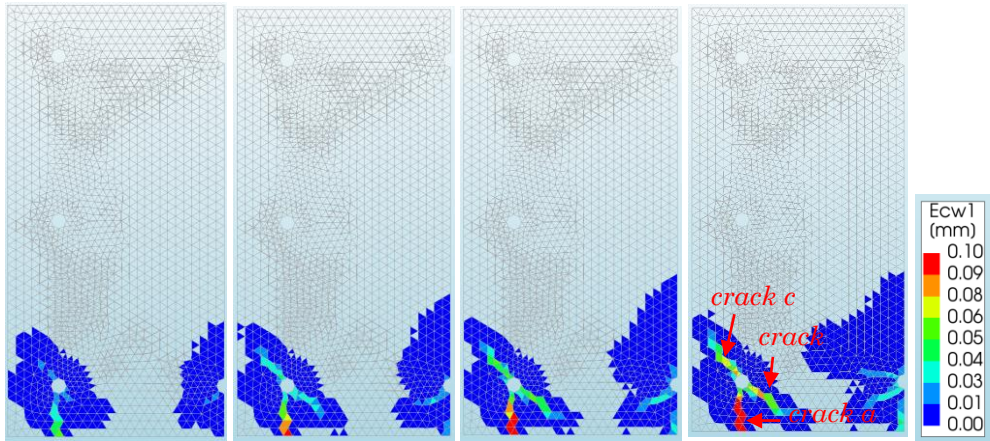
(b)



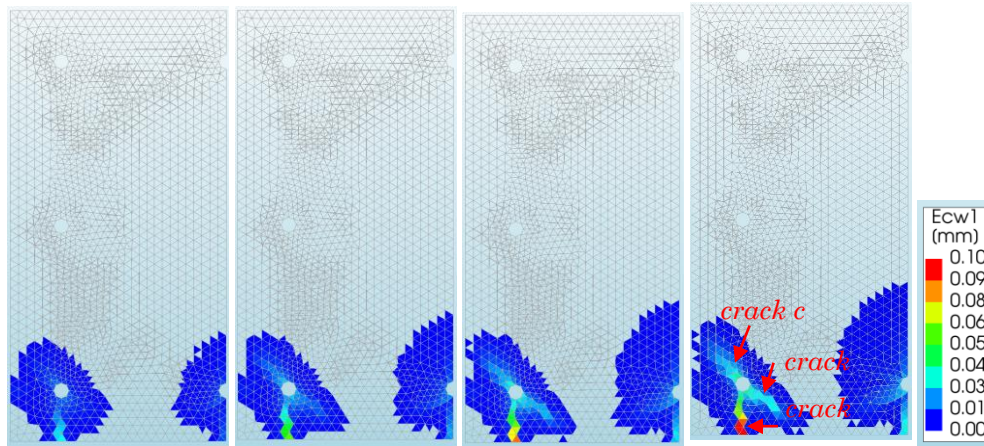
(c)



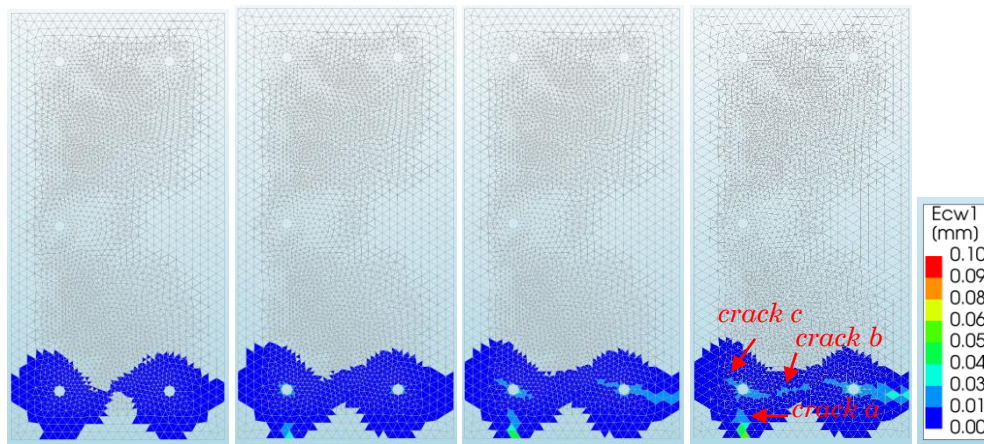
(d)



(e)



(f)



(g)

Figure 10. Corrosion-induced crack patterns at different corrosion penetration depths. (a) PL1 at $x_u = 100, 150, 200, 250 \mu\text{m}$; (b) PL2-I at $x_u = 100, 150, 200, 250 \mu\text{m}$; (c) PL2-II at $x_u = 100, 150, 200, 250 \mu\text{m}$; (d) FRC1 at $x_u = 150, 250, 350, 450 \mu\text{m}$; (e) FRC2 at $x_u = 150, 250, 350, 450 \mu\text{m}$; (f) FRC3 at $x_u = 150, 250, 350, 450 \mu\text{m}$; (g) FRC4 at $x_u = 150, 250, 350, 450 \mu\text{m}$.

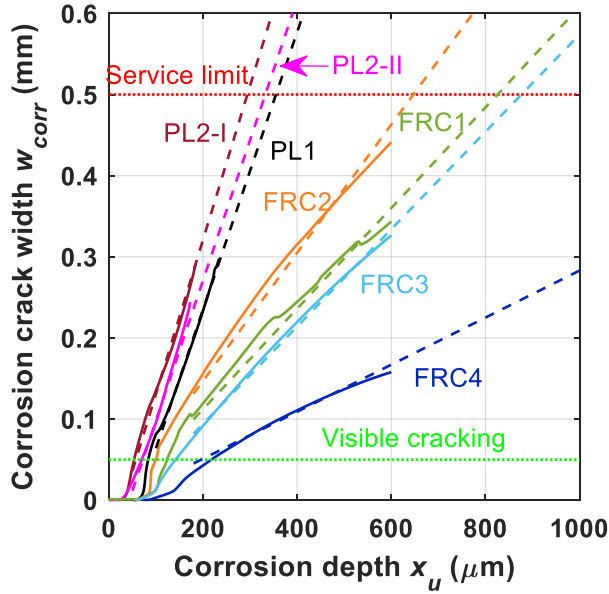


Figure 11. Corrosion-induced crack width versus corrosion penetration depth from FE analysis and simplified linear fitting.

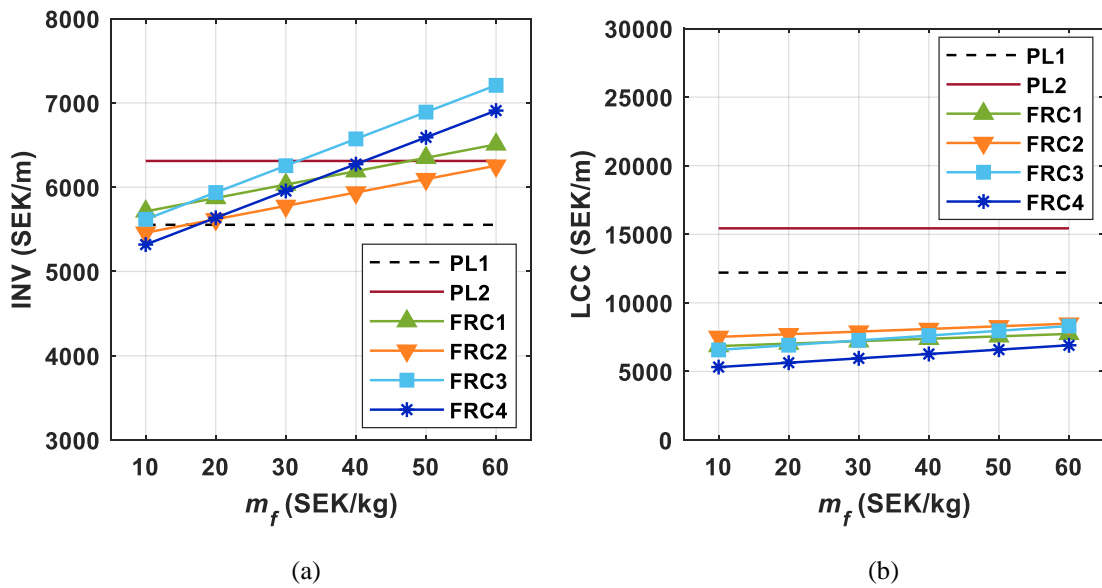


Figure 12. Influence of unit cost of fibre on (a) investment costs (INV) and (b) life-cycle costs (LCC), under the parameters $T = 120$ y, $L_{bridge} = 15$ m, $ADT = 10000$ veh/d, $p = 3.5\%$.

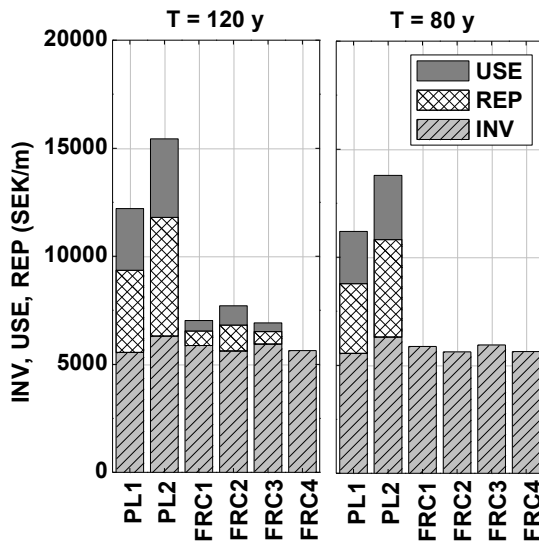


Figure 13. Influence of the design life of a bridge ($T = 120$ or 80 y) on the LCC (including INV, REP and USE, representing investment, replacement and user costs respectively) for the six designs under the parameters $m_f = 20$ SEK/kg, $L_{bridge} = 15$ m, $ADT = 10000$ veh/d, $p = 3.5\%$.

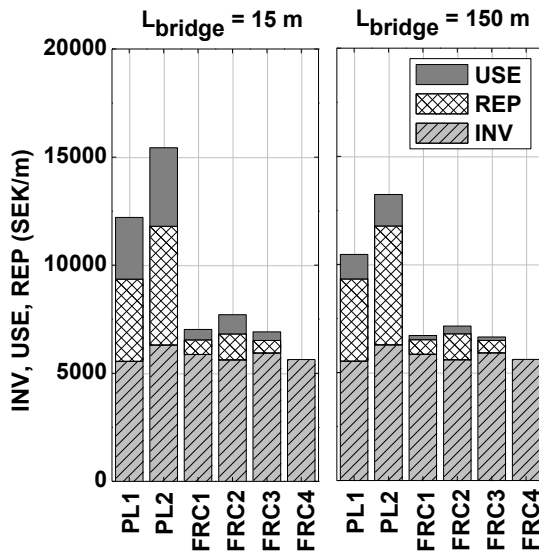


Figure 14. Influence of bridge length ($L_{bridge} = 15$ or 150 m) on LCC (including INV, REP and USE, representing investment, replacement and user costs respectively) for the six designs under the parameters $m_f = 20$ SEK/kg, $T = 120$ y, $ADT = 10000$ veh/d, $p = 3.5\%$.

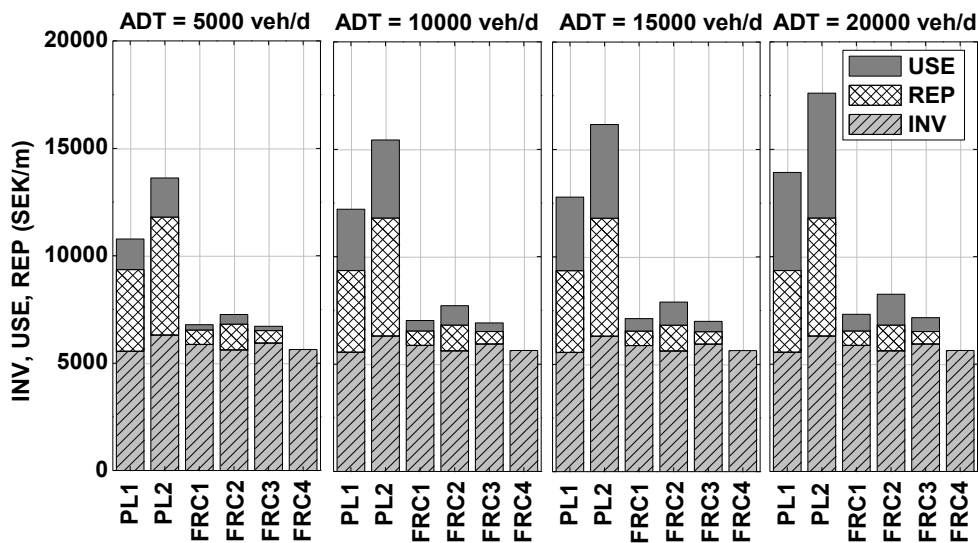


Figure 15. Influence of the average daily traffic ($ADT = 5000, 10000, 15000,$ and 20000 veh/d) on LCC (including INV, REP and USE, representing investment, replacement and user costs respectively) for the six designs under the parameters $m_f = 20$ SEK/kg, $T = 120$ y, $L_{bridge} = 15$ m, $p = 3.5\%$.

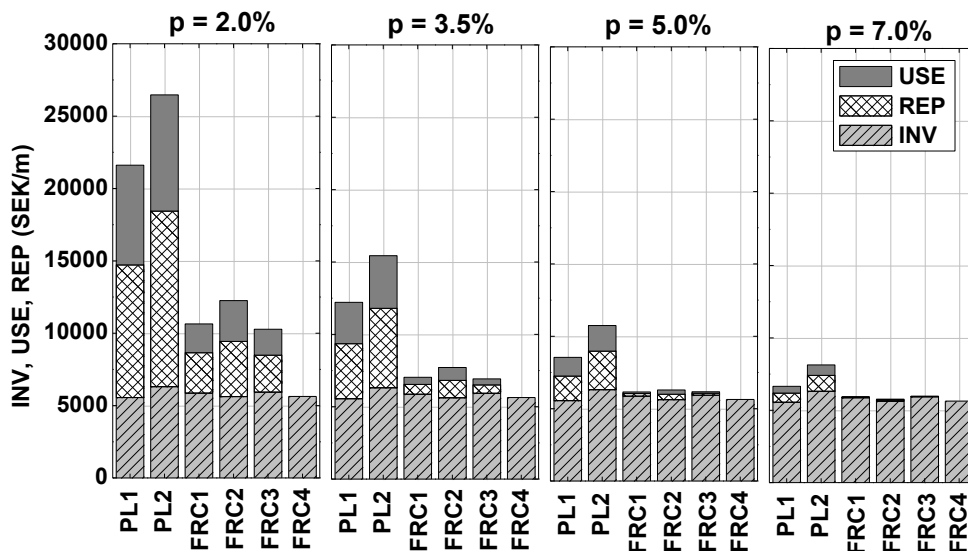


Figure 16. Influence of the discount rate ($p = 2\%, 3.5\%, 5\%$ and 7%) on LCC (including INV, REP and USE, representing investment, replacement and user costs respectively) for the six designs under the parameters $m_f = 20$ SEK/kg, $T = 120$ y, $L_{bridge} = 15$ m, $ADT = 10000$ veh/d.

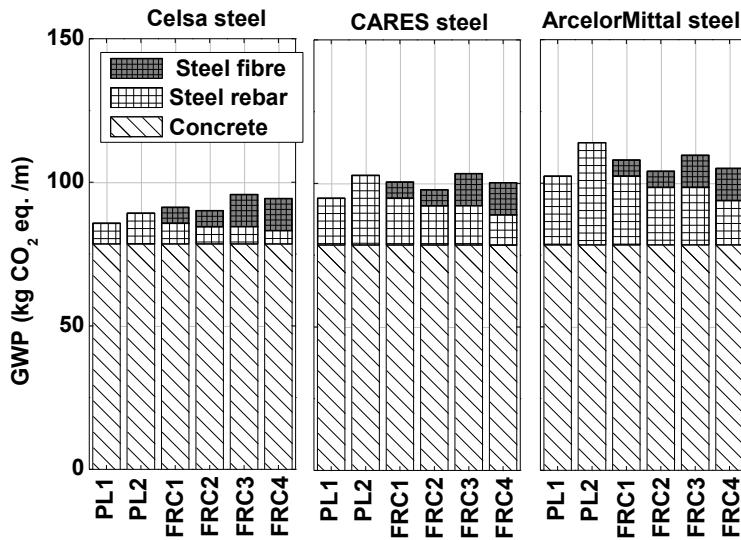


Figure 17. Global warming potential (GWP) from the concrete, steel rebar and steel fibre in each design, with steel producers Celsa, CARES and ArcelorMittal respectively.

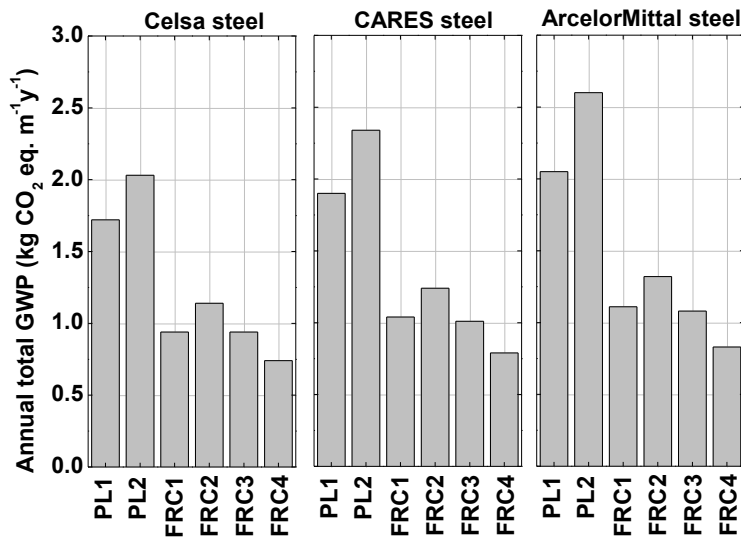


Figure 18. Comparison of the annual total global warming potential (GWP) in each design with steel producers Celsa, CARES and ArcelorMittal respectively.

